PLANAR LASER INDUCED IODINE FLUORESCENCE FOR THE INVESTIGATION OF THE AERODYNAMICS OF REACTION CONTROL SYSTEM JETS ON MARS-ENTRY AEROSHELLS

_____

A Dissertation

Presented to

the faculty of the School of Engineering and Applied Science

University of Virginia

_____

in partial fulfillment

of the requirements for the degree

Doctor of Philosophy

by

Erin Michele Reed

December 2013

Approval Sheet

This dissertation

is submitted in partial fulfillment of the requirements

for the degree of

Doctor of Philosophy

_____
Author

This dissertation has been read and approved by the examining committee:

_____James C. McDaniel_____
Advisor
_____Robert Ribando_____

_____Harsha Chelliah_____

_____Chris Goyne_____

_____Kevin Lehmann_____

Accepted for the School of Engineering and Applied Science:

Dean, School of Engineering and Applied Science
December 2013

ABSTRACT

In order to improve landing accuracies on Mars in preparation for future manned mission, effort has been made in improving control of the vehicle through the use of reaction control system jets under rarefied conditions where normal control surfaces (ailerons, rudders, etc.) are ineffective. Despite their use on Apollo and Viking landers, as well as the space shuttle, firing the reaction control system (RCS) jets can have unanticipated effects on the aeroshell such as augmented heating and induced adverse forces and moments. In order to better understand the aerodynamics of the interactions of reaction control system jets with the aerodynamics of the spacecraft aeroshell in high-speed flow, a qualitative and quantitative study using an experimental method termed Planar Laser Induced Iodine Fluorescence was conducted.

Planar Laser Induced Iodine Fluorescence (PLIIF) is a non-intrusive optical diagnostic technique that utilizes the principles of fluorescence spectroscopy in order to obtain high-resolution planar qualitative flowfield images that clearly exhibit shocks and interactions, as well as quantitative planar velocity and temperature flowfield measurements. The PLIIF method is the only diagnostic techniques that can produce planar velocity and temperature measurements in the mixed continuum and rarefied flowfield conditions that exist for the experiment reported herein.

Using a low-pressure chamber, a model was subjected to Mach 12 freestream flow in order to simulate entry conditions at high speeds. For this research, two RCS jet configurations – a jet issuing transverse to the freestream and a jet issuing parallel to the freestream - were investigated at several thrust coefficients. It was found that the jet

issuing transverse to the freestream had strong interaction with the bow shock that formed off the model, resulting in the bow shock being pushed farther away from the model as well as an inhibited RCS jet expansion. This RCS jet/bow shock interaction can be supposed to have a significant effect on the surface pressures on the model to induce forces and moments. The jet issuing parallel to the freestream indicated little interaction with the model bow shock. For both jet configurations, recirculation regions near the RCS jets with low velocities and high temperatures suggests that flow around the aeroshell in a Mars entry flight would have total temperature recovery in these regions, inducing localized heating.

Qualitative results for the parallel jet configuration at a jet thrust coefficient of 0.5 and quantitative results for both configurations at a jet thrust coefficient of 1.0 were compared to CFD/LeMANS calculations completed at the University of Michigan. The LeMANS computations were computed with consideration for the experimental setup in order to produce high fidelity for conditions with the experiment for comparisons. The results showed agreement in the model bow shock structure on the forebody of the model but exhibited a difference in shock structure and RCS jet structure elsewhere. The velocity and temperature comparisons along the jet centerlines of both configurations showed good agreement. Once compared to the experimental results, computational results can be considered to give predictions of RCS performance. A study of control gain by the University of Michigan indicated that the parallel jet results in near ideal control of the aeroshell while the transverse jet results in diminished control effectiveness. Such measurements have not previously been possible and are due to the unique capability for the PLIIF technique in mixed continuum/rarefied flows.

ACKNOWLEDGEMENTS

Without the support of faculty, friends and family, completing this research would never have been possible. I am deeply grateful for everyone's guidance, patience and assistance in helping me get to this point.

I would like to thank, first of all, my advisor, Jim McDaniel, for his continual patience and optimism towards me and the equipment in my lab, for his scientific insight and advice and for giving me the opportunity to grow as a researcher. I am grateful for his help and support throughout the years. I would like to thank my undergraduate mentors Dale Tree and Jerry Bowman for their encouragement and their advice. I would like to thank Professor Robert Ribando, Professor Harsha Chelliah, Professor Kevin Lehmann, Professor Chris Goyne and Professor Eric Loth for their service on my committees. I have learned so much from their classrooms and am grateful for their guidance throughout this dissertation process. A special thanks to Hicham Alkandry and Iain Boyd at the University of Michigan for the collaboration on this research. I have enjoyed and appreciated every encounter during this joint effort. I would like to thank Eric Cecil for helping me to learn the lab procedures and technique. I would also like to thank my colleague Joshua Codoni, who has proven his mettle time and time again and has taught me so much more than I ever pretended to teach him. Thanks to Luther Tychonievich for his mentorship and data analysis help. Thank you, Roger Reynolds and Ed Spencely, without whose wonderful contributions to the work, I would not have gotten far. Also, a thank you to Bryan Palaschewski, Chris Glass, and many others at NASA, who have shown interest in my work and asked me good questions to guide me.

I am grateful to everyone at the Aerospace Research Lab and wish them good luck on their bright futures. Also thanks to Isao Tamada and to the Asai/Nagai lab at Tohoku University who taught me so much about collaborative research that could span languages and cultures.

I am grateful to all my friends that I have made during my time here at the University of Virginia. Words cannot adequately express how much your friendship has meant to me, during both good times and bad. Thank you to my dear family: you show me best the meaning of true and unconditional love. And thank you to Makoto Hasebe, for inspiring me to believe that I can make a difference.

TABLE OF CONTENTS

LIST OF FIGURES

Figure

LIST OF TABLES

LIST OF APPENDICES

NOMENCLATURE

Acronyms

CCD	Charge-Coupled Device
CFD	Computational Fluid Dynamics
DSMC	Direct Simulation Monte Carlo
EDL	Entry, Descent and Landing
MSL	Mars Science Lander
NASA	National Aeronautics and Space Administration
PLIIF	Planar Laser Induced Iodine Fluorescence
RCS	Reaction Control Systems

Latin Symbols

A	Ashkenas and Sherman constant, 3.65
A_j	Area of the jet exit
A_{21}	Fluorescence coefficient
b_{12}	Einstein absorption coefficient
b_{21}	Stimulated emission coefficient
c	Speed of light, 3×10^8 m/s
C_b	Broadening coefficient
C_I	Impact shift coefficient
C_p	Heat capacity
C_q	Quenching coefficient
C_T	Jet thrust coefficient
f_1	Boltzmann population fraction in ground state
f_s	Seeding fraction
I_2	Diatomic iodine
J''	Rotational quantum number in the ground state
J'	Rotational quantum number in the excited state
k	Boltzmann constant
$\dot{m}$	Mass flow rate
M	Mach number
n_1	Number of molecules in the ground state
n_2	Number of molecules in the excited state
p	Pressure, kPa (atm)
q	Dynamic pressure
Q_{12}	Quenching coefficient
Q_{21}	Quenching coefficient
R	Recombination coefficient
R	Gas constant for nitrogen

S_{impact}	Impact shift uncertainty
S_p	Pressure uncertainty
S_{shift}	Frequency shift uncertainty
S_T	Temperature uncertainty
S_v	Velocity uncertainty
T	Temperature, K
T	Thrust
u	Velocity, m/s
v"	Vibrational quantum number in the ground state
v'	Vibrational quantum number in the excited state
x/D	Distance normalized by jet diameter
x_0/D	Source flow location for Ashkenas and Sherman relationship, 0.4

Greek Symbols

γ	Ratio of Specific Heats, 1.4 for nitrogen
λ_0	Wavelength of the argon laser, 514.5 nm
ν_0	Frequency observed by a stationary molecule
$\Delta\nu_D$	Doppler linewidth
$\Delta\nu_{Doppler}$	Doppler shift
$\Delta\nu_I$	Impact shift
Θ_{rot}	characteristic rotational temperature
Θ_{vib}	characteristic vibrational temperature

Subscripts

$(-)_0$	Stagnation/Total conditions
$(-)_j$	RCS exit conditions
$(-)_t$	Total conditions
$(-)_\infty$	Freestream conditions

CHAPTER ONE

INTRODUCTION

1.1 Reaction Control System Jet

Although seven vehicles to date have successfully landed on Mars, the task of a vehicle safely entering the Martian atmosphere, maneuvering safely in descent, and landing continues to be a considerable challenge. For one, Mars has a much thinner atmosphere than Earth (about 1%). This means less drag is produced on the aeroshell's blunt body that is normally relied upon to help slow a reentry vehicle to low velocities for a safe landing. The other complication is that the atmosphere is still dense enough to cause significant heating concerns for the aeroshell and thermal protection system [1, 2]. Mars is also known to have a stormy atmosphere with strong winds that can complicate reentry vehicle maneuvering during entry and descent by possibly drastically altering the flight path of the vehicle. Furthermore, rocks and craters strewn across Mars' surface limit regions of the planet suitable in ensuring safe landings.

As a result of these several considerations, before the Mars Science Laboratory (MSL) mission, landing footprints chosen were on the order of 100's of kilometers in relatively

rock-free regions of the Martian landscape. This footprint size must be decreased to allow access to scientifically-interesting regions. Furthermore, in looking towards manned missions, heavier vehicles would need to land in areas on the order of 10's of meters (or four orders of magnitude smaller than previously) [1, 3-4]. MSL, which was larger and heavier than previous landers, served as an important step in moving towards a larger space vehicle with an improved accuracy of one order of magnitude (10 km radius landing footprint) [3, 5-7]. However, taking such an important step also brought new challenges to the already complicated scenario: the large ballistic coefficient (measure of vehicle's resistance to surrounding air during flight) from the larger vehicle size and mass results in higher velocities at lower altitudes. This means higher dynamic pressure (on the surface of the vehicle) and higher Reynolds numbers, so that that turbulent transition is highly likely. In other words, for the MSL and moreso, for future manned mission, more severe aerothermodynamic conditions exist than on any previous Mars entry vehicle [8].

In light of these challenges in landing on Mars, utilizing control for maneuvering throughout the entry, descent and landing sequence from the rarefied regimes to continuum is necessary [9]. One such technology used for maneuvering and navigation is the use of Reaction Control System (RCS) jets. RCS jets have been in use since the Apollo era to help orient entry vehicles at altitudes where control surfaces — ailerons, rudders, etc. — are ineffective. They also help dampen oscillations introduced during entry by either the vehicle's own inertia or due to the atmosphere, by the use of yaw and roll commands [10]. Despite their use for so many missions over the years, firing the RCS jets has resulted in augmented heating on the unprotected backshell of the entry vehicle, as well as plumes that impact the aerodynamics of the entry capsule, including induced

adverse moments that cause thrust reversal [6, 10-13]. In addition, it is difficult to predict the control effectiveness of the RCS jets [14]. These RCS jets fire into the wake region behind the aeroshell of the vehicle. It has been suggested that the jet plume interacts with the vehicle wake and alters it, thus affecting jet impingement on the vehicle and interaction with the atmosphere and other flow structures around the entry capsule [8-9, 13]. In order to improve the performance and reliability of RCS jets, it is necessary to study these complicated RCS jet/flowfield interactions.

1.2 Computations vs. Experiments

Necessarily, there are certain trade-offs in the application of either computational methods or experimental techniques. Experiments are limited in their ability to effectively reproduce and investigate simultaneously all of the atmospheric entry conditions on Mars. On the other hand, the complexity of the flowfields can mean that computational models are unable to correctly predict flight conditions when compared to flight data, thus necessitating experiments to help improve the models for future flights. This is especially so because capsule designs change from mission to mission [15]. As Spaid and Cassel reported,

> "the jet interaction flowfield is so complex that predictions of induced forces, pressure distributions, concentration distributions, etc., must heavily rely on experimental data. Accurate predictions concerning situations which lie far outside the range of available data will require additional experimentation" [16].

More recently, Mitcheltree et. al. [7] stressed the need for validation in order to address the concerns of modeling RCS interactions with the capsule wake. Experiments can effectively serve as validation for computational models in order to improve the knowledge of flowfield phenomena. Both experiments and computations that investigate these phenomena are essential components of creating a reliable database for use in entry vehicle performance and characterization [6].

1.3 Joint Experimental/Computational Effort

The need for using both experiments and computations is well established. However, the comparison of the different approaches can be complicated by the many different parameters in a given experiments and matching them in the computations. This body of research was funded by NASA Headquarters with the intention of completing a joint experimental (University of Virginia) and computational (University of Michigan) study of the RCS jet interactions. Through collaboration in maintaining similar conditions, it was hoped that a true comparison of the two approaches could be made. The research reported in this dissertation focuses on the experimental technique used in the joint work; however, the computational method used will be described briefly.

1.4 Computational Method

Numerical simulations are performed using the computational fluid dynamics (CFD) code LeMANS, developed at the University of Michigan for simulating hypersonic reacting

flows [17-18]. This general purpose, three-dimensional, parallel code solves the laminar Navier-Stokes equations on unstructured computational grids including thermo-chemical nonequilibrium effects with second-order accuracy. In LeMANS, the flow is modeled assuming that the continuum approximation is valid and that the fluid can be weakly ionized. The validity of the continuum approximation is best measured by Gradient-Length Local Knudsen number. Breakdown would occur for Knudsen values >0.05. Calculating this number for the experiment conditions, the continuum assumption has been determined to be valid for the RCS jet interaction [49, 107].

The finite-volume method applied to unstructured grids is used to solve the set of differential equations. LeMANS can simulate two-dimensional/axisymmetric flows using any mixture of quadrilateral and triangular mesh cells, and three-dimensional flows using any mixture of hexahedra, tetrahedra, prisms, and pyramids. It employs a modified Steger-Warming Flux Vector Splitting scheme to discretize the inviscid fluxes across cell faces, which is less dissipative and produces better results in boundary layers compared to the original scheme. Viscous terms are computed using cell center and node values. Time marching is performed using either a point implicit or a line implicit method. LeMANS is parallelized using METIS to partition the computational mesh between processors and MPI to communicate information between processors [19].

1.5 Experimental Technique

In order to experimentally study the aerodynamics of different flows and different applications, it is necessary to use an appropriate measurement technique. Optical

diagnostic methods are attractive methods for studying aerodynamics because they do not disturb the flow by use of physical probes. Hiller outlines six important characteristics in an optical diagnostic method: non-intrusive probing, sufficient temporal resolution, high signal-to-noise ratio, good spatial resolution, planar/3-D capabilities, and operable flow conditions [20]. Laser induced fluorescence provides strong signals with the capability for spatial and temporal resolution and can be applied in a large range of flows from continuum to rarefied, as well as mixed continuum/rarefied regimes (such as the one present in the current RCS investigation). This makes it advantageous over other methods, such as Coherent Raman techniques, which are limited to single-point measurements, as well as Schlieren and Rayleigh Scattering methods which are not useful in rarefied flow conditions [21]. The Electron Beam Fluorescence technique, which is a quantitative technique that analyzes resulting fluorescence from an excitation electron beam source, is a technique primarily used in rarefied gas flow investigations [22-25]. However, this technique is limited only to low density (rarefied) flows due to problems with beam scattering, quenching and the beam current measurement at higher densities [22]. Thus, it is necessary to use a technique like laser induced fluorescence which is applicable to both rarefied and continuum flows.

The largest challenge of laser-induced fluorescence is finding a seeding molecule that has resonant transitions with an available laser. For this work, iodine has been chosen as the seed molecule based on its strong visible absorption spectrum when excited by the 514.5 nm line of the argon ion laser. Iodine has a vapor pressure of 0.3 torr at room temperature which provides adequate seeding (about 1 part iodine in 10,000 parts nitrogen). Iodine also has a large absorption cross-section and a relatively long fluorescent

lifetime (on the order of a microsecond), thus making it a good choice as a seeding molecule [26]. Further, iodine has also been extensively studied and well documented, so properties of iodine are well-known [27-31]. Iodine does have the drawback of being highly corrosive to materials, especially in the presence of water, and can be detrimental to human health with extended contact or in high doses; however, by selecting proper materials and keeping the iodine in a closed system that is purged before venting into the atmosphere, it is possible to minimize these adverse effects.

The technique of Planar Laser Induced Iodine Fluorescence has been developed at the University of Virginia and used as a qualitative and quantitative technique to obtain both visualization images as well as quantitative measurement of pressure, temperature, density, mole fraction and velocity in a cross-sectional plane of the flow. It has been applied in continuum and rarefied regimes as well as mixed continuum/rarefied flows [21, 32-36].

1.6 Thesis Statement:

The purpose of this research is to use the technique of Planar Laser Induced Iodine Fluorescence to obtain experimental data for the study of fundamental aerodynamics of RCS jet interactions with an entry vehicle. The data will also be used for comparison and validation of CFD predictions.

As the wind tunnel facility at the Aerospace Research Laboratory has never been applied to blunt body flows with RCS jets, the first objective of this work is to determine the experimental parameters necessary for this research. These experimental parameters

include freestream Mach number, RCS thrust coefficients, blunt body model design and size, and RCS jet design.

A second objective of this work is to obtain qualitative images for a preliminary understanding of the flowfield phenomena, such as the complicated interactions of the RCS plume with the bow shock generated by the model. These qualitative images will be compared to CFD predictions of flowfield features. The qualitative images will also be used to examine a variety of flow conditions and setups for further quantitative studies.

A third objective of this work is to obtain quantitative planar flowfield data of temperature and velocity. The quantitative data will be applied to a few specifically chosen cases determined by the qualitative data. The results will then be compared to quantitative CFD results. It is anticipated that these quantitative results will allow for an improved fundamental understanding of the aerodynamics of RCS jets.

1.7 Outline

In Chapter Two, relevant research is reviewed and summarized. Relevant research refers to both experimental (and limited computational) studies of reaction control system jets and previous research using the Laser Induced Fluorescence technique.

Chapter Three explains the theory and technique of Planar Laser Induced Iodine Fluorescence. The chapter first discusses the mechanisms of excitation and relaxation of iodine molecules and gives relevant equations used to derive the fluorescence signal equation. Next, the transitions accessed by excitation from an argon ion laser are given and

the thermodynamic dependencies of the fluorescence spectra are discussed. Finally, the technique as it applies to qualitative images and to quantitative velocity, and thermodynamic properties is explained.

Chapter Four discusses the experimental facilities used for the research. The low-pressure chamber used to obtain hypersonic flows, the laser and optics system and the camera characteristics are all discussed in turn.

Chapter Five outlines some of the initial considerations used to design the model and experimental parameters. A plasma visualization study was used to help reduce shock interactions that would not be modeled by the computations and which would affect the experimental results. The model design of two RCS configurations – a parallel and a transverse configuration - is discussed, as well as the determination of jet thrust coefficient, the freestream Mach number, and the RCS jet exit Mach number.

In Chapter Six, the data collection method is discussed for both the qualitative and quantitative measurements. Because of the complicated experimental setup, data collection required use of an automated computer program that simultaneously controlled the CCD camera, laser scanning, as well as monitored pressures and temperatures. The steps taken to complete the experiments are briefly discussed. Finally, the data analysis method is discussed in detail.

Chapter Seven reports the qualitative results for the RCS parallel jet and transverse jet configurations. Because two cameras were used to obtain the qualitative images, the lower resolution camera images are shown and discussed only briefly. Most of the chapter instead focuses on the higher resolution camera images.

Quantitative data for the RCS transverse jet configuration are given in Chapter Eight. First, the velocity flowfield is reported with some discussion outlining flowfield features. Velocity magnitudes are examined along the RCS centerline and at cross-sections normal to the centerline. Measured temperatures are also reported. Throughout this chapter, comparisons are made to the Ashkenas and Sherman relationship [103], which is an empirical relationship derived based on the method of characteristics, used to characterize underexpanded jets.

In Chapter Nine, quantitative data for the RCS parallel jet configuration is reported. A similar analysis used in Chapter Eight is used in Chapter Nine to discuss and note the important flow features and behavior of the parallel jet and the bow shock interactions.

Chapter Ten focuses on the comparison to the computational method. After giving some brief details on the method used, a qualitative comparison of the RCS parallel jet configuration at a jet coefficient of 0.5 is given. Next, the comparison to the quantitative data given in chapters Eight and Nine is examined by focusing on velocity magnitudes within the jet structure.

Chapter Eleven gives conclusions from the research. It also recommends future work that can be used to further study and examine RCS jet interactions.

CHAPTER TWO

PREVIOUS RESEARCH

2.1 Introduction

This chapter discusses work previously completed for laser induced fluorescence, as well as research completed for the reaction control system jets. In examining the works relevant to the research conducted for this dissertation, it is necessary to examine both the research conducted using laser induced fluorescence as well as research involving Reaction Control System jets. Some previous research has been completed using laser induced fluorescence to investigate Reaction Control System jets and this will be also addressed.

2.2 Laser Induced Fluorescence

The use of laser induced fluorescence as an effective visualization technique has been demonstrated through the work of Exton, Danehy and others [37-42]. Wilkes et.al., in a work examining qualitative images of underexpanded jets, compared the results obtained to CFD calculations and found close agreement, showing the effectiveness of using laser induced fluorescence to help validate computational work [42]. The use of laser induced fluorescence as a method to effectively measure temperature, pressure, and velocity in compressible flows has also been investigated and demonstrated through the work of several labs including Niimi, Hiller, and McDaniel [35-36, 43-54]. It was found that the

regimes of continuum and rarefied flows, while both could be adequately modeled and studied using laser induced fluorescence, relied on different methods to obtain various quantitative data. Because of the depopulation of certain iodine transitions at low temperature and pressures, it was necessary to model and examine the hyperfine structure of the remaining populated transition in the range given [55]. Pressure and temperature in the continuum region utilized a variety of data analysis methods, including ratios of peaks and valleys of given parts of the resolved iodine spectrum, as well as height and width of the Voigt profile [35, 47]. Velocity proved to the most accurate of the quantitative measurements taken since it just depends on a frequency shift [21].

2.3 Reaction Control System Research

In reviewing the literature for the research in entry, descent and landing and more specifically, addressing the issues regarding blunt bodies in hypersonic flows interacting with reaction control system jets, there are a number of different aspects of the research under consideration: jet/model configuration (flat plate, thin wedge, blunt body), method of investigation (experimental/computational), test parameters, as well as phenomena investigated (flow physics/heat transfer). In examining the relevant research, three considerations will be considered by examining each of the jet/model configurations: flat plate, sharp cone and blunt body.

Flat plate investigations serve as a benchmark for computational and experimental work. Much of the experimental data for flat plate investigations has been qualitative in nature using the schlieren technique, with the exception of planar laser induced iodine fluorescence work completed at the University of Virginia by David Staack and Eric Cecil

[21, 56]. Viti et.al. and Orth et.al. examined sonic RCS jets exiting into supersonic air freestreams at low temperatures with the purpose of examining aerodynamics and the shock interactions produced [57, 58]. Viti et. Al. further used the experiments to validate computations completed using Reynolds-averaged Navier-Stokes equations coupled with Wilcox's 1998 k-w turbulence model [57]. Tartabini et.al. also compared computations to experiments by comparing experimental data from the European Space Agency to computations completed using Direct Simulation Monte Carlo in order to validate the DSMC [59]. They examined supersonic jets exiting into Mach 20 air freestream in order to gain confidence in the computations. Although the experiments matched well with the computations with the jets not firing, the jet firing case required such complex computations that a lower density was used in the computations than in the actual experiments. Glass and LeBeau examined flat plate geometry of a sonic jet exiting in a Mach 9.84 nitrogen freestream that related to experiments completed in the Low Density Tunnel facility at the Defense Research Agency in Farnborough, UK to compare rarefied DSMC to continuum Computational Fluid Dynamics (CFD) computations, particularly the transition between these regimes [60]. All of these experiments and computations essentially found the basic shock structure of an under-expanded jet issuing into supersonic flow with a distinct barrel shock shape and Mach disk, as well as a bow shock forming upstream of the RCS jet between the freestream and the RCS jet structure. Glass and LeBeau's work also went further and examined density and heating due to the RCS jet on the flat plate.

Sharp cone research focuses mostly on examining missile configurations fitted with side RCS jets. Most of the work examined includes the parameters of a sonic jet of air or

nitrogen issuing into a hypersonic air freestream. Experimental work used schlieren photographs to qualitatively understand the flowfield structure of the jet/freestream interactions, but relied on pressure taps, balance measurements and computational modeling to investigate pressure distributions and the flow physics [61-64]. Zakkay et.al.[61] also used surface dye patterns to examine the flow, while Gülhan et.al.[62] used an oil film technique. It must be noted that, like schlieren photographs, both of these methods give purely qualitative results. Computations by Ebrahimi and others were first validated using experiments and then examined at different flow parameters in order to investigate heating and chemically reaction effects on the jet interactions [63, 64]. In the experimental work, conditions included both laminar and turbulent flow, as well as 2-D and 3-D flow. In all of this work, it was found that there was significant crossflow interactions between the side jet and the freestream which was influenced by the amount of thrust of the RCS jet and less influenced by combustion effects. Ebrahimi and Gülhan et.al. also examined different angles of attack [62, 64].

Since blunt body research is the aim of this research, this type of flowfield was thoroughly examined. A number of different entry vehicle configurations were examined including Apollo, space shuttle, Mars lander, Jovian probe, Orbital Maneuvering Vehicles and Crew Exploration Vehicle geometries. Moss et.al reviewed several blunt body experiments performed in five different hypersonic low-density wind tunnels (Mach numbers ranged from 9 to 20) located in France, Germany and the United States, as well as a flight test performed in Japan, and comparisons of these experiments to CFD and DSMC computations [65, 66]. This study found good correlation between the computations and experiments with its greatest emphasis on pressure and heating distributions on the

surface of the blunt body aeroshell. Romeo and Sterrett and others addressed blunt bodies with forward-facing jets [67-69]. These studies helped establish the field of retropropulsion for both vehicle deceleration and/or reduced heating on the aeroshell, mentioned here because they also established the dimensionless thrust coefficient parameter and the pressure ratio parameters used to compare different experiments. They also formed some of the first experiments conducted on blunt bodies fitted with jets of any kind. Most of the research for jet injection from blunt bodies examines Reaction Control System jets. Several studies investigate RCS jets on different geometries, such as the Orion Crew Module, the Time History of Events and Macroscale Interactions during Substorms satellite mission (THEMIS), and Orbital Maneuvering Vehicle [70-76]. McGregor et.al. examined cold gas (nonreacting) thrusters through DSMC computations and found that the plume from the RCS jet enhances backflow which increases heating in the region where the RCS jets are located [74].

Watkins et.al. experimentally investigated the heating concerns of RCS through the use of pressure- and temperature-sensitive paint [76]. While this work showed proof-of-concept for using these techniques to examine the problem, the data had a lot of noise, requiring more work to accurately investigate augmented heating. A number of works examined the control, design and aerodynamic characteristics of the RCS jets on the space shuttle [77-82]. In these studies, Rausch and Roberts discovered that RCS jets significantly affect the aerodynamics with a degraded performance of yaw and roll conditions due to cross-coupling effects. They also determined that thrust and Mach number could be significant parameters in the effective use of the jets [77]. The use of RCS jets on the space

shuttle provided significant testing and data. However, the geometry of the space vehicle and its RCS jets is significantly different from Mars landing vehicles.

Of more interest is the work that addresses Mars lander vehicle geometries [9, 12, 83-84]. Rault, Cestero and Shane used DSMC to simulate RCS jet interactions during aerobraking in preparation for the Mars Surveyor Program and Mars Global Surveyor flights. This work found in simulations that firing the jets at periapsis, or the point at which vehicle was closest to Mars during the aerobraking maneuver, would generate a torque in the direction opposite from the direction intended but at the same magnitude [12]. This work thus recommended that the use of the RCS jets be avoided. This work also examined the Magellan real flight data during aerobraking and found it difficult to determine the characteristics of the RCS jets from the data given, resulting in the supported theory that the Magellan flew largely RCS-free. Dyakonov et.al. computationally examined the flowfield and pressure distributions for the Mars Pheonix capsule at four different Mach numbers – 3, 18.8, 27.2, and 30.5 – in order to determine the effectiveness of the RCS jets in the different flow regimes. As with the shuttle data, the computations revealed significant cross-coupling effects which gave the jets little authority in the yaw direction and possibly even control reversal [83]. As a result of this study, RCS jets were intended for use only as a secondary method of control and the Phoenix flew as a ballistic uncontrolled nonspinning entry vehicle. Calhoun and Queen looked the control system design for the MSL RCS jet thrusters and concluded that design of a system that allowed for independent control of the yaw and roll channels was of high priority due to the coupling effects [9].

2.4 Laser Induced Fluorescence Investigations of RCS Jets

Cecil and Staack examined reaction control system jets exiting out from a flat plate in Mach 12 flow and measured temperature, pressure and velocity [21, 56]. Cecil observed a strong viscous interaction on the plate and that velocity slip occurred at the surface of the flat plate and found close comparison with DSMC calculations. Danehy and his research group at NASA Langley has also performed significant various tests using NO PLIF to investigate blunt bodies, including those fitted with RCS jets [85-90]. Most of this research involved investigating the Apollo, Orion or Crew Exploration Vehicle module geometries which are all similar in design. Danehy found sufficient signal in order to provide highly spatially resolved images available for comparison to CFD [85]. Inman et.al. also concluded that such visualizations could give real understanding to the fundamental physics of the flow when computations deviate from predicted values [88]. Danehy's work has been successful in examining RCS conditions for use in comparison to CFD, but has yet to produce quantitative measurements from this method [86].

CHAPTER THREE

PLANAR LASER INDUCED IODINE FLUORESCENCE THEORY

3.1 Introduction

This chapter gives the theoretical background for the technique of planar laser induced iodine fluorescence, as well as the method of obtaining quantitative pressure, temperature and velocity measurements using this technique. Since iodine has been chosen as the seeding molecule for this research, the background will be given with regards to rate processes in the iodine molecule. The actual methodology for obtaining the data is given later in the Data Collection section (Chapter Six).

3.2 Laser Induced Iodine Fluorescence

When the iodine molecule is excited by an argon ion laser at 514.5 nm, the molecule absorbs the energy and transitions from the ground electronic, X, state to a higher energy, or excited B state. The B state is only weakly allowed and thus yields a longer lifetime than other absorption transitions [91]. These states are shown in Figure 3.1. Dissociation – in which the iodine molecule splits into free atoms – occurs when the iodine is excited by light energetic enough to cause dissociation to occur [92]. This kind of energy, above the photodissociation energy shown in Figure 3.1, from the excitation source exists with the

argon ion laser at 488 nm but does not at 514.5 nm. For this reason, dissociation does not need to be taken into consideration.
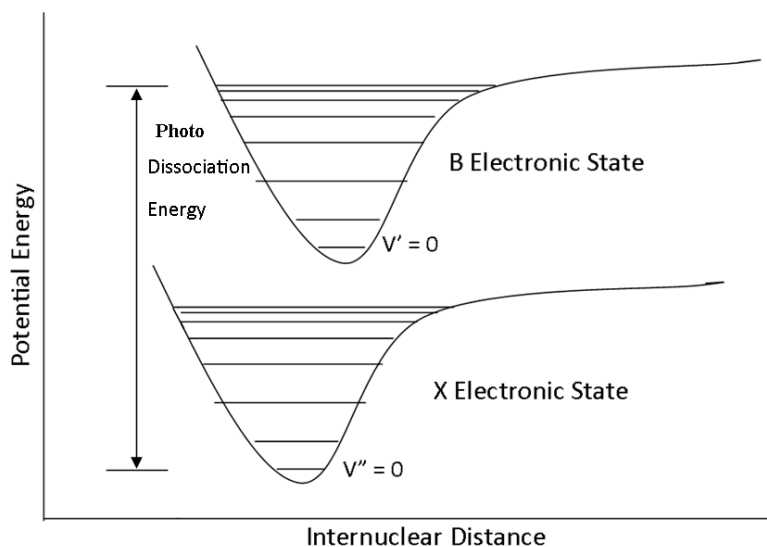
Figure 3.1 Energy wells for B-X transitions

The excitation of the iodine molecule occurs through the absorption rate constant, b_{12}, as shown in the Jablonski diagram in Figure 3.2. Once the molecule is excited, there are several methods by which the molecule will return to its ground state.
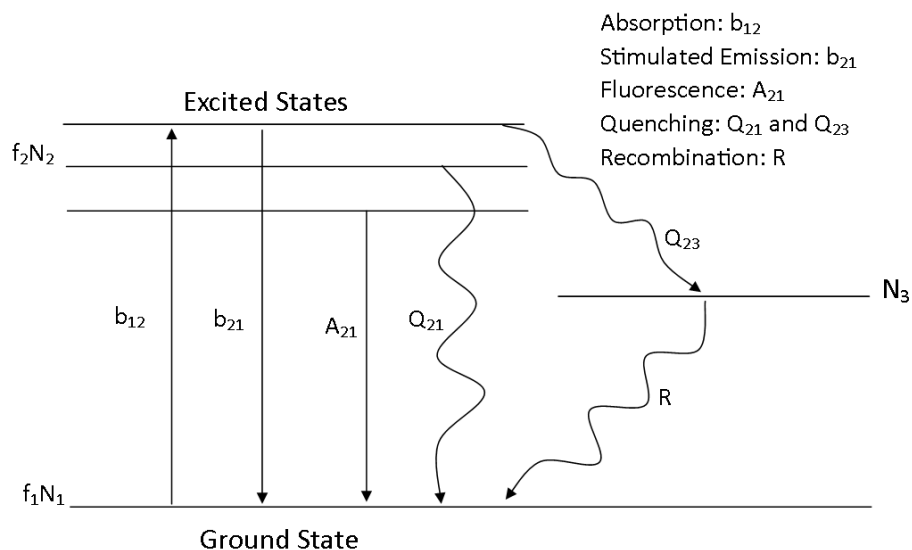
Figure 3.2. Jablonski diagram of excitation and de-excitation of iodine molecule

Stimulated emission, labeled as b_{21} in the figure, is a radiative transfer that occurs to molecules in the excited state in the presence of the excitation light source (argon laser). In this, the molecule releases a photon at the same resonant frequency and returns to its ground state. The number of molecules that radiate through stimulated emission is the product of the number of molecules populating the excited state and the stimulated emission rate constant, b_{21}. In order for stimulated emission to be significant, the excitation light source would need to be very powerful. For this research, due to low operating power levels of the laser (1.5 W), stimulated emission is negligible. Fluorescence, shown in the diagram as A_{21}, is the spontaneous emission of light emitted by the molecule when it decays back to its ground state. Collisional quenching, indicated by Q_{21} in figure 3.2, occurs when collisions between excited and non-excited molecules cause energy transfer back to the ground state without emitting light. Here, Q and A_{21} are averaged values for all observed transitions which decay from the excited energy level, as will be discussed later. Pre-dissociation occurs when the molecule moves from an excited stable state to an excited unstable state before dissociating. Pre-dissociation is possible where two potential energy curves cross each other and excited molecules can cross over to the other state. Given the vibrational levels of the cross-over, molecules can have enough energy to pre-dissociate, via rate Q_{23} [93]. After pre-dissociation, the iodine atoms can recombine (shown as R in the figure) and return to the ground state. Given the excited vibrational levels accessed through the argon ion laser excitation at 514.5 nm, no curve crossovers exist. Thus, in the present application, collisional quenching and fluorescence are the only decay processes of concern.

The entire excitation and decay to the ground state can be described as a two energy level (ground and excited) system and can be modeled in the following rate equation, in which predissociation and stimulated emission are neglected:

$$\frac{dn_2}{dt} = b_{12}\, f_1 n_1 - [\, A_{21} + \, Q]n_2 \tag{3.1}$$

where n is the number of molecules in the given state, and f is the Boltzmann population fraction. The numbers 1 and 2 refer to the ground and excited states, respectively. For steady-state solutions, applicable when using a continuous-wave (non-pulsed) laser, the left-hand side of the equation is equal to zero.

This equation can be solved for the fluorescence signal collected by the detector (in this work, a CCD camera) by including other factors including the intensity of the laser I, the seeding fraction of the iodine molecule in the media, f_s, and the total number density, n, of the flowfield, as well as a constant, C. The resulting equation for the fluorescence signal is given in equation 3.2.

$$S_F = C f_{v''J''}(T)\, \frac{A_{21}}{A_{21}+Q(p,T)}\, \frac{V(p,T,u)}{\Delta v_D(T)} I f_s n \tag{3.2}$$

It must be noted that the constant, C, includes considerations for the optical and geometric factors of the experimental setup, as well as molecular constants such as the Franck-Condon factor and the Hönl-London factor. The Franck-Condon factor is derived from the concept that transitions between the electronic states occur vertically (i.e., the nuclear geometry does not change); therefore, the vibrational level that the molecule transitions to in the upper state will have a state wave function that favorably overlaps the wave function of the initial ground state [93-94]. The Franck-Condon factor, effectively a measure of line strength, is not dependent upon temperature, pressure or velocity, and so remains constant

in the fluorescence signal equation. The Hönl-London factor is a rotational line strength factor which is $J''+1$ for the R branch transitions and J'' for the P branch transitions [97, 108-109], and also does not depend on thermodynamic parameters or velocity, so is included in the constant C.

In this fluorescence model, the amount of signal that can be produced from the fluorescence is dependent on the Boltzmann population of iodine initially in the ground rotational-vibrational energy level excited by the laser. This is shown in the equation as $f_{v''J''}(T)$, in which v'' and J'' are the vibrational and rotational ground-state quantum numbers, respectively, and is temperature dependent. A fluorescence efficiency factor, referred to as the Stern-Volmer factor, is defined as the ratio of fluorescence decay rate to the value of both decay mechanisms, $A_{21}/(A_{21} + Q(p,T))$. The collisional quenching rate, Q_{21}, is related to the collisional frequency and depends on pressure and temperature. The Voigt line shape, $V(p,T,u)$ is a convolution of homogeneous collisional broadening and in-homogeneous Doppler broadening. The lineshape depends on pressure, temperature, and velocity, through the Doppler velocity frequency shift. $\Delta v_D(T)$ is the Doppler line width, which is a function of temperature[95]. The intensity, I, of the continuous-wave laser is low, with the laser operating at a power of 1.5 W throughout the experiment. The seeding fraction of the iodine, f_s, (which will be discussed in more detail in Chapter Four) is about 1 in 10,000 for iodine seeded into nitrogen. The density of molecules is a function of pressure and temperature, assuming the flow is an ideal gas. These contributing factors to the fluorescence signal will be discussed in greater detail below.

3.3 Available Transitions and the Boltzmann Fraction

Under the gain profile of the 514.3 nm argon ion laser, three strong transitions are present: the overlapping R13/P15 lines and the overlapping P48/P103 lines, shown in the figure 3.3 below, as well as the R98 "hot-band" transition.
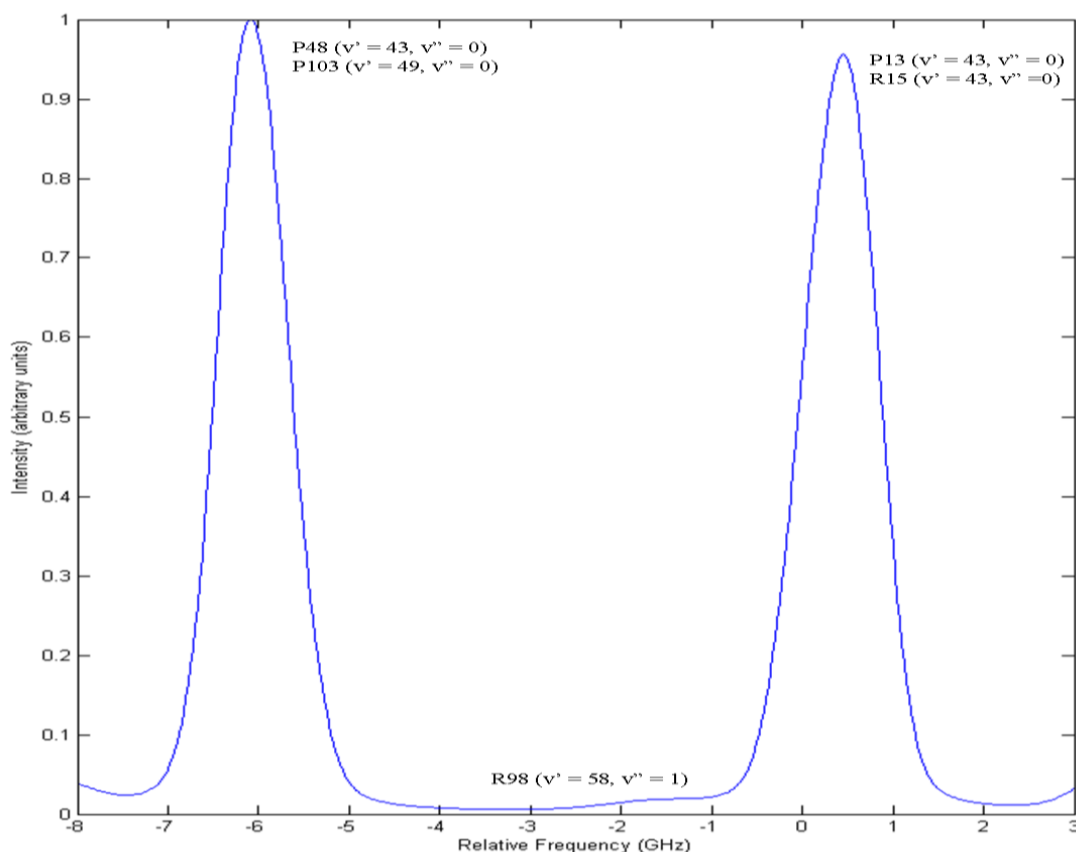
Figure 3.3 Available iodine transitions within laser profile

As stated above, the fluorescence signal is a function of the Boltzmann population of the ground rotational-vibrational state of the iodine molecule. This Boltzmann fraction, $f_{v''J''}$, is defined as:

$$f_{v''J''} = f_{v''} \cdot f_{J''} .$$

(3.2)

The vibrational Boltzmann fraction, $f_{v''}$, and the rotational Boltzmann fraction, $f_{J''}$, are defined as:

$$f_{v''} = \exp\left(-v'' \frac{\theta_{vib}}{T}\right) \cdot \left[1 - \exp\left(\frac{\theta_{vib}}{T}\right)\right] \quad\quad (3.3)$$

$$f_{J''} = \frac{(2J''+1) \cdot exp\left[-J''(J''+1)\frac{\theta_{rot}}{T}\right]}{\frac{1}{\sigma} \cdot \frac{\theta_{rot}}{T}} \quad\quad (3.4)$$

in which θ_{rot} is the characteristic rotational temperature, or 0.0537 K for iodine; θ_{vib} is the characteristic vibrational temperature, which has a value of 308.62 K for iodine; and σ is 2, to account for iodine being a symmetric (homonuclear) diatomic molecule. Plotting these Boltzmann fractions as a function of rotational or vibrational quantum number at various temperatures yields some important characteristics for its contribution to the fluorescent signal.
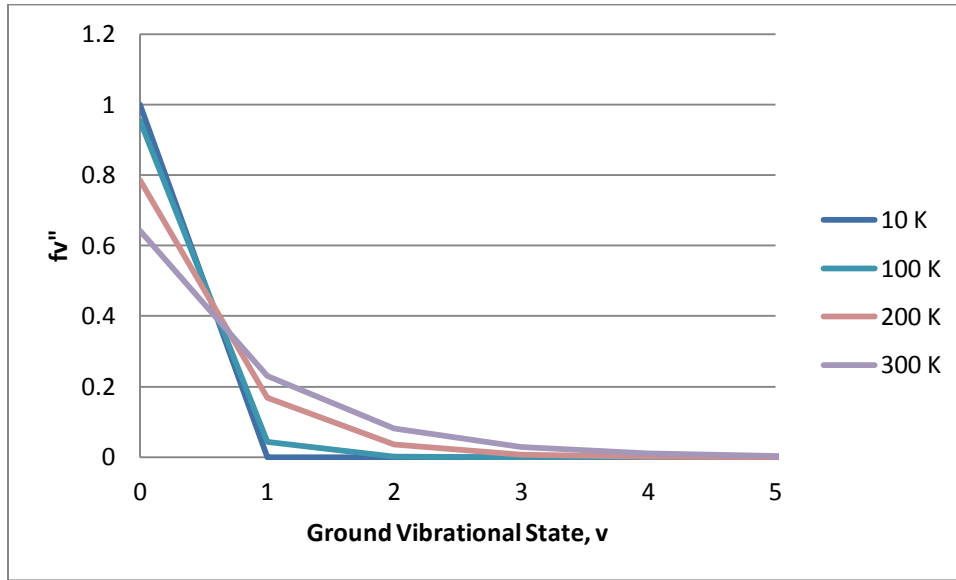
Figure 3.4 Vibrational Boltzmann fraction population distribution

For the vibrational contribution, as shown above in figure 3.4, at the temperatures in the range of the experiment (10-300 K), most molecules will be in the lowest ground vibrational state. At lower temperatures, only the ground vibrational state $v'' = 0$ is

significantly populated. For this reason, the hot band, for which the iodine molecule transitions from a ground vibrational state, v" = 1, is not observed at low temperatures.
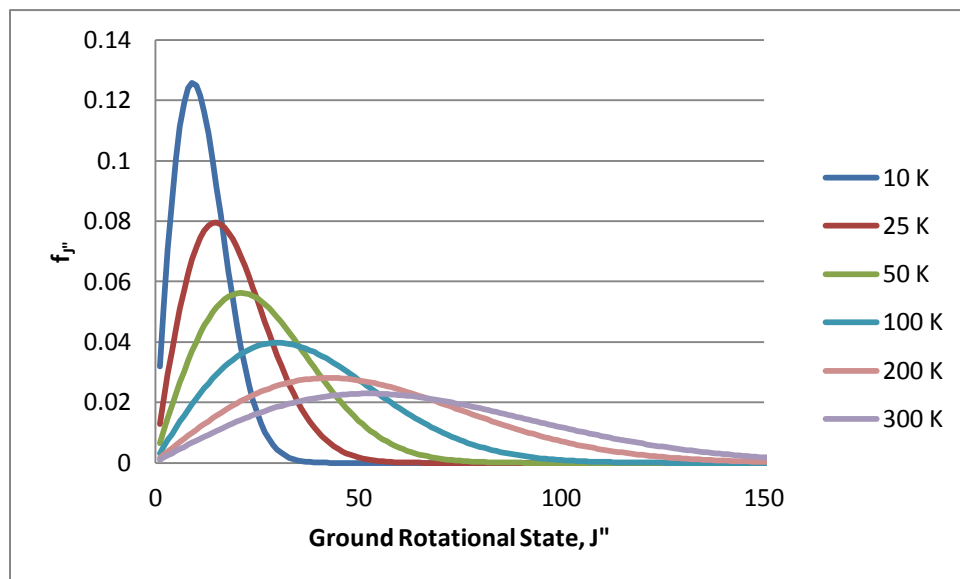
Figure 3.5: Rotational Boltzmann fraction population distribution

The rotational contribution to the Boltzmann fraction is more complicated. At room temperature, the peak for populated energy levels exists at J" = 52 and the P13/R15 (J" = 13 and J" = 14) and P48/P103 (J" = 48 and J" = 103) transitions have relatively low populations. However, as temperature is lowered, the higher rotational quantum numbers depopulate. (It will be seen that the temperature in the experiment can be low as 7 K). Around temperatures of less than 25 K, the P48/P103 transitions effectively disappear. Conversely, at the lower temperatures, the lower rotational energy levels become significantly more populated. At 10 K, the peak of the Boltzmann population fraction population distribution occurs at a rotational quantum number J" = 9. Thus, at low temperatures, the P13/R15 becomes the dominant and sole transitions under the argon ion

tuning range. This rotational population fraction for the P13/R15 transitions is critical to the use of PLIIF in low temperature flows.

3.4 The Stern-Volmer Factor

The Stern-Volmer factor is essentially an efficiency factor that indicates the effect of quenching on overall fluorescence. The Stern-Volmer factor can be reduced to a simplified form in the following equation:

$$\frac{A_{21}}{A_{21}+Q} = \frac{1}{1+\frac{Q}{A_{21}}}$$
(3.5)

in which the Stern-Volmer factor can now be reduced to one variable – the quenching rate, Q, normalized by the constant fluorescence decay rate. Donohue experimentally developed a relationship for this normalized quenching rate as [96]:

$$\frac{Q}{A_{21}} = C_q \frac{P}{T^{0.5}}$$
(3.6)

in which C_q is the quenching coefficient and p is the pressure, given in kPa. This quenching coefficient has been determined as 2.1 $K^{0.5}$/kPa.

3.5 Voigt Lineshape

The transition lines are subject to different type of broadening, resulting in a lineshape. Natural lifetime broadening occurs due to the Heisenburg uncertainty principle which indicates that it is impossible to know with any certainty the exact quantum level the molecule populates [93]. The iodine diatomic molecule has a reported natural lifetime of 2.9E^{-6} s [30, 112]. By including quenching considerations at room temperature and standard pressure, an effective lifetime can be calculated as 2.2E^{-7} s [26, 96]. This results in

iodine transitions that have some natural width, resulting in a homogeneous lineshape. Collisional broadening (also known as pressure broadening) occurs when molecules collide randomly, resulting in a homogeneous or Lorentzian lineshape [97]. Collisional broadening was experimentally determined as [96, 98]:

$$\Delta \nu_C = C_b \frac{P}{T^{0.7}} \qquad (3.7)$$

where C_b is the broadening constant, with a value of 4.2 GHz K$^{0.7}$/kPa. Doppler broadening occurs due to molecules having a distribution of velocities and results in an inhomogeneous or Gaussian lineshape. The Doppler lineshape, $\Delta \nu_D$, is a function of temperature and is defined as [97, 99]:

$$\Delta \nu_D = \sqrt{\frac{8 \ln(2) kT}{mc^2}} \nu_0 \qquad (3.8)$$

in which k is the Boltzmann constant, m is the mass of the molecule, c is the speed of light and ν_0 indicates the line center frequency. At high temperatures and low pressures, Doppler broadening will dominate, while conversely, at low temperatures and high pressures, the collisional linewidth will be much greater than the Doppler linewidth. In between these two extremes, both types of broadening are present and so a convolution of the two must be considered in order to adequately describe the total lineshape [97]. Thus the lineshape of the iodine transitions is best characterized as a Voigt lineshape and is a function of pressure and temperature.

At very low temperatures and pressures, where collisional broadening and Doppler broadening are both reduced, a hyperfine structure appears in the P13/R15 lineshapes [85]. The appearance of this hyperfine structure is a result of the interaction of nuclear and molecular spin (i.e. the angular momentum is slightly varied due to the nuclear spin of the

27

iodine atoms in the diatomic molecule [56, 91, 93-94]) and consists of 21 transitions for odd rotational quantum numbers and 15 transitions for even rotational quantum numbers [91].

3.6 Doppler Shift

Doppler shift of the transition line center frequency and is caused by the "tuning" of the transition to a higher or lower frequency due to the molecule's velocity with respect to the laser propagation direction. Molecules that are moving towards the laser will "see" the laser at a higher frequency and will be appropriately blue-shifted (to higher frequency) with respect to a stationary molecule for the same laser direction. Likewise, molecules that are moving away from the laser will "see" the laser red-shifted (to a lower frequency) compared to a stationary molecule. The amount of shift is directly proportional to the velocity component of the molecule with respect to the laser's direction. Doppler shift is represented in the following equation, in which c is the speed of light, u is the velocity of the moving molecule, v is the frequency of the excitation source and v_0 is the frequency observed by a stationary molecule:

$$v = \left(\frac{c+u}{c}\right) v_0. \tag{3.9}$$

This equation can be solved for the Doppler frequency shift:

$$\frac{\Delta v_{Doppler}}{v_0} = \frac{u}{c} \, , \; where \; \lambda_0 v_0 = c. \tag{3.10}$$

λ_0 is the wavelength of the argon ion laser (or 514.5 nm) and $\Delta v_{Doppler}$ is the Doppler shift in frequency. Solving for velocity then yields the result:

$$u = \lambda_0 \Delta v_{Doppler} \tag{3.11}$$

(This should not to be confused with $\Delta\nu_D$, which denotes the Doppler line width.) The shift is measured by comparing the observed frequency of the lineshape in the flowfield with respect to the lineshape in a static cell of molecules with zero velocity.

3.7 Impact Shift

The line center can also be shifted due to collisions that occur between molecules, known as impact shift. This impact shift has been experimentally determined as:

$$\Delta\nu_I = C_I \cdot \frac{p}{T^{0.7}} \qquad (3.12)$$

where C_I is a constant which was determined experimentally with a given value of -0.39 GHz*K$^{0.7}$/kPa [96]. Impact shift is not directional like the Doppler shift, in that it always reduces line center frequency irrespective of laser propagation direction. At standard pressure and room temperature, the impact shift is not a negligible effect, accounting for as much as 50% of the shift of the line center. In some cases, this impact shift can be cancelled using a counter-propagating beams approach or by through the use of flow symmetry [35, 100-101]. However, in the case of this research, neither method is available due to the complex geometry of the model and experimental set-up. Impact shift, however, does decrease linearly with pressure. Thus, at the low pressures of this experiment, the impact shift will become negligible and can be neglected.

3.8 Qualitative Measurement

Laser-induced iodine fluorescence can be used as a powerful qualitative, spatially-resolved imaging technique. To do this, the laser can be operated in broadband mode and all the resulting fluorescence is collected using a CCD camera. When the argon laser is in

broadband mode, the lasing linewidth (about 10 GHz) exceeds the iodine transition linewidth (about 1.5 GHz for the P13/R15 transition at room temperature and pressure), resulting in several iodine transitions being excited at once. The fluorescence signal equation, described in 3.2 can be reduced to the following:

$$S_F = C f_{v''J''} \frac{A_{21}}{A_{21}+Q} I f_s n \qquad (3.13)$$

For the broadband fluorescent signal equation, the Voigt lineshape has been effectively integrated over all frequencies in equation 3.2 and is normalized to give a value of unity. The broadband fluorescent signal is a complex function of pressure and temperature, which are not known a priori in a flowfield; therefore, fluorescent imaging is qualitative in an unknown flowfield. It will be shown that this fluorescent broadband signal can be used to capture planar images of flow features with sufficient signal to highlight important flowfield characteristics, such as shock structures, jets and shear layers. Qualitative imaging can be used in rarefied, continuum and mixed rarefied/continuum flows for high-quality, spatially resolved images [49, 102].

Due to the nature of the signal, though, it is also possible to use the qualitative images for semi-quantitative analysis. Using isentropic relations for expansion from stagnation conditions (p_0 = 183 kPa and T_0 = 298 K) temperature and pressure can be determined versus Mach number. Therefore, the Stern-Volmer factor and Boltzmann fraction can be plotted versus Mach number, as shown in figure 3.6 and 3.7. These Mach numbers are typical of the conditions in the experiment.
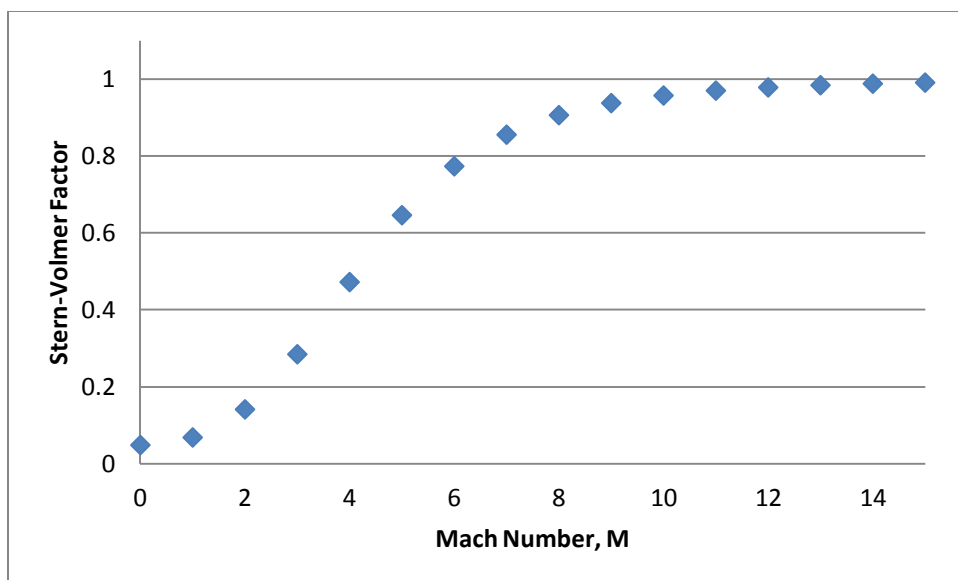
Figure 3.6 Stern-Volmer factor at various Mach numbers

As shown in the plots, at higher Mach numbers, the Stern-Volmer factor approaches and reaches a value of one. This is because in rarefied conditions, collisions between molecules are greatly reduced and so quenching goes to zero.
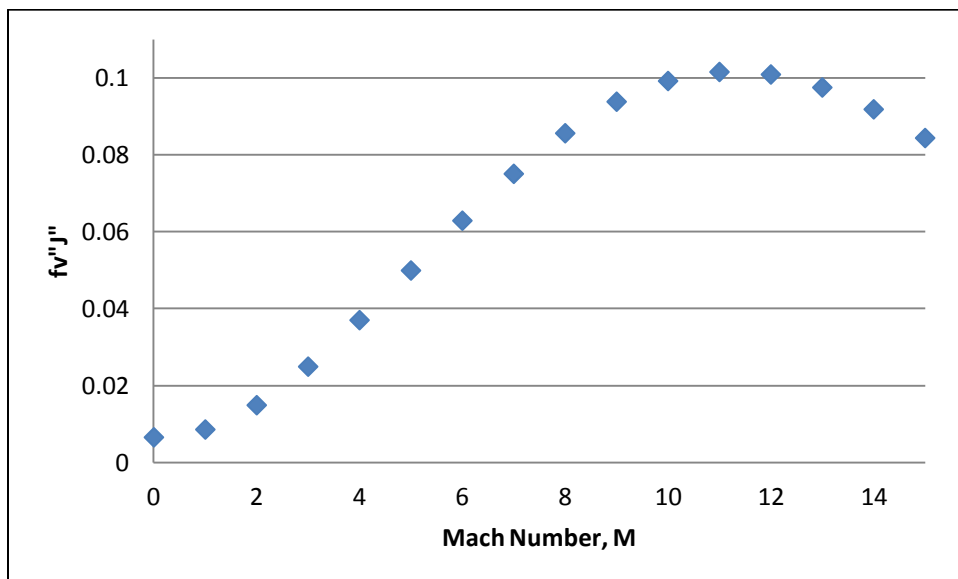
Figure 3.7 Boltzmann fraction population distribution for P13/R15 peak

The Boltzmann fraction does not asymptote to one but does tend towards a roughly constant value in the Mach 8-14 range. By multiplying the Stern-Volmer factor and the Boltzmann population distribution for the P13/R15 peak and plotting it, as in figure 3.8, a similar trend to the Boltzmann fraction can be seen.
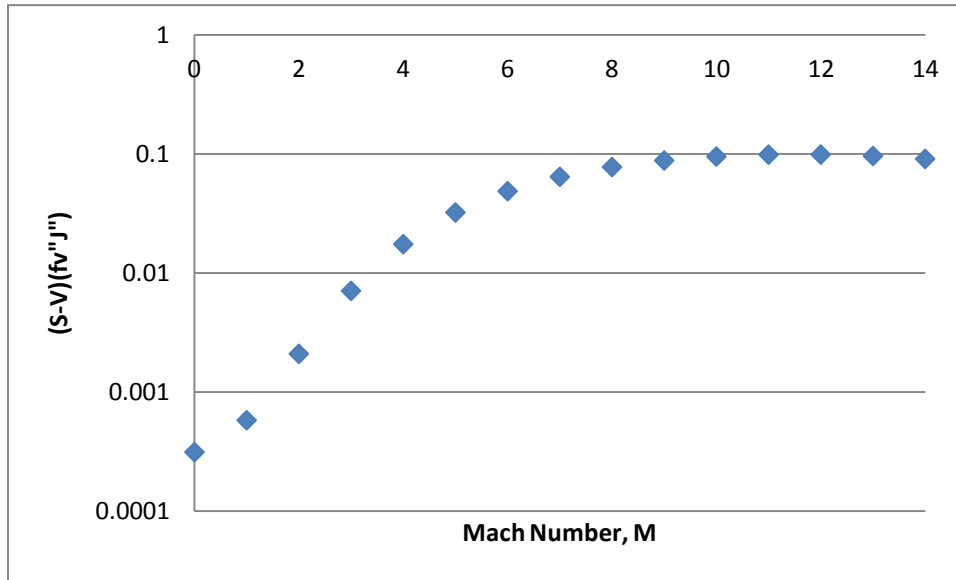
Figure 3.8 Product of Stern-Volmer factor and Boltzmann population fraction, plotted on semi-logarithmic scale.

At higher Mach numbers, a roughly constant value is reached. As such, the fluorescence equation then consists of several factors that are all constants at higher Mach numbers, above about Mach 5 (with 5% error), multiplied by the number density. Thus the fluorescence signal equation at Mach numbers greater than 5 (for the stagnation conditions of this experiment) can be considered a direct function of density and can be used to measure the density of the flow. This makes the broadband approach quantitative in its ability to measure number density in the rarefied flow regime.

3.9 Quantitative Measurement

When the laser is operated in narrowband mode, in which the laser linewidth is much narrower than the iodine transition linewidth, it is possible to exploit the thermodynamic properties of the iodine transitions available in the laser profile to obtain quantitative measurements. As described in the background above, the fluorescence signal and lineshape are functions of pressure, temperature and velocity due to Doppler shifts. In the laser narrowband mode, within the argon ion laser's gain profile width of 10 GHz, small frequency steps on the order of 10's of MHz can be accessed through laser tuning. A given, tuned frequency will resonate with rotational and vibrational energies of the iodine molecule and excite it to a higher energy level, where it will undergo the various processes of decay described previously. The resulting fluorescence from the excitation will decay at shorter frequencies (longer wavelengths) than the excitation frequency in a phenomenon known as the Stokes shift. This shift usually occurs because fluorescence will decay within the excited electronic state to lower ro-vibrational energy levels through collisions before decaying through spontaneous emission [93]. Using a long-pass filter on a CCD camera, all the shifted fluorescence emission is collected, removing the detailed spectroscopy of the emission spectrum. The resulting C_q and C_b that go into equation 3.2 are constants for this collected signal and independent of the specific value for each fluorescence emission line. Thus, the fluorescence collected can really be seen as a measure of the absorption at the given excitation frequency. (In other words, equation 3.2 for the fluorescence is actually an equation for the absorption spectrum with broadband fluorescence signal collection. The fluorescence is used to obtain spatial resolution at a point along the line-of-sight absorbing laser beam.) By tuning through the small frequency steps through the profile of the argon

ion laser, the fluorescence collected at each frequency can be plotted versus excitation frequency, producing an absorption spectrum. Due to the fluorescent signal's dependence on pressure, temperature and velocity, it is possible to numerically fit the measured absorption spectrum to the fluorescent model and extract this information from the flow.

For a Planar Laser Induced Iodine Fluorescence (PLIIF) image, a CCD camera is able to capture fluorescence at every pixel in the 2-D region of interest and thereby obtain an absorption spectrum at each point in the flowfield. At each pixel, the absorption spectrum is subject to the temperature, pressure and velocity of the flowfield corresponding to that point imaged on the CCD. The Planar Laser Induced Iodine Fluorescence methodology involves numerically fitting the data at each pixel to a theoretical model of the fluorescence. This results in a measurement of pressure, temperature and velocity to each point in a given 2-D region of interest in the flowfield. The approach taken to determine these individual properties is described next.

3.10 Thermodynamic Dependence

As discussed before, the Voigt profile and absorption spectrum of the iodine transitions across the laser gain profile are subject to pressure and temperature broadening. In figure 3.9, a range of different spectra of the P13/R15 transitions is given at discrete Mach numbers. Their corresponding thermodynamic conditions are calculated from isentropic relations at each Mach number for expansion from stagnation conditions. These spectra are indicative of the types of spectra that will be encountered in the flowfield, due to its characteristics as an isentropic underexpanded jet, as will be discussed in more detail in the following chapter.
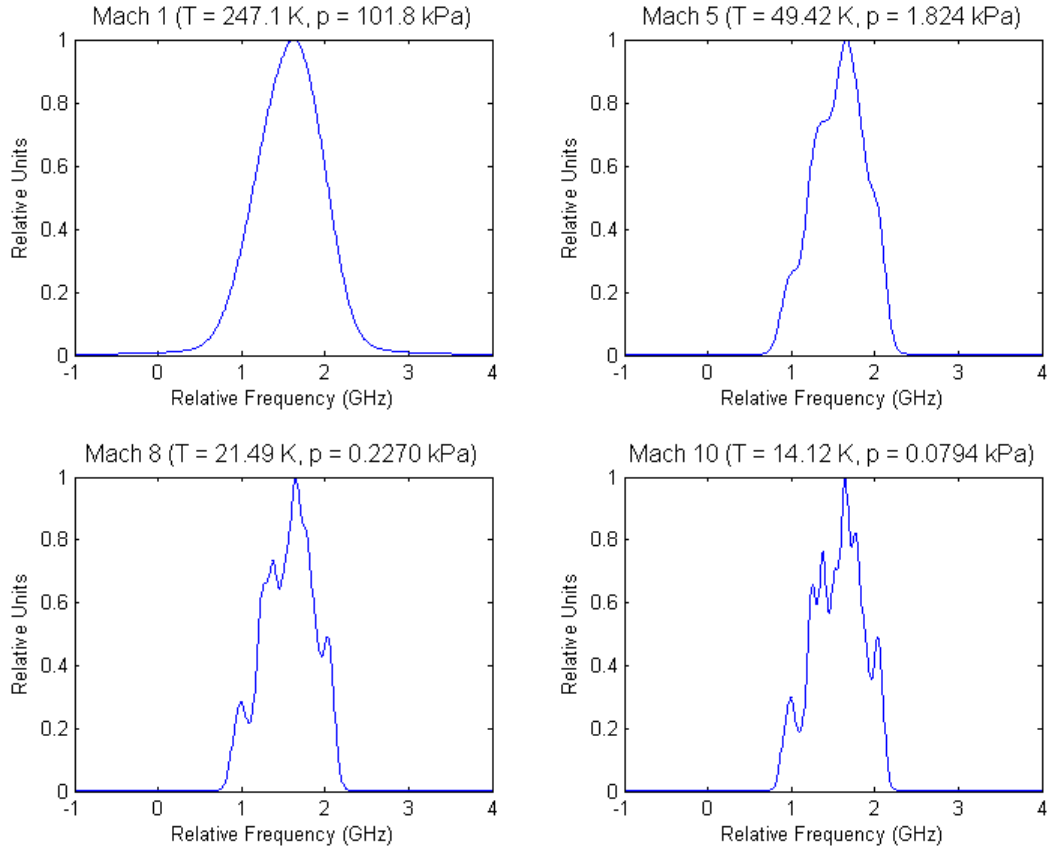
3.9 Iodine absorption spectra at discrete Mach numbers for an isentropic expansion (p_0 =183 kPa, T_0 = 298 K)

At Mach 1, the combined collisional and Doppler broadening result in a lineshape that is distinct, for a given pressure and temperature. This results in a smooth Voigt lineshape in the continuum regime. At higher Mach numbers, and lower pressure and temperature, the hyperfine splitting of the P13/R15 absorption line appears, as seen at Mach 5. By Mach 10, the hyperfine features are fully resolved. At this low pressure condition, the collisional broadening is negligible and the spectrum is purely Doppler broadened.

To solve for temperature and pressure, a resolved absorption spectrum is numerically fitted using the iodine fluorescence model (equation 3.2). This iodine fluorescence model effectively provides a database of the available iodine absorption

spectra under the argon ion laser gain profile. In the high Mach number, rarefied regime, the pressure measurement is subject to error, due to low sensitivity of the model to collisional broadening. Temperature, on the other hand, is more accurate in the rarefied regime because of the sensitivity of the hyperfine absorption spectrum to temperature.

3.11 Velocity

By taking advantage of the Doppler shift that occurs due to the velocity component of a molecule with in the direction of the excitation light source, it is possible to use PLIIF to derive quantitative measurements within a plane. However, the total frequency shift includes both a shift due to the Doppler effect and a shift due to collisions, as mentioned previously:

$$\Delta \nu_{Tot} = \Delta \nu_D + \Delta \nu_I \qquad (3.14)$$

In order to obtain this total frequency shift, the laser is tuned in a single longitudinal mode across the argon gain profile to produce the PLIIF spectrum of the excited iodine molecules throughout the plane of the flow. Simultaneously, the laser excites iodine molecules in a static cell at known temperature and pressure conditions and the static, unshifted, absorption spectrum is also generated. The spectrum of the P13/R15 transition is found in the static cell and compared to the spectra within the flow to calculate the total frequency shift between the static cell and each point in the flow. The spectra in figure 3.9 at the discrete Mach numbers are shown in figure 3.10 with respect to a static, unshifted spectrum. Using the thermodynamic properties at each Mach number, impact shift and Doppler shift are calculated and shown as parts of the total frequency shift expected for

these flow and conditions. Note that these spectra are for a fixed laser sheet direction, giving the same velocity component for each spectrum. It can be noted that at Mach 1, impact shift represents a significant part of the total frequency shift, whereas at Mach 5, it represents a much smaller part of the total shift and is negligible at the higher Mach number of 8.
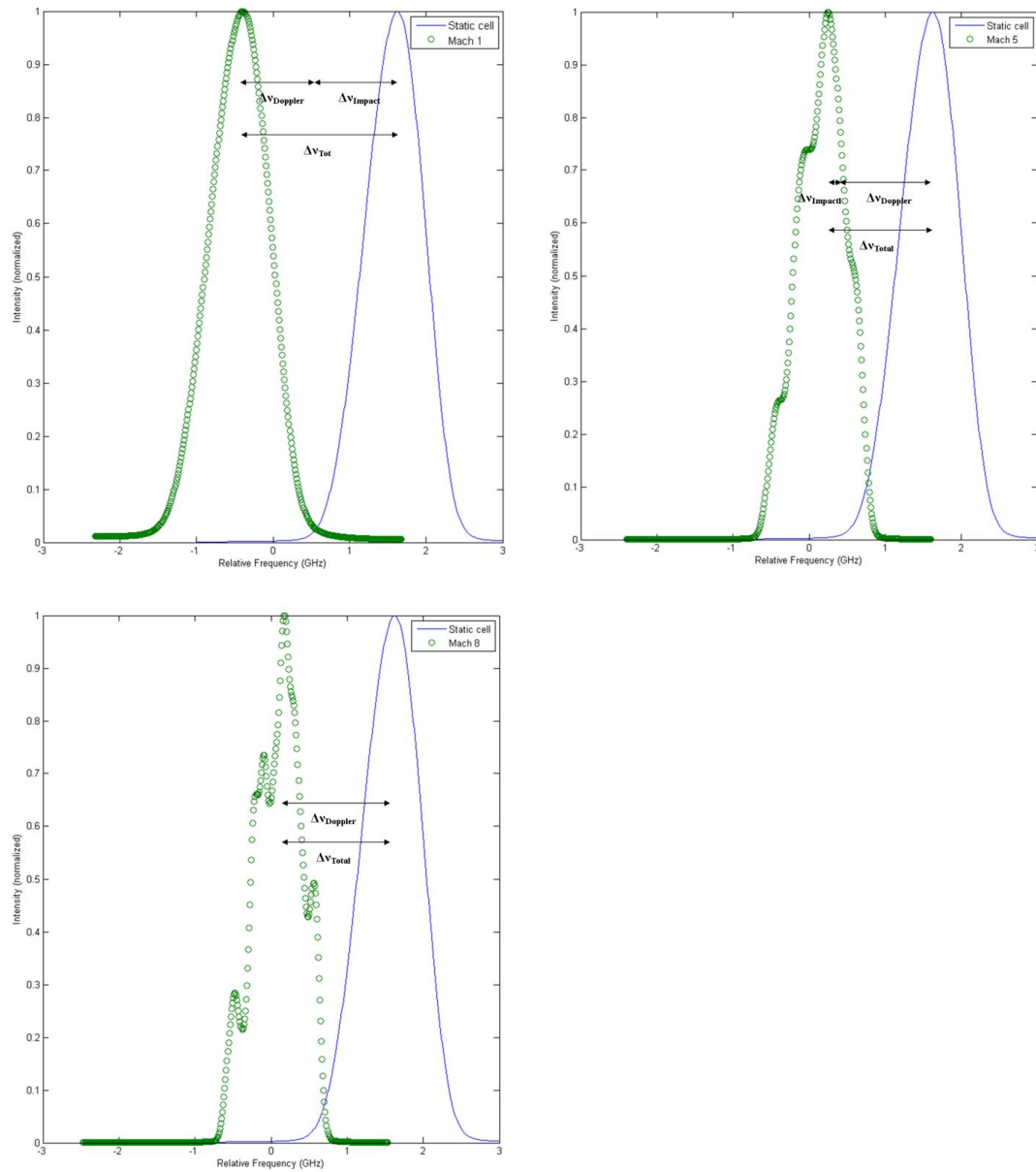
3.10 Spectra at Mach 1, 5 and 8 with Doppler and impact shift with respect to unshifted spectra with same laser sheet direction

To solve for the Doppler shift in frequency, it is necessary to first subtract the impact shift. Velocity can then be solved for by the following equation:

$$u = \lambda_0 \left(\Delta v_{Tot} + \frac{39.05p}{T^{0.7}} \right)$$ (3.15)

The Δv_{Tot} is the difference between the flowfield line center frequency and the static cell line center frequency of the P13/R15 peak. This yields the velocity in the direction of the laser sheet. In order to obtain 2-D planar velocity, it is necessary to use two laser sheet angles to measure two components of velocity. It is ideal if these two laser sheet angles are well separated in order to provide an accurate 2-D velocity vector. However, when using any two laser angles, it is possible to complete a transformation of the two laser sheet angles into x-y coordinates. Given a velocity, u_1, in the direction of θ_1 and a second velocity, u_2, in the direction of θ_2, the following equations may be applied to give u_x and u_y [21]:

$$u_x = \frac{-u_1 \cos\theta_2 + u_2 \cos\theta_1}{\sin(\theta_1 - \theta_2)}$$ (3.16)

$$u_y = \frac{u_1 \sin\theta_2 - u_2 \sin\theta_1}{\sin(\theta_1 - \theta_2)}$$ (3.17)

Using this transformation, two velocity components are obtained and can be used to produce planar measurements. In previous PLIIF measurements, velocity has been reported to have an accuracy of 5 m/s in certain thermodynamic conditions [21]. In this research, an error analysis was performed. At hypersonic conditions (above Mach 5), the error in temperature in an isentropic expansion is less than 10 % and the error in velocity is less than 6%. An error analysis of velocity, temperature and pressure is given in Appendix A.

The equation 3.15 shows how the accuracy of velocity is dependent on pressure and temperature because of the necessary inclusion of impact shift. In continuum regions of the flow where pressures and temperatures are high, impact shift is an important factor. If miscalculated, this can result in large errors in velocity calculations. In some isolated, high pressure regions of the flow in this experiment, shifts due to impact can be as large as 1 GHz, resulting in error in a velocity component of over 500 m/s, accounting for as much as 50% of the total shift measured.

Impact shift does become negligible in rarefied conditions and can be assumed to be zero. Due to the low pressure conditions in the vacuum chamber for this research and the rarefied conditions that the RCS jet is exiting into, the flow quickly becomes rarefied (within 3 jet diameters from the jet exit) and impact shift can be neglected for most of the flow. It only becomes significant in shear layers and shock waves and close to the jet exit. In these situations, a good calculation of temperature and pressure are required to calculate the impact shift and correct for it in velocity measurements.

CHAPTER FOUR

EXPERIMENTAL SET-UP

4.1 Introduction

The experimental set up for the PLIIF technique is quite complicated and requires several different systems to work together in order to achieve the desired experimental characteristics. In this chapter, the wind tunnel set up, laser system and the CCD camera/optical setup will be discussed. This chapter will mostly focus on the capabilities and performance of each system. Details regarding the design of the experiment and data collection are discussed in later chapters.

4.2 Low Pressure System

In order to obtain the supersonic/hypersonic flowfield, a vacuum is created in a large chamber using a Stokes rotary vacuum pump, as well as two Roots booster pumps, that can continuously evacuate the chamber and maintain pressures on the order of 10 mTorr, or 1.31×10^{-5} atm. Industrial-grade nitrogen (99.998%) is introduced into this

low-pressure from a stagnation chamber through a 2 mm diameter orifice. This orifice chokes the flow, creating sonic conditions at the orifice exit, which then rapidly expands into the low-pressure background as a highly underexpanded jet, shown in figure 4.1.
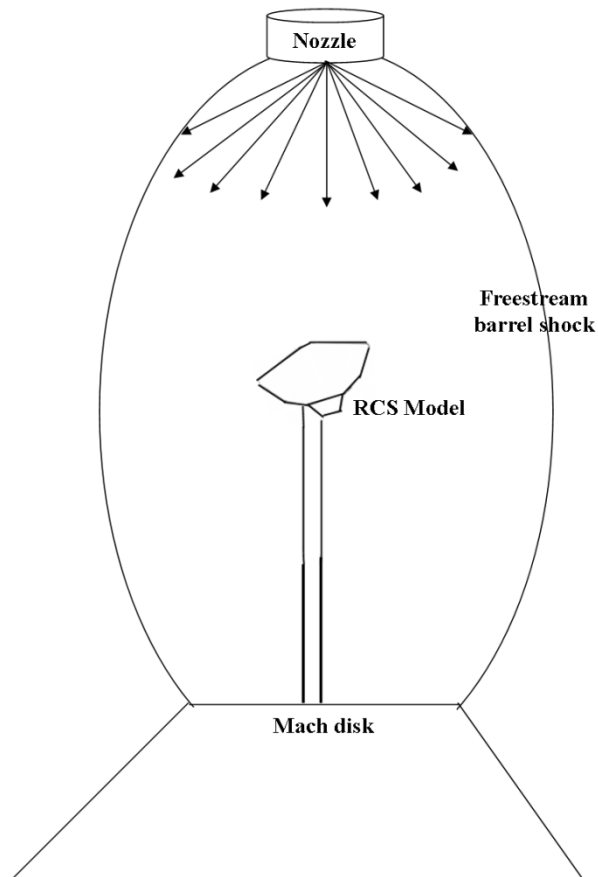
Figure 4.1 Schematic of freestream underexpanded jet structure.

This flow in the underexpanded jet increases, referred to as the freestream, in speed as it expands farther away from the nozzle, resulting in variable conditions from sonic up to about Mach 16 before terminating in a Mach disk shock wave. After the Mach disk, conditions return to subsonic. Moving laterally away from the orifice, the flow radiates

outward before passing through a barrel shock. This type of highly structured, underexpanded jet has been well-studied and characterized by a study completed by Ashkenas and Sherman [103]. In their study, Ashkenas and Sherman show that, along the centerline of this jet, the Mach number (M) of the flow inside the supersonic/hypersonic jet structure can be calculated with respect to the distance from the orifice (x). This is shown in equation 4.1 in which A = 3.65, γ = 1.4 (for nitrogen gas), the effective source of the flow, $x_0/D = 0.40$ and D is the diameter of the nozzle [103]. This relationship will apply for the freestream flow, as well as the core of the RCS jets.

$$M = A \left(\frac{x-x_0}{D}\right)^{\gamma-1} - \frac{1}{2}\left(\frac{\gamma+1}{\gamma-1}\right)A^{-1}\left(\frac{x-x_0}{D}\right)^{-(\gamma-1)} \tag{4.1}$$

Using this equation, if a model is placed within this freestream jet structure at a specific point from the freestream nozzle exit, one can determine the freestream Mach number for the model, as shown in figure 4.2.
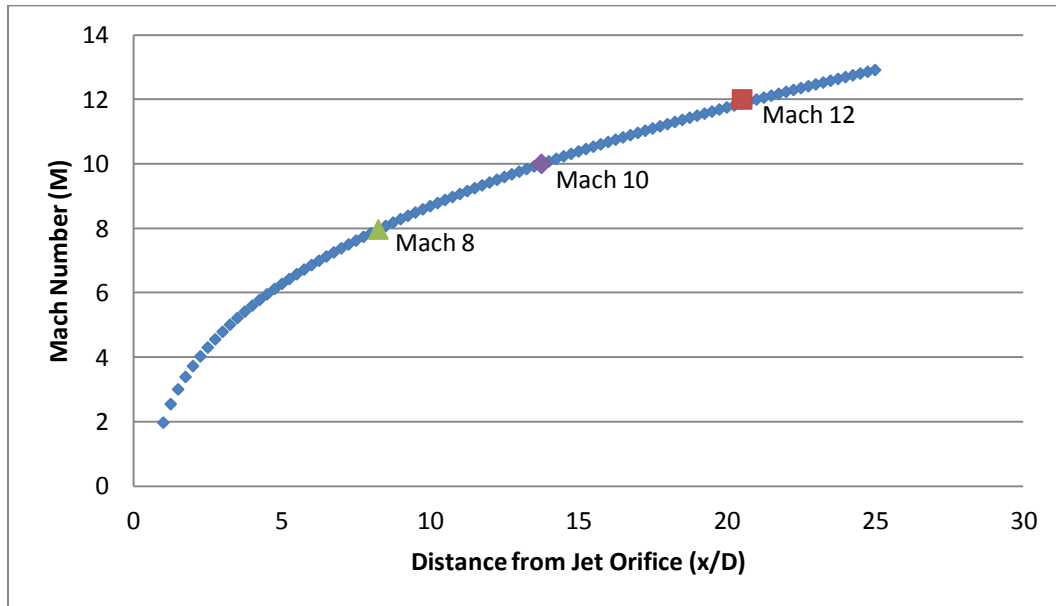
Figure 4.2 Ashkenas and Sherman relationship for Mach number versus x/D.

42

Once the Mach number is known, the thermodynamic properties and velocity can be determined using isentropic relations. Hence, this jet structure becomes an effective test section with variable Mach number and thermodynamic and velocity conditions along the centerline. For this work, Mach 12 conditions were desired, which would require putting the model at a distance from the orifice of 42.03 mm, or freestream x/D =21.0. The jet structure for this facility has been compared to the Ashkenas and Sherman study and found that it is consistent with their relationship in equation 4.1 [49, 85]. This Ashkenas and Sherman study is also very important for the study of RCS jets as the sonic, RCS jets exit the model in low-pressure conditions behind the shoulder of the model, forming an underexpanded jet structure.

Because the underexpanded jet is expanding into a near vacuum, temperatures decrease rapidly from room temperature to around 10 K at Mach 12, thus making this facility effective at achieving high flight Mach numbers and rarefied conditions; however, it is inadequate at achieving and investigating high-temperature effects that would exist on a blunt body in re-entry conditions. This facility is well-suited to provide a fundamental understanding of the aerodynamics involved in RCS jets and its various interactions.

During the experiment, the stagnation chamber is maintained at a pressure of 1.8 atm or 26.5 psia (183 kPa). When this flow is introduced into the chamber, the pumps are able to maintain a backpressure of around 250 mTorr ($3E^{-2}$ kPa). The pumps are further helped to evacuate nitrogen, and seeded with iodine, by cooling the baffle at the bottom of the chamber with liquid nitrogen from a 240 L tank. When the RCS jet is introduced into

the chamber as well, a backpressure can be maintained at 300 mTorr ($4E^{-2}$ kPa) for lower thrust coefficients and 450 mTorr ($6E^{-2}$ kPa) for higher thrust coefficients.

4.3 Flow Buffer Gas

Dry nitrogen gas from a bank of nitrogen cylinders is used as the buffer gas for this experiment, both in the freestream and in the RCS jet. In order to use the PLIIF technique, the nitrogen is first introduced into a mixing vessel that holds trays of solid iodine pellets. When the nitrogen flows over the trays, the iodine sublimates into gaseous form and mixes with the nitrogen gas. The seeding fraction of iodine in nitrogen is dependent on the partial pressure of iodine. The partial pressure of iodine is highly dependent on temperature; in fact, the amount of iodine seeded in nitrogen doubles with every 10 degree increase in temperature, on the Celsius scale. The partial pressure of iodine at room temperature is 0.3 torr. Room temperature (65°F) is maintained in the mixing vessel by use ceramic space heater. This space heater is used to reduce effects from outside temperatures, where the nitrogen is stored, and to heat the nitrogen while in the mixing vessel before its introduction into the low-pressure chamber.   The iodine seeding fraction is the vapor pressure of iodine, divided by the stagnation pressure in the mixing vessel. This seeding value at room temperature and an operational mixing vessel pressure of 45 psig, produces an iodine seeding fraction of iodine is 1 in 10,288 parts nitrogen. This seeding fraction is sufficient to provide adequate signal in the flow even in a mixed/rarefied regime. Without condensation, this seeding fraction is constant in the flowfield.   No evidence of condensation on any of the surfaces has been detected.

Due to iodine's corrosiveness, a number of precautions and considerations were made with regards to the experimental setup. The pressure gages which were used to monitor main jet pressure, RCS jet pressure and the back pressure in the vacuum chamber included diaphragms that were made of chemically resistant materials. Carbon filters were also installed in order to scrub out the iodine and not damage the instruments.

The tubing for the entire system consists mostly of Teflon®, which is impervious to iodine. Where fittings are required, 416 stainless steel is used which is not entirely resistant to iodine but holds up better than other materials. The tubing to the model inside the wind tunnel is made of Tygon®. It is not as resistant to iodine as Teflon but is more flexible and could be stretched to fit over the model mounting sting. Although the iodine results in high discoloration, it does not affect the integrity of the tubing material, which could result in failure during an experiment. To prevent this from happening, this tubing is also replaced every few runs.

4.4 Laser and Optics System

The experiment uses a Spectra Physics 2080A argon ion laser, running on the 514.5 nm line. The laser power is typically only used at a value of 1.5 W (maximum for this laser is 10 W, 5 W with an etalon.) By running at a lower power, the profile for the laser can access 10 GHz under the gain profile of the laser without losing power at the ends of the tuning range. By scanning the laser across this 10 GHz, the P13/R15 peak, as well as part of the R48/P103 peak and the R98 peak, can be accessed. The P13/R15 peak, which is of greatest interest for mixed-rarefied regimes, is located off-center of this profile (shown in

figure 3.3). The laser can be scanned through its profile using an etalon, located in the laser cavity, which selects specific longitudinal laser modes. By using a stepper motor that is attached to a gear on the etalon, coarse scanning at step sizes of 87 MHz can be obtained. In a scan across the entire profile, this would give 115 discrete frequencies and about 23 discrete frequencies across the width of the P13/R15 peak. By using the computer to control a piezo-electric transducer on the laser output mirror (whose normal primary function is to reduce jitter of the laser signal) a finer scan can be obtained with step sizes as small as 20 MHz. This finer scan can give 500 discrete frequencies across the laser profile and 100 discrete frequencies across the R13/P15 peak, which is an order of magnitude finer frequency steps than without the transducer. Because there are several regions in the laser profile without absorption features, usually scans are completed using the smaller step sizes across the P13/R15 peak and the P48/108 peak and then using the larger step sizes across the low absorption areas of the profile. Using this method, a full scan across the profile typically consists of 350 discrete frequencies.

The laser frequency is highly dependent on temperature. A temperature increase in the laser cavity results in a change in the cavity length, which changes the frequency of the laser. Temperature changes can also affect laser beam drift and mirror misalignment unless the laser is continually monitored and the laser sheet on the model is readjusted. In order to reduce temperature changes, the laser uses an etalon heater to help maintain a uniform temperature in the etalon throughout the experiment. The laser also is water-cooled using a water pumping system from a pit below the lab (and in another room) in which cooling water from a reservoir is passed through a heat exchanger to cool the closed water loop in the laser system.

The entire set-up with the laser system is shown in figure 4.3.
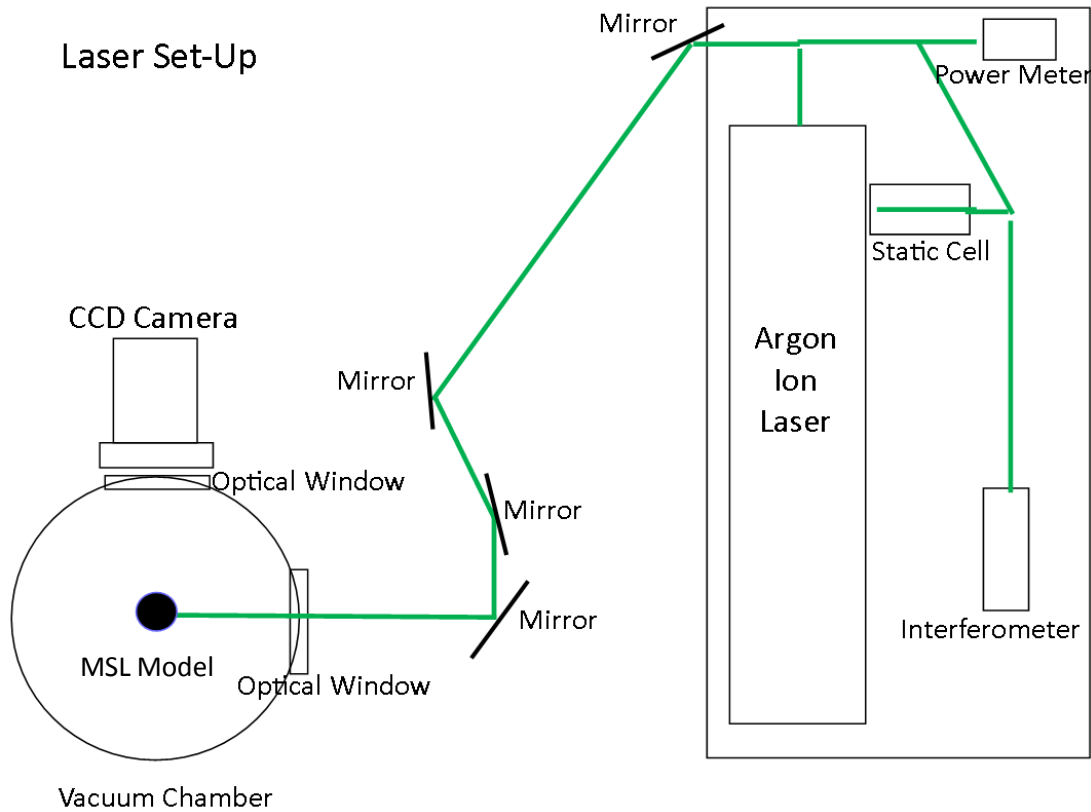
Laser Set-Up

Figure 4.3 Laser Set-Up for PLIIF Experiment. Green line marks the laser beam path.

The beam from a 514.5 nm argon ion laser is split by a beam splitter. The significant beam is reflected by four mirrors across the room over to an optic train located in front of the vacuum chamber, in line with the model and centerline of the test section, but in a plane perpendicular to the camera. This optic train contains an iris to control the diameter of the laser beam through the optics, followed by a cylindrical lens with a focal length of -400 mm to collimate the beam. The collimated beam then goes through a spherical lens with a focal length of 330 mm to focus the laser sheet on the RCS jet exit with about 0.3 mm in thickness. A thin laser sheet is desired so that the PLIIF planar image width is small compared to the RCS jet diameter.

The other portion of the beam is split further to go into an external laser Spectraphysics 404 diode power meter, a static iodine cell and a Spectraphysics 450-1 interferometer. The power meter monitors external laser power and is calibrated before each experiment using the laser's internal power meter. The static cell, as discussed earlier, is sealed to a pressure of 0.3 torr and at room temperature. The static cell fluorescence is captured by a photodiode. The interferometer reads relative frequency from the laser beam and is the primary feedback for the program that scans through the laser frequencies. All three of these measurements – power meter, photodiode and interferometer frequency – are included in the data acquisition program and information is stored in the computer. The data acquisition program will be discussed at length later in Chapter Six.

4.5 CCD Camera System

As shown in figure 4.4, the camera is located at a plane perpendicular to the optical train in order to image the flowfield plane across the laser length and height of the laser sheet.
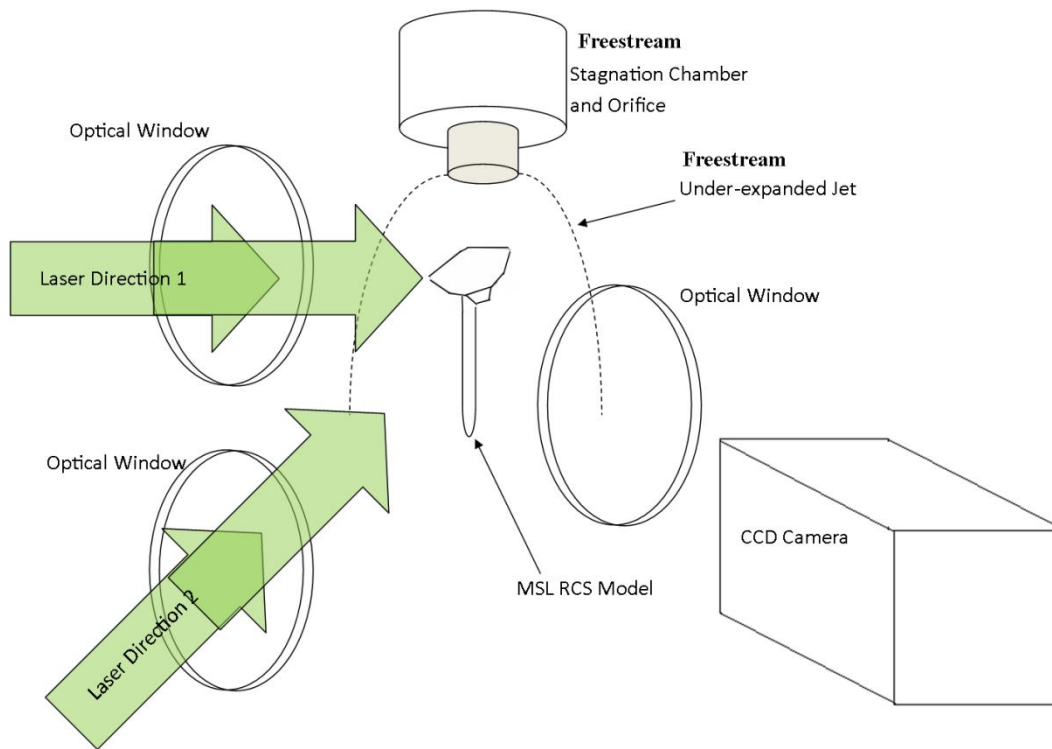
Figure 4.4 Laser and CCD Camera Schematic

directed through either the lower or the middle optical window of the low-pressure chamber. The two laser sheet directions are shown in the figure. These two laser sheet directions compose the two directions that give two components for the calculation of planar velocity, as described in the previous chapter. The two directions are not taken simultaneously but successively.

Images are taken using two different cameras. Early qualitative images were taken using a Photometrics CH 210 CCD camera with a 516x516 pixel CCD. This camera is liquid-nitrogen cooled to temperatures around -90°C in order to minimize dark current to allow

for high-quality images in spite of the long exposure times. The camera system allowed for 14 bit analog-to-digital conversion with an adjustable gain from 1 to 4 to allow for increased sensitivity. Later qualitative and quantitative images were captured using an Andor Ikon-L camera which has a thermoelectric cooled CCD. The CCD was considerably larger than for the Photometrics camera with a 1056x1056 pixel count and the system provided 16 bit analog-to digital conversion to provide greater resolution and sensitivity relative to the Photometrics camera system. Like the Photometrics camera, the Andor camera had an adjustable gain from 1 to 4 but the gain of 4 was used almost exclusively. The Andor camera system is liquid cooled using a Koolance cooler with special coolant to maintain the camera at temperatures of -90 degrees Celsius, giving the camera a low dark current. Both cameras were fitted with an 85 mm f/1.8 Nikon lens and an extension ring used to reduce the focusing distance. The cameras also used a 560 nm long pass filter in order to reduce light scatter from the laser. Images obtained through both camera systems are stored as a part of the data acquisition system. The cameras take averaged images with exposure times that can be adjusted depending on the amount of fluorescence available.

With the pumps operating and iodine-seeded nitrogen gas introduced into the main freestream flow, there is adequate signal to image the bow shock over the model MSL aeroshell. By introducing iodine-seeded nitrogen through the RCS jet in the model, the RCS jet structure is also able to be captured through the use of the CCD camera. Hence, the entire complicated interactions of the RCS jet structure with the aeroshell and the bow shock off the aeroshell can be obtained both qualitatively and quantitatively.

CHAPTER FIVE

EXPERIMENT DESIGN

5.1 Introduction

In this chapter, the approach for determining the experimental parameters for this research is outlined. This effort was necessary to allow a study of important parameters for the blunt body and RCS research. Given the current wind tunnel set-up, it was necessary to determine model size, RCS jet size, model characteristics, Mach number, as well as parameters to outline the experiment for comparison to the computed solutions completed at the University of Michigan.

One important consideration in the design of the experimental RCS models had to do with the limitation of the numerical solution in computing the full structure of the underexpanded jet that formed the freestream test section. Such a full viscous calculation, with oblique shocks embedded in shear layers, for example, would require excessive computational resources. As a result, the numerical solution treated the underexpanded jet freestream test section as an inviscid source flow, without barrel shock and Mach disk shock structures, or bounding shear layers.

The impact of this computational limitation on the experimental design was that, experimentally, the model bow shock can interact with the freestream test section barrel shock structure, especially the triple point where the oblique barrel shock and normal Mach disk intersect, as shown in figure 5.1.
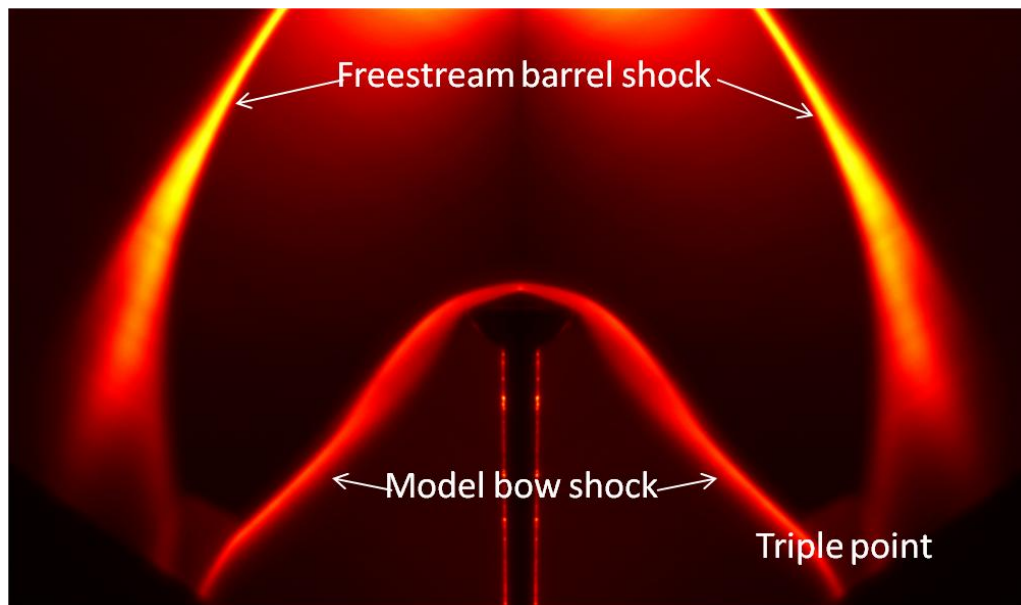
Figure 5.1 An image of MSL model at zero degrees angle of attack, highlighting the shock-shock interaction of the model bow shock and the freestream barrel shock and triple point.

This interaction can change the characteristics of the model bow shock by shock interaction. This interaction can change the shape and strength of the model bow shock. This is undesirable, since the comparison of the measured flowfield with the computed one would be less meaningful. Therefore, an early part of the experimental design was to determine the size and placement of the RCS model in the underexpanded jet test section in order to minimize this shock-shock interaction that was not computed. This required a parametric study varying the position of the model in the test section as well as size and angle of attack of the model. The resulting model characteristics were used to design RCS

models to be used in the qualitative and quantitative PLIIF studies for the remainder of this research.

The parametric study is first outlined and discussed. This chapter then outlines the model design and test conditions for the experimental setup.

5.2 Model Design

The model to be studied was a scaled version of the Mars Science Lander aeroshell, shown in the figure below. At the outset, it was determined to maintain, as much as possible, the scaled geometry of the Mars Science Lander aeroshell.
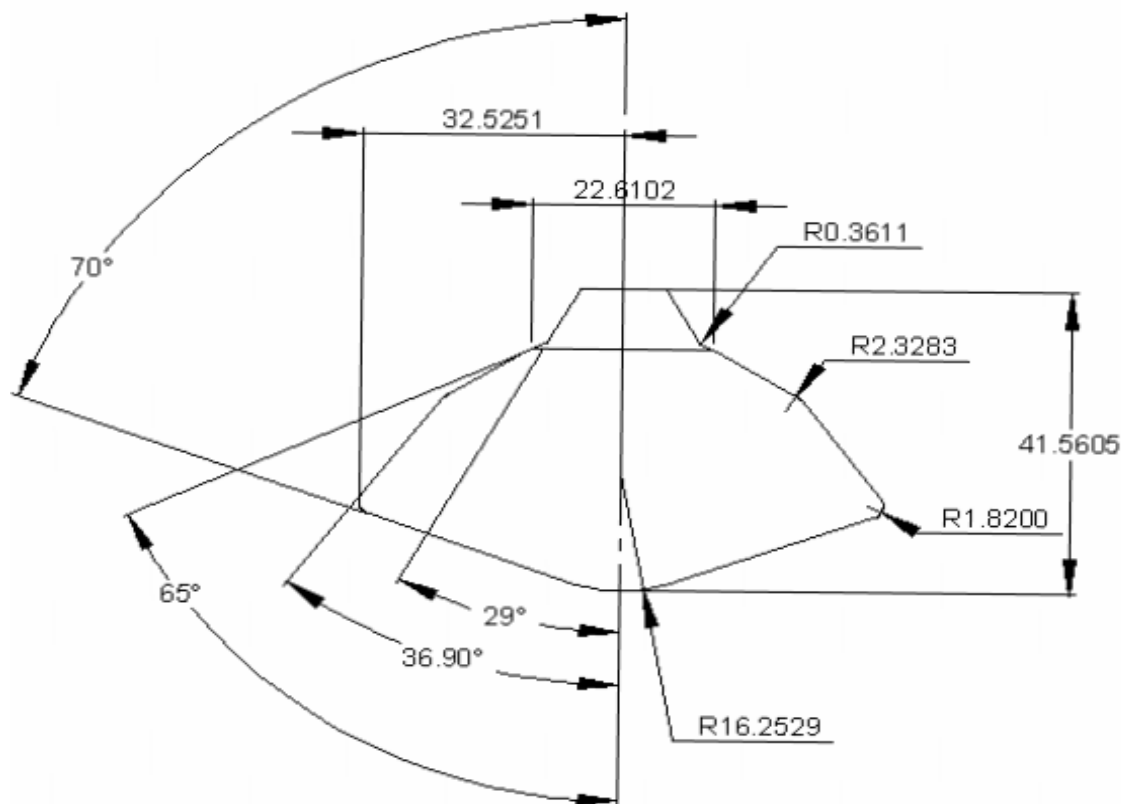
Figure 5.2 Mars Science Lander geometry, units given in inches.

The Mars Science Lander is characterized by a 70-degree spherical cone heat shield on the front of the aeroshell and an angled geometry on the backshell to accommodate the payload. The size of the model used this work was constrained by the test section size. A parametric study was used to determine the model size and location in the wind tunnel test section.

5.3 Motivation and Objectives of Parametric Study

Although several experiments had been completed using the PLIIF experimental method and hypersonic wind tunnel before, none of that work investigated blunt body aerodynamics [21, 85, 109]. Therefore it was necessary to determine the best set of parameters in regards to model size, Mach number and angle of attack that would allow proper investigation of the RCS interactions with the freestream and the aeroshell. Problems will occur if the model bow shock interacts strongly with the barrel shock and triple point (Mach stem) that forms the freestream test section. This would create undesirable shock/shock interactions that would make comparisons with the inviscid CFD solutions less meaningful. A parametric study was conducted to investigate these three parameters for the design of the experiment.

For the parametric study, a small (1.5 cm) diameter and a larger (2 cm) diameter 70-degree spherical cone model were placed on a sting in the test section at a 20-degree angle of attack and at a Mach number of 8, 10 and 12. The 20 degree angle of attack was chosen because it is the trim angle of attack for the entry of the MSL into the Mars atmosphere.

The Mach numbers for the parametric study were chosen by considering the characteristics of the underexpanded jet freestream test section. The highest Mach number possible for the wind tunnel is Mach 16; however, placing a model at this Mach number causes unacceptable interaction with the freestream Mach disk. On the other hand, placing a model at a low Mach numbers enhances the interaction of the model bow shock with the oblique barrel shock and triple point that forms the test section. For this parametric study, three Mach numbers were chosen that fall between the two extremes: Mach 8, 10 and 12 (see figure 4.2).

5.4 Parametric Study Set-Up

The two models were placed at the different locations within the test section and at an angle of attack of 20 degrees, as previously discussed. Visualizations were conducted using plasma emission technique. An Electro-Technic High Frequency tesla coil provided a high voltage and small current to ionize the air in the wind tunnel chamber and produce a glow discharge. The ionized air allowed for visualization of the model bow shock interaction with the test section barrel shock. Photographs of the glow discharge visualizations were taken using an Olympus digital camera at different exposures ranging from 1 to 8 seconds.

It is important to note that the three dimensional shock interactions illuminated by the glow discharge are captured in a two dimensional image by the digital camera. Thus, the images are not spatially resolved. Potentially, the barrel shock and the triple point that form the freestream test section will affect and influence the shape and behavior of the

model bow shock. The visualization images were examined to determine the size and Mach

number most suitable for the experiment.

5.5 Plasma Visualizations

Images for Mach 8, 10 and 12 for the smaller model set at a twenty degree angle of

attack are shown in Figures 5.3, 5.4 and 5.5.

Figure 5.3 Plasma visualization of 1.5 cm model in Mach 8 freestream at 20° attack

Figure 5.4 Plasma visualization of 1.5 cm model in Mach 10 freestream at 20° angle of of attack

Figure 5.5 Plasma visualization of 1.5 cm model in Mach 12 freestream at 20° angle of attack

For all figures 5.3-5.5, the shape of the freestream barrel shock remains unchanged. At Mach 8, there is a strong interaction of the model bow shock with the freestream triple point. This interaction is weakened when the model is moved to the Mach 10 location and is seen to disappear at Mach 12.

Images for the larger 2 cm diameter model at speeds of Mach 10 and 12 at a 20-degree angle of attack are shown in figures 5.6 and 5.7.
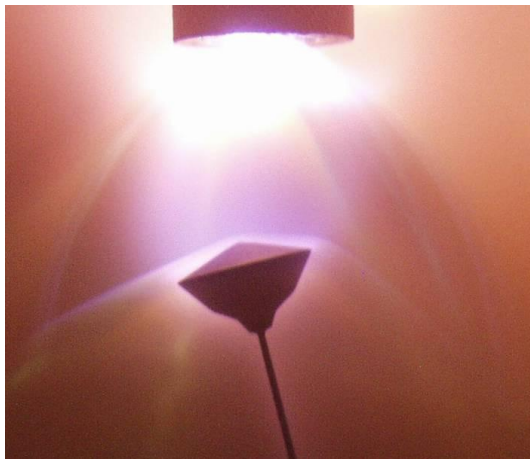
Figure 5.6: Plasma visualization of 2 cm model in Mach 10 freestream at 20 angle of attack

Figure 5.7 Plasma visualization of 2 cm model in Mach 20 freestream at 20° angle of attack

For the larger model, the shock waves exhibit the same characteristic behavior as shown with the smaller model with interaction between the model bow shock and the test section triple point. For the larger Mach number, the model bow shock curves around the model and when compared to the CFD solution (to be shown in Chapter Ten) shows negligible shock/shock interaction.

In order to better understand the RCS interactions, it is important to have the model bow shock interact with the freestream test section shock system as little as possible. In these visualizations, the bow shocks off the models (either size) show the least amount of influence from the freestream barrel shock at Mach 12. Therefore, a freestream Mach number of 12 was chosen for this research. Since the larger model will give better spatial resolution for the PLIIF imaging of RCS interaction, this larger model was selected for the experiments to examine RCS interactions.

5.6 Conclusion of Study

After examining the images obtained for two model sizes at an angle of attack of 20°, each at two or three Mach numbers, it was decided to design a model with RCS jets with a 2 cm diameter at a 20 degree angle of attack and a freestream Mach number of 12. The model would incorporate an RCS jet and would be used for qualitative and quantitative PLIIF measurements for the interactions between the RCS jet and the flowfield around the MSL model. Note that for a 2 cm diameter, the scaling compared to the actual MSL is 0.012:1.

5.7 RCS Jet Design

For the design of the RCS jet, including its location on the model, size and shape, there were many competing design constraints to consider. In discussion with the Aerothermodynamics Branch at NASA Langley, it was desirable to create two RCS jet

configurations: one configuration in which the jet issues parallel to the freestream flow and one configuration in which the jet issues perpendicular to the freestream flow [104]. These RCS jet configurations will be referred to as parallel and transverse, respectively. It was determined that these jets should have the same exit conditions and only differ in jet exit direction in order to imitate the roll/yaw and pitch RCS jets used on re-entry vehicles. In order to design the RCS jets, a list of desired characteristics was chosen:

1. There should be agreement with actual RCS jet to MSL aeroshell scaling.

2. The RCS jet size must be reasonable to manufacture.

3. The jet location would be just downstream of the second shoulder on the model.

4. The parallel and transverse jets should exit at the same angle with respect to exit surface.

5. The length and angle of the subsonic convergent section of the parallel and transverse jet internal geometries upstream the jet exit should be the same.

6. The models would have simple internal geometry that can be accurately manufactured.

7. Both jets would be sonic at the exit in order to produce underexpanded RCS jets.

Considerations three through five refer were intended to help create two jet configurations that only differed in exit direction with respect to the aeroshell and were identical in all other jet exit conditions. With a model diameter of 2 cm, the RCS exit scaling is 83 times smaller than the actual MSL. To perfectly match that scaling for the RCS jet would result in an RCS model jet diameter on the order of 0.01 mm, which is too small for the machinist to manufacture. It was decided to use an RCS jet exit diameter of 0.5 mm.

The designs of the two MSL/RCS configurations are shown in figures 5.8 and 5.9. The design allowed for the two jets to exit at the same location on the aeroshell with similar exit geometries and conditions. The jet exits were elliptical in shape, with a minor axis of 0.5 mm. A subsonic convergent cone angle of 15 degrees was used. Figure 5.8 shows the internal geometry and figure 5.9 shows the exterior of the model. The machinist drawings and specifications are included in Appendix B.
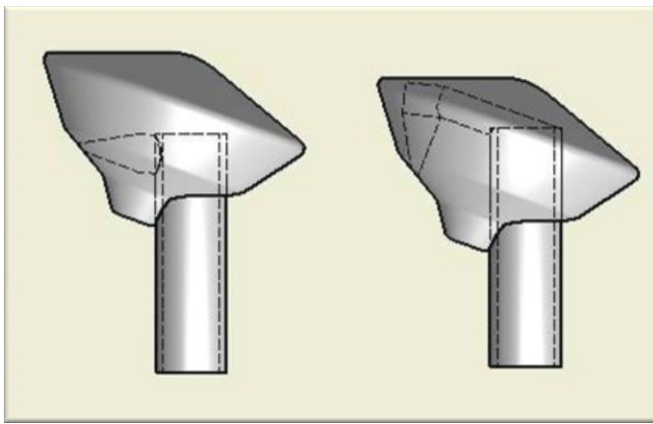
Figure 5.8 Interior geometry for transverse (left) and parallel (right) configurations
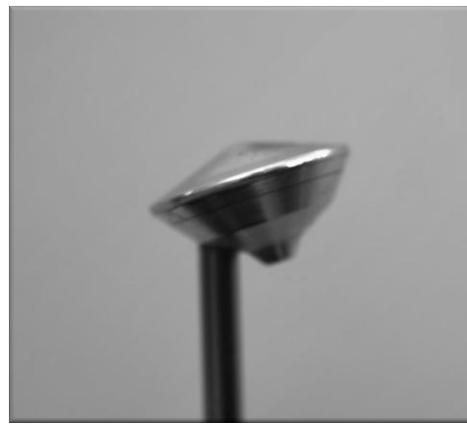
Figure 5.9 Photograph of model exterior

This model and jet design were chosen for subsequent investigation of the RCS jets and their interactions with the aeroshell bow shock and freestream flow.

5.8 Test Conditions

When examining the interactions between the RCS jet, the aeroshell bow shock and the freestream, it is desirable to design the test conditions for comparison to computational simulations, as well as other previous experimental work. In the 1960's and 1970's, when work in jets from flat plates and other geometries was first investigated, experimentalists

used a dimensionless thrust coefficient to characterize the jets [67-69]. The thrust coefficient (C_T) is defined as the ratio of the thrust from the jet to the dynamic pressure of the freestream multiplied by the model frontal area. This is given in Equation 5.1 below in which T is the RCS jet thrust, q_∞ is the dynamic pressure of the incoming or freestream flow and S is the frontal area of the model [68].

$$C_T = \frac{T}{q_\infty S} \qquad (5.1)$$

This equation accounts for varying jet exit conditions as well as variation in model size and freestream conditions.

The jet thrust is defined by the rocket thrust equation as:

$$T = \dot{m}V_j + (p_j - p_\infty)A_j \qquad (5.2)$$

in which $\dot{m}$ is the jet mass flow rate, V_j is the jet exit velocity, p_j is the jet exit static pressure, p_∞ is the static pressure of the freestream ahead of the model bow shock (i.e. M_∞ =12), and A_j indicates the area of the jet exit. The first term in equation 5.2 is:

$$\dot{m}V_j = \rho_j A_j V_j^2 = 2q_j A_j \qquad (5.3)$$

in which ρ_j is density at the jet exit and q_j is the exit dynamic pressure. This leads to the following simplified equation:

$$T = A_j(2q_j + p_j - p_\infty). \qquad (5.3)$$

This thrust equation has three terms: the dynamic pressure of the RCS jet, the exit pressure of the RCS jet and the ambient pressure of the freestream. The first term is the positive thrust resulting from the mass flow rate. The second two terms are the difference between the jet exit pressure and the back pressure. (This third term is negligible as will be seen in the formulation given below). In order to use this thrust coefficient in a meaningful way for the experiment, it was necessary to determine if there was a way to reduce the number of variables to a few that could be easily changed or modified to give different thrust coefficients.

Assuming isentropic flow, the thrust coefficient becomes:

$$C_T = \left(\frac{A_j}{S}\right)\frac{2}{M_\infty^2 \gamma}\left[1 + \left[1 + M_j^2 \gamma\right]\left(\frac{p_{0,j}}{p_{0,\infty}}\right)\left[\frac{1+\frac{1}{2}(\gamma-1)M_\infty^2}{1+\frac{1}{2}(\gamma-1)M_j^2}\right]^{\gamma/\gamma-1}\right] \qquad (5.4)$$

Given that the exit Mach number of the jet for the experimental set up is 1 (the jet is sonic) and the freestream Mach number is 12, and the gas used was nitrogen with a gamma of 1.4, the terms in equation 5.4 can be reduced for supersonic Mach numbers to a constant times a ratio of RCS jet stagnation pressure, $p_{0,j}$, to freestream stagnation pressure, $p_{0,\infty}$, shown in equation 5.5.

$$C_T = 1.14\left(\frac{p_{0,j}}{p_{0,\infty}}\right) \qquad (5.5)$$

For the actual thrust coefficients, it was decided to follow thrust coefficients used in the previous research [67-69, 105-106] and investigate values from zero to three in increments of 0.5. These thrust coefficients are actually higher than those that would be used on the Mars Science Lander for a given RCS firing, with actual thrust coefficients

generally around 0.01. However, in order to have large enough RCS jets for adequate resolution of the jet geometry for the two configurations and to compare to computational models, zero to three was chosen as an adequate coefficient range to study. For the quantitative work, a thrust coefficient of one was chosen.

The experiment is operated with a freestream stagnation pressure of 1.8 atm (183 kPa) which results in a stagnation pressure range for the RCS jet from 11 to 70 psia (80.7 to 482.6 kPa) for C_T of 0.5 to 3.0, as shown in table 5.1. This is a reasonable range for the pressure gage to read accurately and also a safe range for the pressure rating of the tubing lines used to introduce iodine-seeded nitrogen through the model into the test section.

Table 5.1: Required Pressures for Selected Thrust Coefficients

Thrust Coefficient	Total RCS Jet Pressure psia (kPa)
0.5	11.7 (80.7)
1.0	23.3 (160.5)
1.5	35.0 (241.3)
2.0	46.7 (322.0)
2.5	58.3 (402.0)
3.0	70.0 (482.6)

It must be noted here that, given the constant that was derived in equation 5.5 for Mach 12, the choice of a Mach 12 freestream is a good one. Given the freestream stagnation pressure of 1.8 atm for the experiment, a Mach 10 freestream would require higher pressures for the RCS jet and even higher than that for Mach 8. This would be out of the range of the pressure gauge and safety considerations.

The parametric study showed that a freestream Mach number of 12 not only minimized experimental test-section interference but also utilized a good range of pressures that was compatible with the experimental apparatus.

The conditions for this experiment can be summarized in the table below:

Table 5.2: Test Conditions for RCS Experimental Setup

Dimensionless Parameter	Value
Freestream Mach number	12
Mach number at RCS jet exit	1
Thrust coefficients	0.5, 1.0, 1.5, 2.0, 2.5, 3.0

CHAPTER SIX

DATA ACQUISITION AND ANALYSIS

6.1 Introduction

Given the explanation of the theory of the Planar Laser-induced Iodine Fluorescence in Chapter Three, the explanation of the experimental facilities in Chapter Four, and the design and set-up of the experiment itself in Chapter Five, it is necessary to give a detailed description of the data acquisition and analysis used. Unlike the previous sections which focused in large part on theory, scope and capabilities of the technique and method, this section will focus largely on the procedures and methods used to accomplish the body of work. Data acquisition will be briefly discussed regarding how information is obtained, recorded and utilized to complete the objectives for this research and extract the desired information. A list of procedures to run the experiment will also be described, denoting differences for qualitative and quantitative data methods. The chapter will end with a discussion on data analysis for both qualitative and quantitative methods. This chapter can be seen largely as a "nuts and bolts" chapter, intended so that the reader may understand the actual logistics for the technique and experiment.

6.2 Data Acquisition

It was stated before that the technique and experiment require the coordination of several different systems all working in concert in order to perform a successful experiment. A significant part of this coordination is handled by the data acquisition system and the Labview program that executes it.

For the qualitative data collection, the etalon in the laser which selects longitudinal laser modes, was removed from the laser. In this manner, the laser could be operated in broadband mode, in which the laser linewidth is much greater than the iodine absorption linewidth. Because of this, the laser excited several iodine transitions at once. Such a set-up does not require frequency monitoring, making the acquisition simple enough to perform without an extended computer-controlled data acquisition program. In fact, because of its ease of execution, most of it was performed manually with the exception that of a canned program, which was used to maintain temperature control on the CCD camera and also to take images. The canned program, called Andor Solis, asked for user inputs for camera gain and exposure times in order to obtain the qualitative images. Other data that was necessary to obtain and record for this portion of the research, was the back pressure in the vacuum chamber, the RCS jet total pressure of the model and the freestream main jet pressure in the stagnation chamber before the main jet orifice. The back pressure was important for determining the location of the Mach disk for the main jet, which thus directly impacted the size of the freestream test section for the experiment. This was recorded for repeatability purposes and to maintain similarity between different runs of the experiment. The RCS jet stagnation pressure and the main jet stagnation pressures

66

were recorded manually and were important to determine the RCS jet thrust coefficients. The RCS jet stagnation pressure and the main jet stagnation pressure were maintained by manually monitoring the pressure displays and using a needle valve to control the flow rate. RCS jet pressure for the qualitative portion of the body of research was observed and recorded from a Hess analog gage with a resolution of 0.05 psia and a range of 0-100 psia. The main jet pressure was observed and recorded from a Setra digital gage with a resolution of 0.005 psia and a range of 0-100 psia with an accuracy of 1% FSR. Images were taken as stated before using the Andor Solis program which also saved the images and displayed them.

To obtain quantitative data, the laser is operated in narrowband mode, in which the laser linewidth is narrower than the iodine transition linewidth. The laser is stepped through small frequency step sizes through the use of a stepper motor and piezo-electric transducer in order to obtain an absorption spectrum for each point in the flowfield. This method necessarily requires the use of an automated computer program to orchestrate the several functions required to obtain the data. Using Labview as the data acquisition program, the program had a number of different and concurrent uses: controlling camera temperature; capturing images from the Andor camera and storing and displaying them; measuring and recording pressure data; measuring and recording temperature data from 9 thermocouples located in the pumps, vacuum chamber, room, and cooling pit; and monitoring, recording and controlling the frequency of the laser through the interferometer, piezo-electric transducer and the stepper motor attached to the etalon of the laser; and measuring and recording fluorescence signal on the static cell. This can be

summarized in the following figure, 6.1, in which the Labview program oversees and controls three systems for data acquisition.
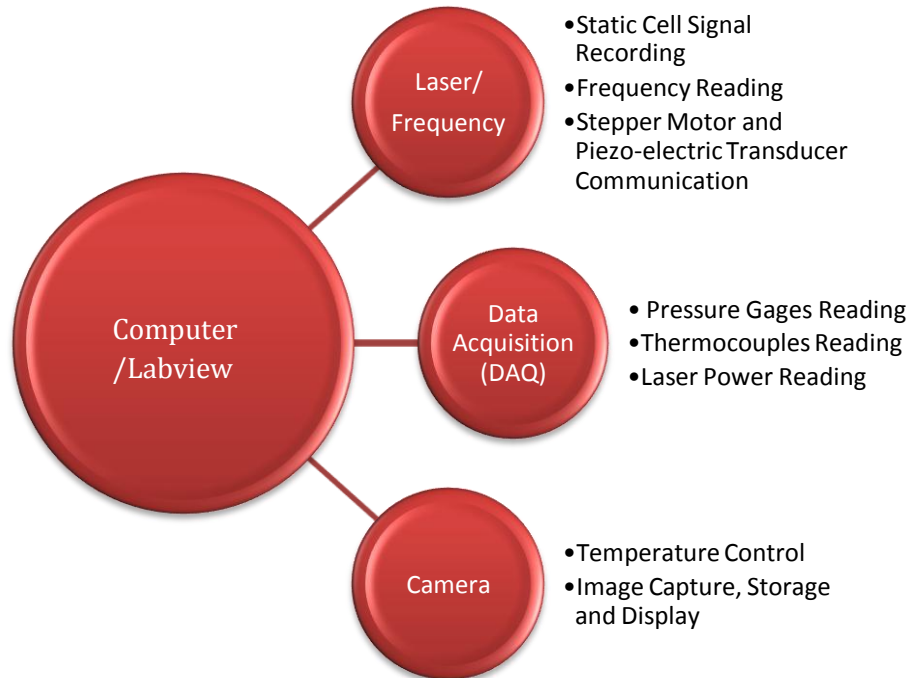
Figure 6.1 Basic diagram outlining the processes and measurements controlled by the Labview data acquisition program for quantitative experiments

For the camera control portion of the program, active camera temperature control runs in parallel to all other programs throughout various functions in order to maintain low shot noise for good images. The program also allows for users to input desired camera gain and exposure times, in addition to controls for capturing, saving and displaying images. The image display also allows the user to adjust the viewing region and signal levels in order to examine the quality of images during an experiment run.

The computer also automatically measures and records data from various instruments throughout the lab. The pressure data from the RCS jet total pressure, the freestream main jet pressure in the stagnation chamber and the back pressure are

recorded at every frequency step in the experiment. Secondly, temperature is measured and recorded from the thermocouples located in the three vacuum pumps, the low pressure chamber, the RCS pressure line, the room, and the water cooling pit. Thermocouples in these places are necessary in order to monitor the performance of the experiment. The chamber stagnation temperatures are used to calculate predicted temperatures for isentropic expansion in the flow. The thermocouples in the pumps and in the room are used to monitor the operation of the equipment to avoid overheating the pumps during the long experiment times. Laser power is also monitored. If the laser power drops below a certain level, which it experiences at the edges of the laser gain profile, the program will stop running in order to avoid an over-current on the laser.

The frequency reading and control is, by far, the most complicated portion of this data acquisition program system and could not be completed without the use of the program. The feedback loop for this process is shown in the figure 6.2:
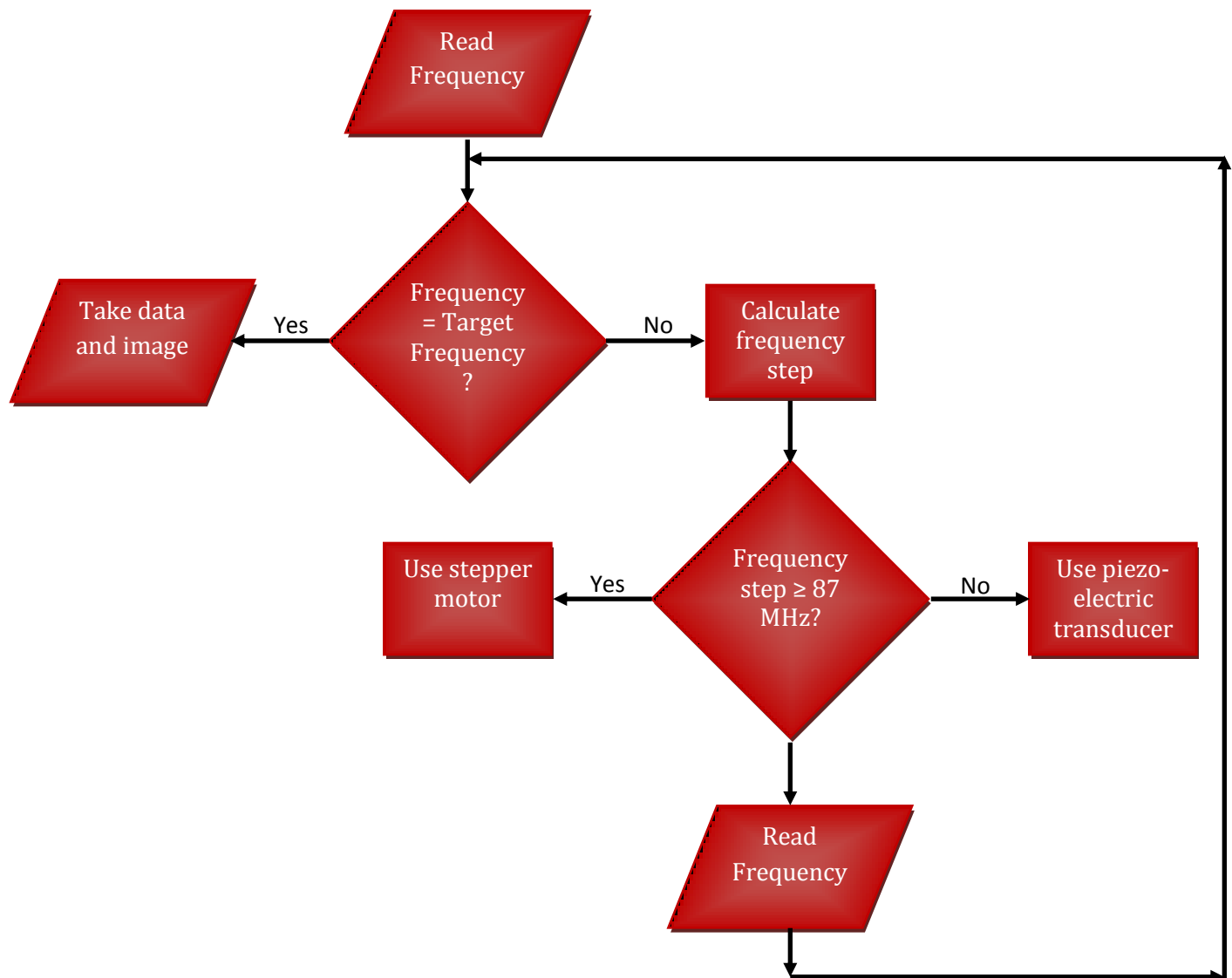
Figure 6.2 Flowchart for Frequency Feedback and Control

As shown in Figure 6.2, feedback consists of determining from the computer (or user) what the desired frequency should be and calculating the required frequency increment. If the desired frequency change will be greater than or equal to a laser longitudinal mode hop (87 MHz), the stepper motor is directed to move the gear on the etalon a calculated number of turns. If the desired frequency change is less than a mode hop, the piezo-electric transducer receives an electric voltage signal that lengthens or

shortens the cavity length of the laser to effectively create the given frequency change. The interferometer is probed again and the process is repeated until the frequency is within 5 MHz of the desired frequency. In this process, the interferometer and the piezo-electric transducer both communicate with the computer through a National Instruments voltage data acquisition card while the stepper motor communicates through means of GPIB. In addition to laser frequency, the laser power was monitored and recorded at each frequency point in order to account for a power decrease on the outer edges of the laser profile. The Labview program which controlled and recorded all of this information is an updated version from a previous version to account for upgrade in camera, data acquisition and computer hardware [85]. In addition to upgrading the program, there was an addition made to control cooling of the CCD camera from the program. In the Labview program, the user has the ability to choose which functions to perform and the program saves the appropriate information as SIF images (Andor-specific file format) or in a spreadsheet. When running a full scan through the laser profile, the data acquisition program performs the following functions in order: uses the stepper motor and the piezo-electric transducer in concert to move specified step in frequency; records frequency, laser power, static cell signal, pressures, temperatures; and takes a picture and displays it.

6.3 Data Collection Procedure

The following steps are taken to run the experiment. A more detailed procedure is given in Appendix C.

(1) Turn on the equipment: laser, etalon heater, vacuum pumps and instrumentation.

(2) Adjust the optics to allow for proper alignment on the model.

(3) Open up the Labview program and set up desired variables for the run.

(4) Introduce nitrogen into the mixing chamber to seed iodine.

(5) Introduce iodine-seeded nitrogen into the vacuum chamber and through the model and adjust flow rates to achieve desired thrust coefficient.

(6) Tune laser across laser profile using Labview program. At each frequency step, an image is taken with the CCD camera and temperature, pressure, static cell signal and laser power are measured.

(7) During the laser scan, monitor and adjust (if necessary) jet pressures, laser sheet position.

(8) Once a scan is completed, background images with the laser sheet in place but the flow turned off are taken.

(9) Shut the system down.

From start-up of the laser to shut-down, experiment times vary between eight and fourteen hours. Variation in run times is due largely to exposure times for the hundreds of images taken, as well as performance of the laser.

6.4 Qualitative Data Analysis

Since the qualitative experiments are merely capturing images, data analysis consists in little more than examining the various images taken to find one that has a good signal-to-noise ratio without over-saturation of the fluorescence. These SIF images are converted to a useable data format (usually a jpg or tiff image) and the image is

superimposed with a picture of the model in the wind tunnel with no flow on at normal room lighting. This superimposed model helps orient the viewer for the flow phenomena that are seen in the images. As a part of the qualitative image data analysis, in order to make a semi-quantitative comparison between the CFD and the PLIIF data, the signal level at location along the centerline of the RCS jet is taken and recorded. At conditions of low pressures and temperatures, or within a few jet exit lengths from the RCS jet exit, the fluorescence signal has direct correlation to density. This can then be compared to density predictions made using CFD calculations.

6.5 Quantitative Data Analysis

During the quantitative experiment procedure, as the laser frequency is scanned, fluorescence signal is collected at each pixel on the CCD camera by taking an image of the flow. From the resulting series of images, the iodine absorption spectra are generated for every point in the flowfield. Data analysis for the quantitative experiments, therefore, is necessarily more complicated and involved. Once the data is all collected, the static cell signal measured is plotted versus the relative frequency of the experiment to get an initial estimate on the effectiveness of the run. Images that were taken at each frequency of the laser scan are converted into data files and a small region of interest of pixel locations is selected and these images are then compiled into iodine spectra and saved as jpg data images. These images are reviewed to look for potentially bad regions of data (such as if a door was opened during an experiment, resulting in an image with significant amounts of

outside light) and also to examine the spectra to make sure there is sufficient frequency step resolution to analyze the spectra.

Once the run is deemed satisfactory, a region of interest from the flowfield that includes the RCS jet and the model bow shock is chosen for analysis. Using a compilation program written in Matlab, the images are listed and organized and a 3D matrix is created which holds the spectral data at each pixel (location in the flow) for all of the images. (The 3 dimensions come from a 2D CCD, with the third direction being the resulting absorption spectra for each X, Y pair.) The static cell data is extracted from the spreadsheet and normalized. The frequency data is also extracted from the spreadsheet of collected data. This frequency data, which is relative frequency, is adjusted so that the P13/R15 peak on the static cell signal aligns closely with the relative frequency peak in the iodine fluorescence model (around 2 GHz). This step merely allows for the program to better align the correct peaks during the analysis process.

At this point, all of the data is properly compiled and organized for analysis of every pixel in the region of interest. However, doing so with one program would take significant amounts of computer time and might result in running out of memory before execution is completed. Instead, a new system has been developed in which the region of interest is sub-divided into a smaller area that is called a batch. Batch sizes can include anywhere from a few hundred to a few thousand pixels and the number of batches for a given region range from 220 to 420. These batches are run simultaneously on the UVA cluster system.

The data analysis program itself utilizes the iodine spectral model (equation 3.2) that has been compiled from spectral lines near the regions of interest and also includes

hyperfine structure. This iodine spectral model is a database of information that builds the absorption spectra for any given parameters of frequency shift (related to velocity), pressure and temperature, as well as a scaling multiplicative constant and an additive constant. The data analysis program uses a global least squares fitting routine to change these parameters in order to obtain a best fit of the data to the iodine spectral model. With each parameter, the complexity of solving is increased. Hence, in order to reduce this complexity, a few things are done. First, all of the images used to compile the spectra data are background subtracted. This reduces the additive parameter to a negligible or near negligible value. Secondly, in order to eliminate the multiplicative constant, both the compiled spectra and the iodine spectra are normalized so that the peak values of the spectra to be compared have a maximum value of 1 and then have 1:1 scaling. These two steps reduce the fitting routine to solve for the three essential parameters: frequency shift, pressure and temperature, resulting in the important data. The program then runs as follows:

(1) The static cell is fitted to the iodine spectral model to get a frequency shift.

(2) The spectra from a given pixel is fitted to the data to get a pressure, frequency shift and temperature

(3) The frequency shift of the pixel spectra is subtracted from the frequency shift of the static cell to get a total frequency shift that compares the static cell to the flow data which allows for the solving of velocity.

(4) The values are all saved in appropriate matrices.

The fitting routine program runs several batches simultaneously on the UVA cluster system. Run times for a single batch can take on the order of 5 to 6 hours and increasingly more than that for areas with significantly less signal to noise ratios.

After all of the batches are run, the data from the several batches is recompiled into one coherent set of data. Once this is done, the frequency shift data is adjusted using the pressure and temperature data in order to calculate and account for frequency shift due to impact shift. The adjusted frequency shift matrix is multiplied by the laser wavelength (514.4 nm) in order to obtain velocity. A velocity matrix is obtained for each laser angle direction. The velocity directions are then transformed into x and y coordinates using a Matlab program. Once the two directions of velocity are resolved, streamlines and magnitudes may be plotted. The velocity data may be compared to prediction from the study by Ashkenas and Sherman [103] of highly underexpanded jets, using the distance from the jet exit to calculate the Mach number at that location and then using isentropic relations to obtain other thermodynamic properties required to calculate velocity.

Pressure and temperature, which were previously calculated, may also be plotted and examined. These may also be compared to predictions made by using Ashkenas and Sherman's study [103] to determine Mach number at a given location in the RCS flowfield and then using isentropic relations to calculate pressure and temperature. The isentropic equations to solve for pressure and temperature are given in equations 6.2 and 6.3, respectively:

$$\frac{p}{p_t} = \left(1 + \frac{\gamma - 1}{2} M^2\right)^{-\gamma/(\gamma+1)} \tag{6.3}$$

$$\frac{T}{T_t} = \left(1 + \frac{\gamma-1}{2}M^2\right)^{-1} \qquad (6.4)$$

in which M is the Mach number, γ is 1.4 for nitrogen, and p_t and T_t stand for total pressure

and total temperature.

CHAPTER SEVEN

QUALITATIVE IMAGES

7.1 Introduction

In this chapter, the qualitative PLIIF images obtained with the laser operating in broadband mode are presented and discussed. The qualitative data was obtained using two different types of cameras (discussed previously in Chapter Four). The results from the lower resolution camera will be limited to only a few cases for each configuration with the rest of the images given in Appendix D. Overall, the higher resolution camera gave much more detailed results and so the majority of the chapter will include a discussion of the shock structure and interactions observed from these results. The reasons for this increase in definition is due to a larger CCD on the camera creating better spatial resolution given the same camera optical setup, as well as a higher bit camera which results in a greater dynamic range to utilize for images.

7.2 Orientation of Images

Before the images and results are discussed, it is necessary to first orient the reader regarding the model placement and setup. In each image, figures 7.1 through 7.4, an image of the model (which has been superimposed on the images for the sake of understanding the image) is shown at the left of the image, oriented at an angle of attack of 20 degrees.

The mounting sting extends below the model. The freestream flows from the top of the image towards the bottom with the bow shock off the aeroshell (model) forming on the windward side of the model, or right-hand side of the image. This model bow shock is not seen in the lower dynamic range images of the Photometric camera, but is with the Andor camera images. The RCS jet exits the model just downstream of the shoulder on the windward side and flows parallel or perpendicular to the freestream, as indicated by the parallel or transverse configurations, respectively.

7.3 Photometric Camera Images

In figures 7.1 and 7.2, the images for the transverse and parallel jet configurations at thrust coefficient values of 0.5 and 1.0 are shown.
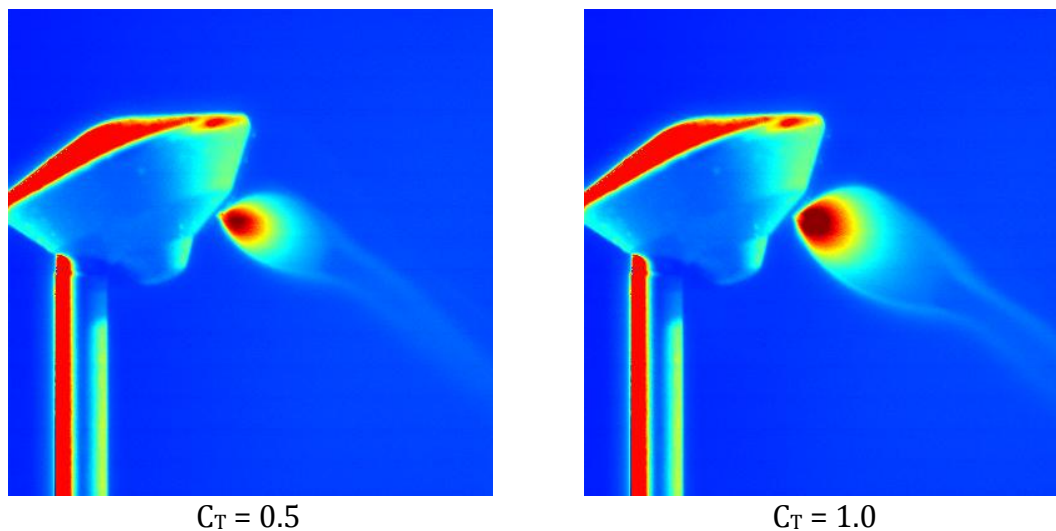

| $C_T = 0.5$ | $C_T = 1.0$ |

Figure 7.1: Transverse RCS Jet Images with Photometric Camera

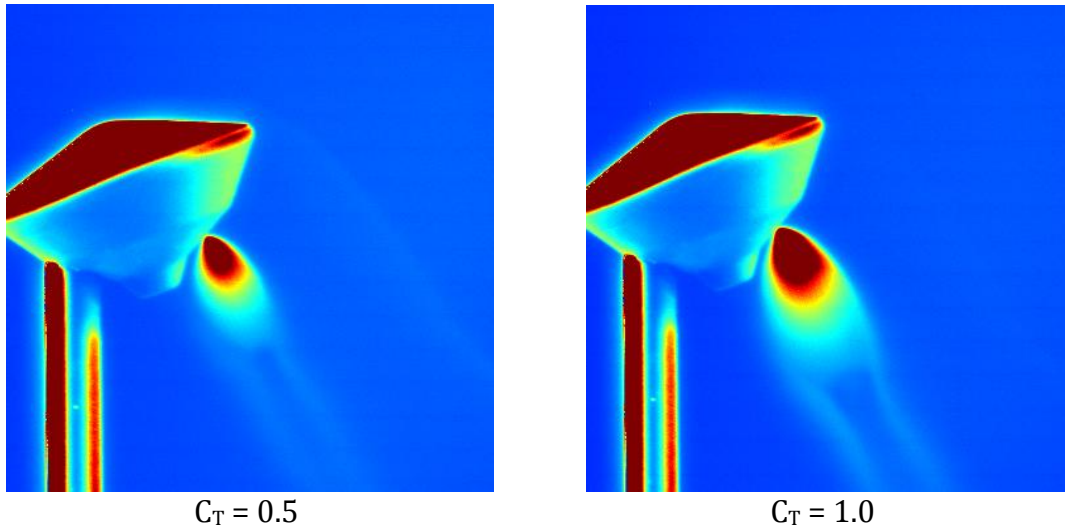| $C_T = 0.5$ | $C_T = 1.0$ |

Figure 7.2: Parallel RCS Jet Images with Photometric Camera

As can be seen in each image, the RCS jets exit the model as under-expanded jets. The shock structure around the RCS jet and its subsequent termination in a Mach disk can clearly be seen in each image. With an increase in thrust coefficient, the jet and its shock structure extends further beyond the model. For the transverse RCS jet flow, the asymmetry of the RCS jet core shock structure (most noticeable by the different shapes of the shock on the left side of the RCS jet from the right side of the RCS jet) can be seen and becomes more pronounced at higher thrust coefficients. This asymmetry is due to the interaction of the model bow shock with the shock structure of the RCS jet. The parallel jet images do not show this asymmetry since the jet does not interact with the model bow shock. As seen in these images, the dynamic range of the images is limited due to saturation in this jet core. The 12-bit higher resolution camera will give greater detail to the structure within the camera without saturating the RCS jet core.
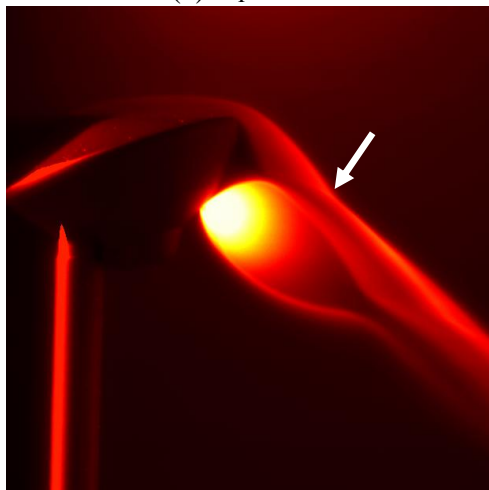
7.4 Andor Ikon Camera Images

Images shown in Figures 7.3 and 7.4 are those taken with the Andor Ikon camera, at nozzle-thrust coefficients increasing from a value of 0.5 to 3.0 in increments of 0.5. Like the images taken with the Photometric camera, the RCS jets, upon exiting the model at Mach 1, form a highly underexpanded jets with a well-defined barrel shock structure. This jet increases in Mach number reaching supersonic and hypersonic conditions before reaching a Mach disk. At higher thrust coefficients, this jet and its shock structure extend further beyond the model. However, it is readily apparent that the detail in the images is greater with this camera. The aeroshell bow shock is visible with clearly defined boundaries and a mixing region between the transverse jet and the aeroshell bow shock can be seen.
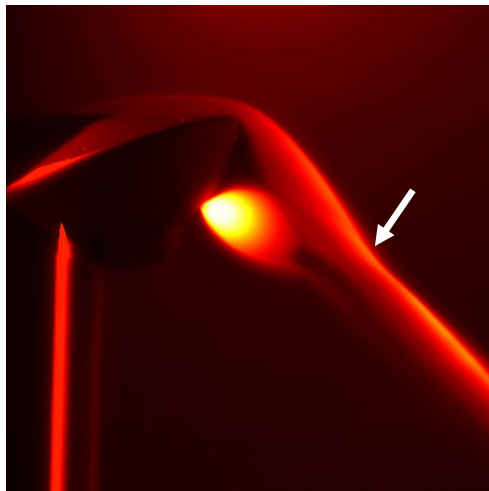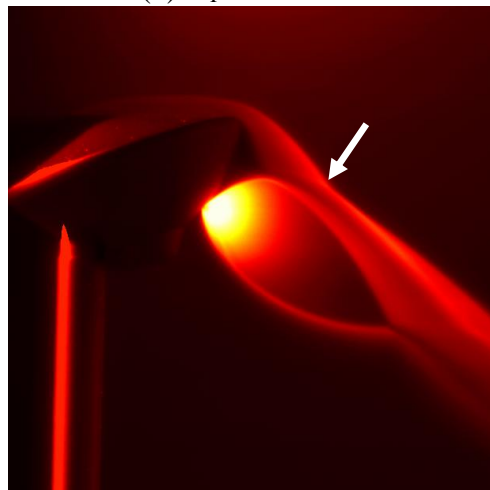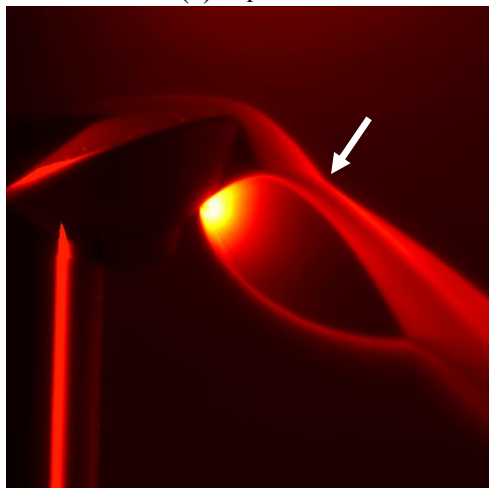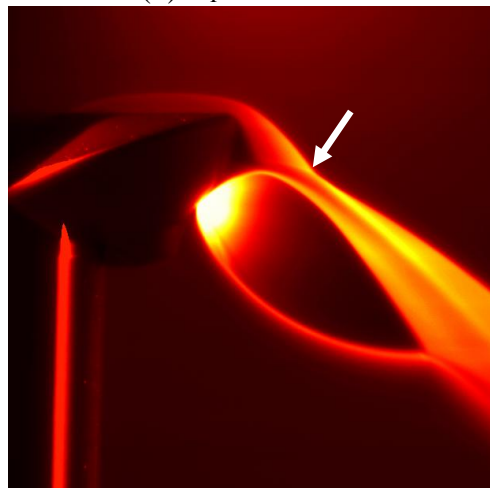
(a) $C_T = 0.5$
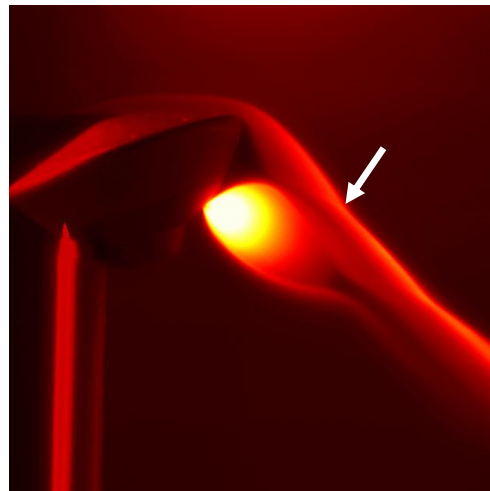
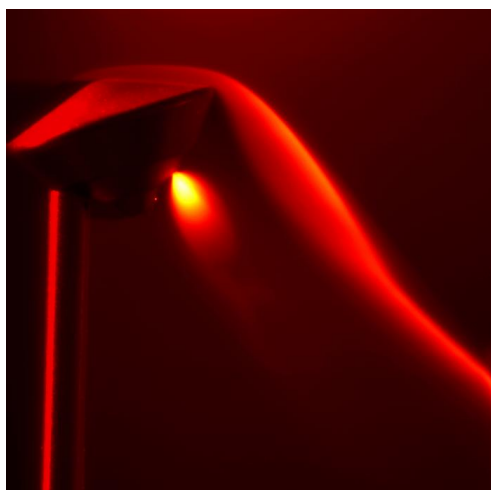(b) $C_T = 1.0$

(c) $C_T = 1.5$

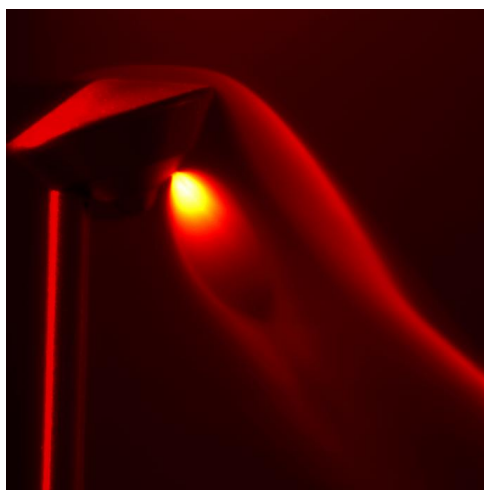(d) $C_T = 2.0$

(e) $C_T = 2.5$

(f) $C_T = 3.0$

Figure 7.3 – RCS Transverse Jet Images with Andor Ikon Camera. The white arrows indicate location of an inflection point in the bow shock.

In Figure 7.3, there are number of characteristics in the RCS transverse jet flow that become apparent. The first is the interaction of the aeroshell bow shock and the RCS jet barrel shock. This interaction can best be illustrated by the shape of the bow shock. As the jet-thrust coefficient increases, the thrust from the RCS jet pushes the aeroshell bow shock out away from the model and the RCS jet structure. This can be seen most readily in a change of angle of the bow shock as it continues downstream, indicated in the images by a white arrow. With increasing jet-thrust coefficient, this angle (arrow) moves farther upstream and closer to the shoulder. (It can be supposed that this interaction – the transverse RCS jet pushing the bow shock away from the model – would affect the surface conditions on the model, including pressure distribution and forces and moments. Such a difference of pressures and forces could induce inverse moments on the aeroshell.) Another characteristic of the transverse jet seen in these images is that with increased thrust coefficient, the jet's Mach disk reduces in diameter until the oblique barrel shocks merge. Also, there is asymmetry in the RCS jet which exists at smaller thrust coefficients but is readily noticeable at higher thrust coefficient. This seems to be due to the interaction with the bow shock from the aeroshell. At higher jet-thrust coefficients, the aeroshell bow shock is pushed upstream and curves more tightly around the model. In the $C_T = 0.5$ case, behind the shoulder is a relatively dark spot indicating a low density region; however, the $C_T = 3.0$ case indicates a smaller dark and hence, low density, area.
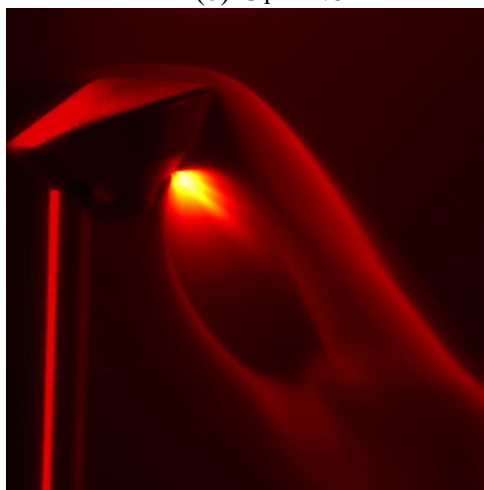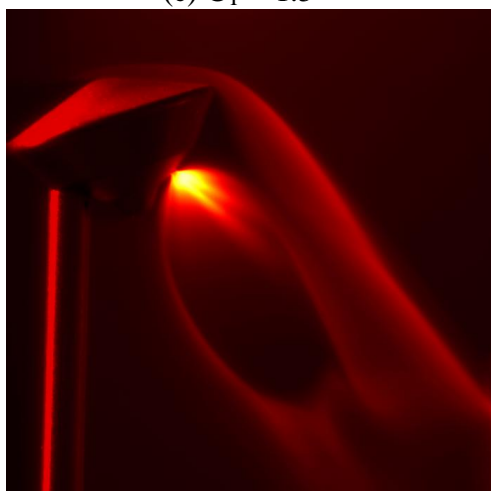
(a) $C_T = 0.5$

(b) $C_T = 1.0$
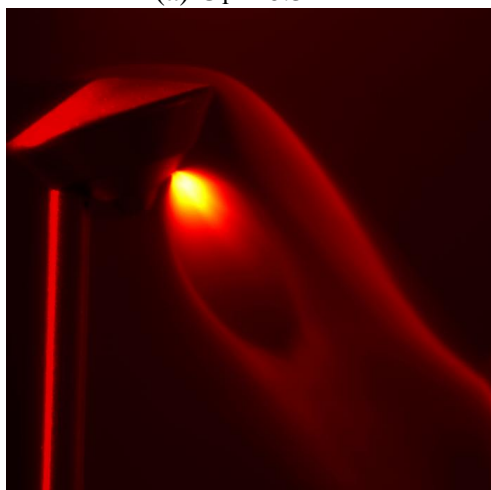
(c) $C_T = 1.5$

(d) $C_T = 2.0$

(d) $C_T = 2.5$
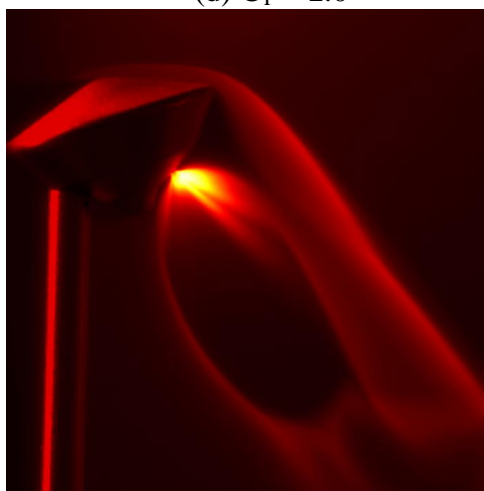
(f) $C_T = 3.0$

Figure 7.4 – RCS Parallel Jet Images with Andor Ikon Camera

The parallel RCS jet images are given in Figure 7.4. At thrust coefficients of 0.5 and 1.0, the parallel RCS jet appears to extend into a symmetric underexpanded jet structure. At thrust coefficients higher than this, an asymmetry appears and the side of the RCS jet that is closest to the aeroshell bow shock appears to be pulled into the shear mixing layer between the bow shock and the RCS jet as the RCS barrel grows in width. The shock structure for the higher C_T jet is more clearly defined, including a pronounced Mach disk. It is interesting to note that the Mach disk that terminates the RCS jet is not more than one or two RCS jet diameters wide at the lowest thrust coefficients but becomes at least 20 jet diameters (an order of magnitude) wider at higher thrust coefficients. In comparing the bow shock shape throughout the series, the parallel RCS jet appears to have no affect on the bow shock off the aeroshell. Thus, is seems unlikely that the RCS jet/bow shock interaction would affect the conditions on the surface of the aeroshell. However, the RCS jet itself could cause some local changes in pressure on the surface of the aeroshell itself, which are uncertain without surface pressures to compare. A shear region that forms between the jet and bow shock, which effectively changes the shape of the underexpanded jet structure exiting the RCS nozzle, does not seem to cause any change in shape in the bow shock structure.

CHAPTER EIGHT

TRANSVERSE JET QUANTITATIVE RESULTS

8.1 Introduction

In this chapter, quantitative results for the RCS transverse jet configuration with a thrust coefficient of 1.0 are presented. These results were analyzed using an analysis program on UVA's cluster (as described in previous chapters). Velocity and temperature fields are given and discussed at length. The results are also compared to predictions from the Ashkenas and Sherman characterization for underexpanded jets [103]. From the velocity and temperature fields, it is also possible to calculate Mach number distribution within the flow, which is given and discussed as well.

8.2 Velocity

The planar velocity vectors for the transverse RCS jet at a thrust coefficient of one are shown in figure 8.1. For clarity, the vectors are shown at every tenth pixel, rather than at every pixel. Magnitudes, superimposed with flow streamlines, are shown in figure 8.2.

In both of these images, the Mach 12 freestream flow is from top to bottom, parallel to the sides of the figure. The MSL model is shown blocked out in the top left hand corner of each figure. The top (upstream) discontinuity of the model surface is referred to as the model shoulder.
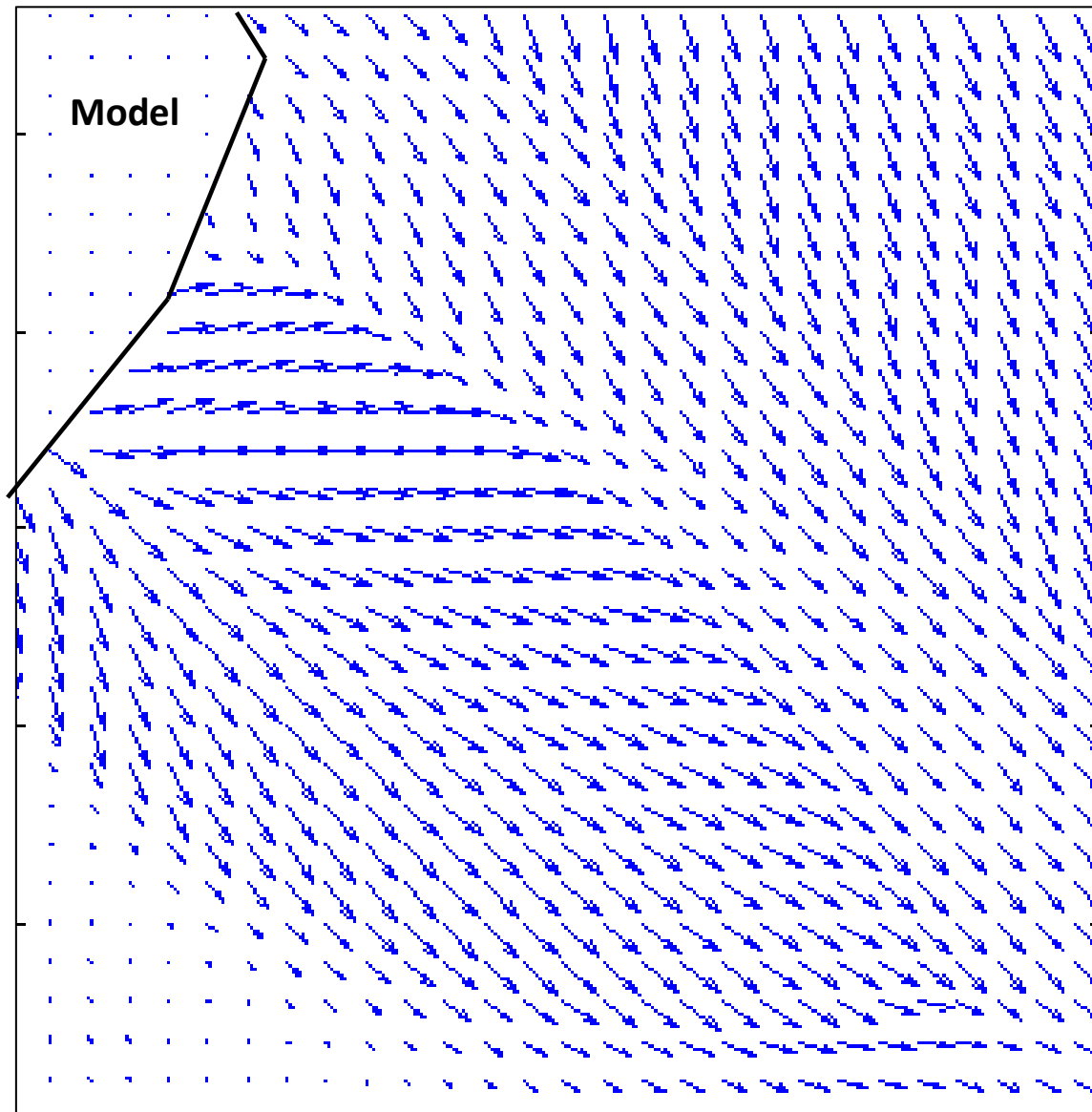
Figure 8.1: Planar velocity vector plot for RCS transverse jet with M_∞=12 and a jet thrust coefficient of 1.0.
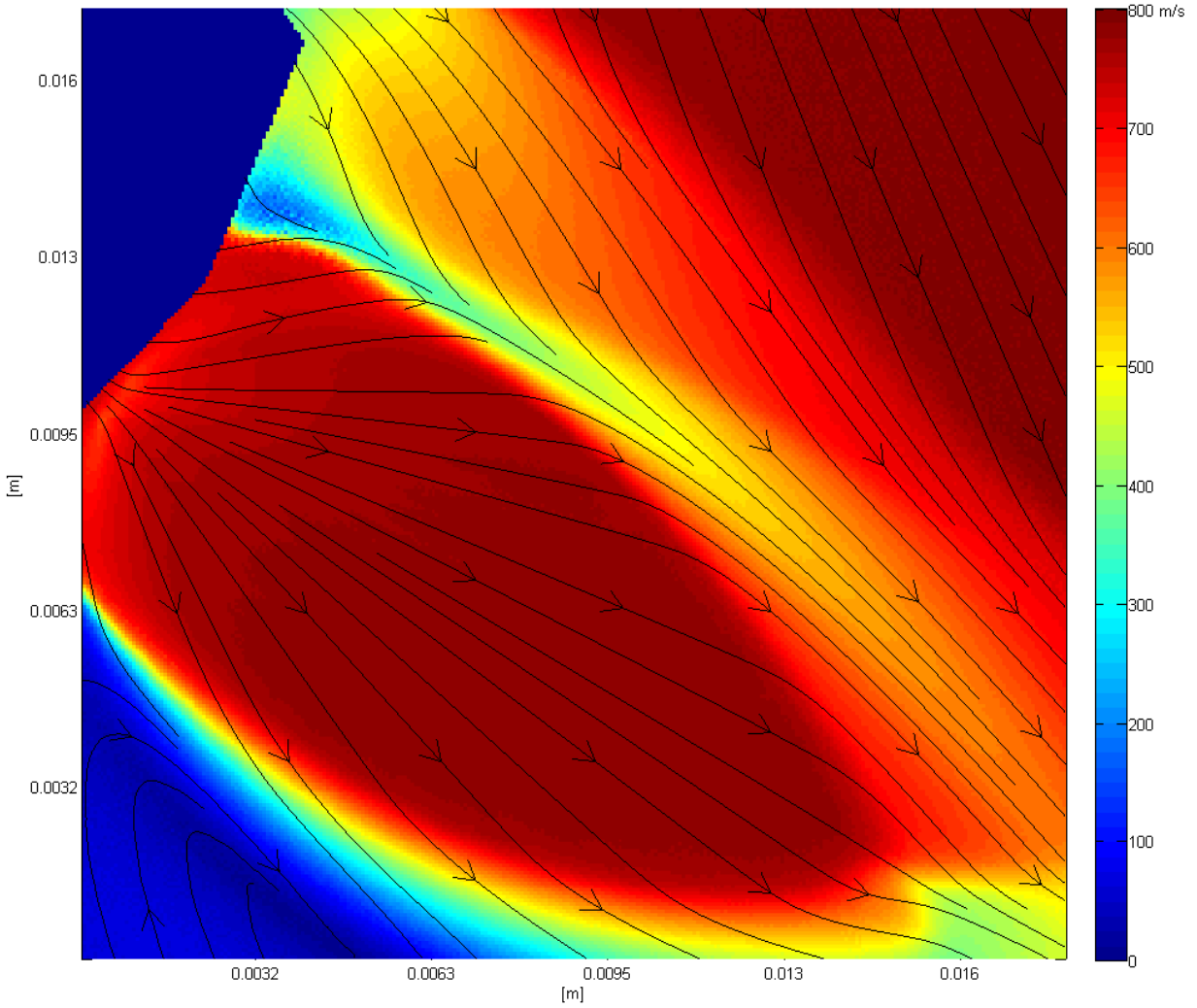
Figure 8.2: Planar velocity magnitude plot for RCS transverse jet at M_∞=12 and a jet thrust coefficient of 1.0. Streamlines are also shown.

For ease of discussion of the velocity flowfield, figure 8.3 shows the velocity flowfield image superimposed with labels of features in the flowfield of interest. A few terms will also be defined.
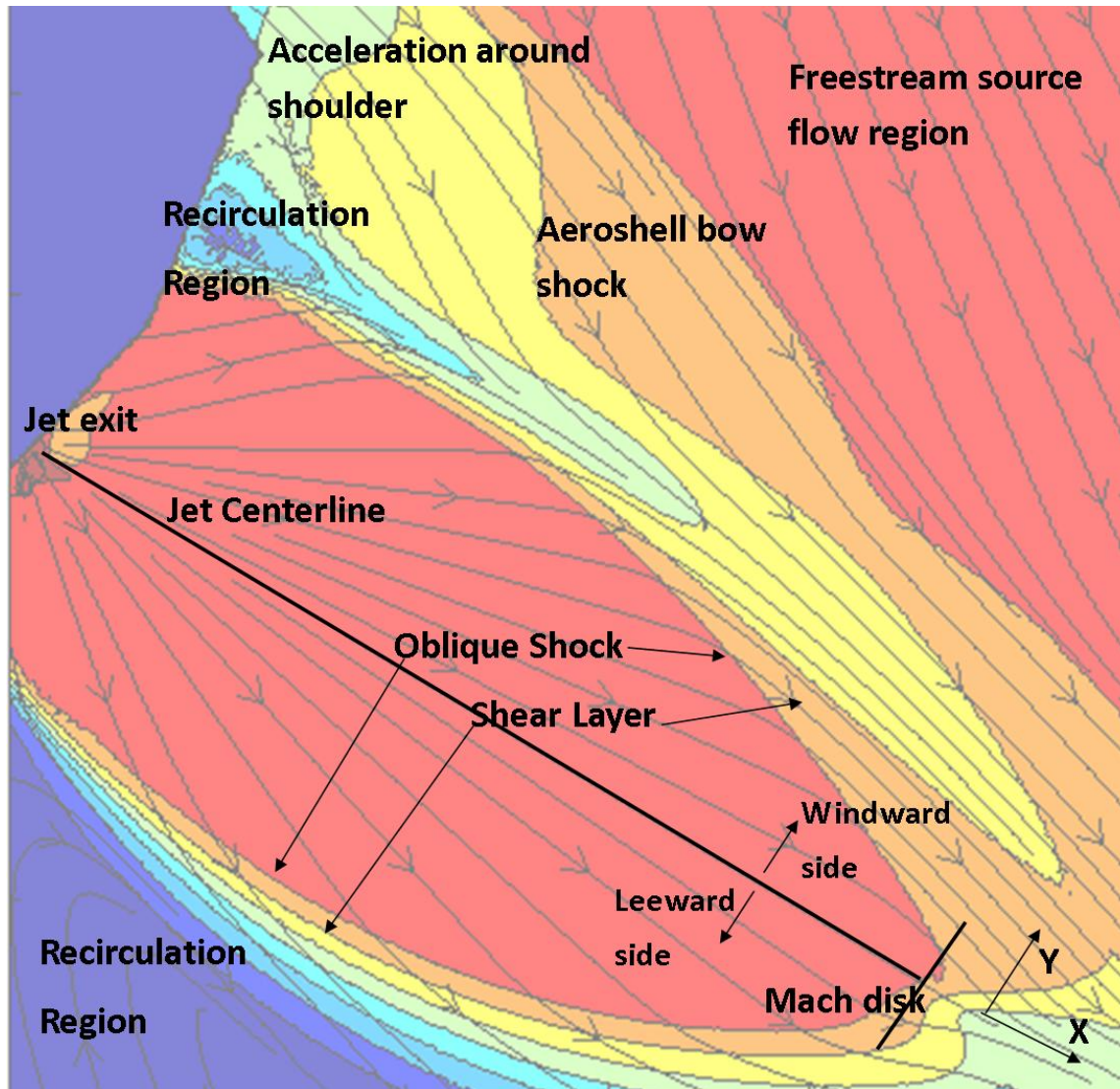
Figure 8.3 Features of the RCS transverse jet flowfield with $M_\infty=12$ and a jet thrust coefficient of 1.0.

The planar images are shown oriented with flow from top to bottom. However, much of the discussion will focus on values given along the RCS jet centerline. Thus, the x-direction is defined along the jet centerline, at a distance, x, from the jet exit (x=0) and the y-direction is perpendicular to the centerline. This x-direction will also be referred to as the axial direction, while the y-direction will also be referred to as the tangential direction. Because the model is oriented at a 20 degree angle of attack with respect to the freestream

flow, the shoulder of the model (surface discontinuity on model at top if image) protrudes into the flow and causes much of the RCS jet flow to interact strongly with the freestream flow as it accelerates around the shoulder and with the curved bow shock from the model. The region to the +y side of the RCS jet centerline is defined as "windward" region, while the region of the flow to the –y side is defined as the "leeward" region. These definitions are useful in the discussion to follow.

8.3 RCS Jet Structure and Oblique Shock

As seen in figures 8.2 and 8.3, the RCS jet streamlines radiate from the jet exit and expand outward as predicted by the Ashkenas and Sherman relationship for underexpanded jets [103]. An oblique barrel-shaped shock which forms around the RCS jet core can be clearly seen as the leeward jet boundary (near the recirculation region) with a steep velocity gradient across the oblique shock and shear layer. The windward boundary is not as clearly delineated due to the interaction with the bow shock, creating a large region between the shocks that still has significant velocity. The Mach disk (normal shock) at the termination of the RCS oblique barrel shock has an irregular shape between the leeward side and the windward sides, indicating influence from the windward side flow.

8.4 Aeroshell Bow Shock Structure

The freestream Mach 12 flow is compressed across the model bow shock. The flow behind the bow shock accelerates from a stagnation point on the surface of the model and around the shoulder of the model before interacting with the RCS jet. The bow shock

curves around the model but then bends away from the model as it interacts with the RCS jet. Potentially, there could be some interaction of the aeroshell bow shock with the barrel shock from the freestream test section shock structure which tends to turn the model bow shock away from the model toward the freestream test section triple point (not shown in these images). However, this interaction is not likely to be strong because the parametric study (Chapter Five) indicated little interaction. Downstream of the first shoulder of the model, there is a low velocity recirculation region between the flow accelerated around the shoulder and the RCS jet.

8.5 Freestream

The freestream streamlines outside the bow shock in the upper right hand part of the images radiate slightly outward from the model. This is as expected since the axisymmetric underexpanded jet core is essentially a source flow. Even though the model is placed far downstream (43 mm) of the main jet exit, a slight radial expansion is still observed. (This radial expansion is accounted for in the CFD model.)

The freestream has an average measured speed of about 785 m/s upstream of the model bow shock. At Mach 12 conditions, it is expected that the freestream has essentially reached its terminal velocity conditions. Terminal velocity is defined from the energy equation and is given in equation 8.1:

$$V_{terminal} = \sqrt{2 \cdot C_P \cdot T_0} \qquad\qquad (8.1)$$

in which C_p is the heat capacity of nitrogen , 1039 J/kgK, and T_0 is the stagnation temperature, 298 K. Using this definition, the terminal velocity is calculated to be 787 m/s, which yields a 0.2% difference from the measured freestream.

8.6 Recirculation Region

In the bottom left of the images is a recirculation region, with low speeds, near the leeward side of the RCS oblique shock. The speed in this region is everywhere less than about 50 m/s. Due to the low density in the wind tunnel, and being shielded from the freestream by the RCS jet core, this region is also very low density.

8.7 RCS Jet Centerline Velocity

The velocity along the centerline of the RCS jet is plotted in figure 8.4, along with the Ashkenas and Sherman relationship [103]. The Ashkenas and Sherman relationship is only shown for x/D greater than one. At x/D less than one, this relationship is inaccurate. In this figure, the PLIIF measurement and the Ashkenas and Sherman relationship show close agreement, with a difference of only about 10 – 15 m/s or a 1.3 – 3% difference, for x/D larger than 5. There is disagreement closer to the RCS jet exit. Although the impact shift is accounted for in the PLIIF model, inaccuracies in the numerical fits to the fluorescence spectra can produce pressures and temperatures which can result in higher PLIIF velocities. Also plotted on the centerline graph is the Mach disk (normal shock) location for the RCS transverse jet. This Mach disk location was calculated by taking the derivative of the

velocities across the shock wave to find the inflection point within the gradient. The Mach disk thickness is 5.85 mm. It is interesting to note that the structure of the normal shock, Mach disk, is very different from continuum in this rarefied flow, being much thicker. Also, note that the Ashkenas and Sherman relationship does not include considerations for the chamber back pressure and so does not show a location for the Mach disk. This relationship can be seen as a model of a pure expansion into a vacuum, as opposed to the low-pressure back pressure in the experiment. Overall, the measured PLIIF velocities in the RCS jet agree well with the Ashkenas and Sherman relationship, especially at the higher Mach numbers where the impact shift is negligible.
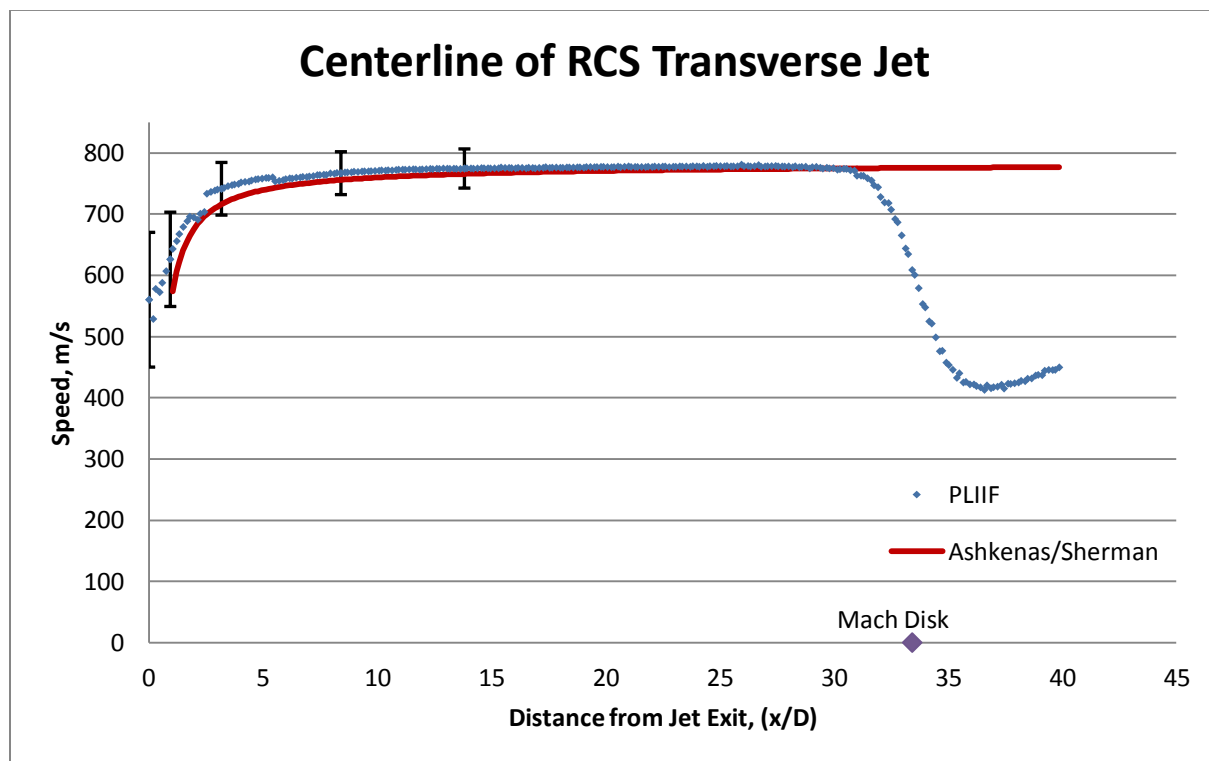
Figure 8.4 Velocity profile along the centerline of RCS transverse jet with a thrust coefficient of 1.0, with error bars for velocities at Mach 1, 2, 5, 8 and 10 conditions shown.

The velocity magnitudes at cross-sections normal (in the y-direction) to the RCS jet centerline, at various distances from the jet exit, are shown in Figure 8.5. In this figure, the cross-sections show the velocities in the low velocity recirculation region on the RCS leeward side, the oblique barrel shock on either side of the RCS jet core, the region between the oblique shock and the model bow shock, and the bow shock off the model.
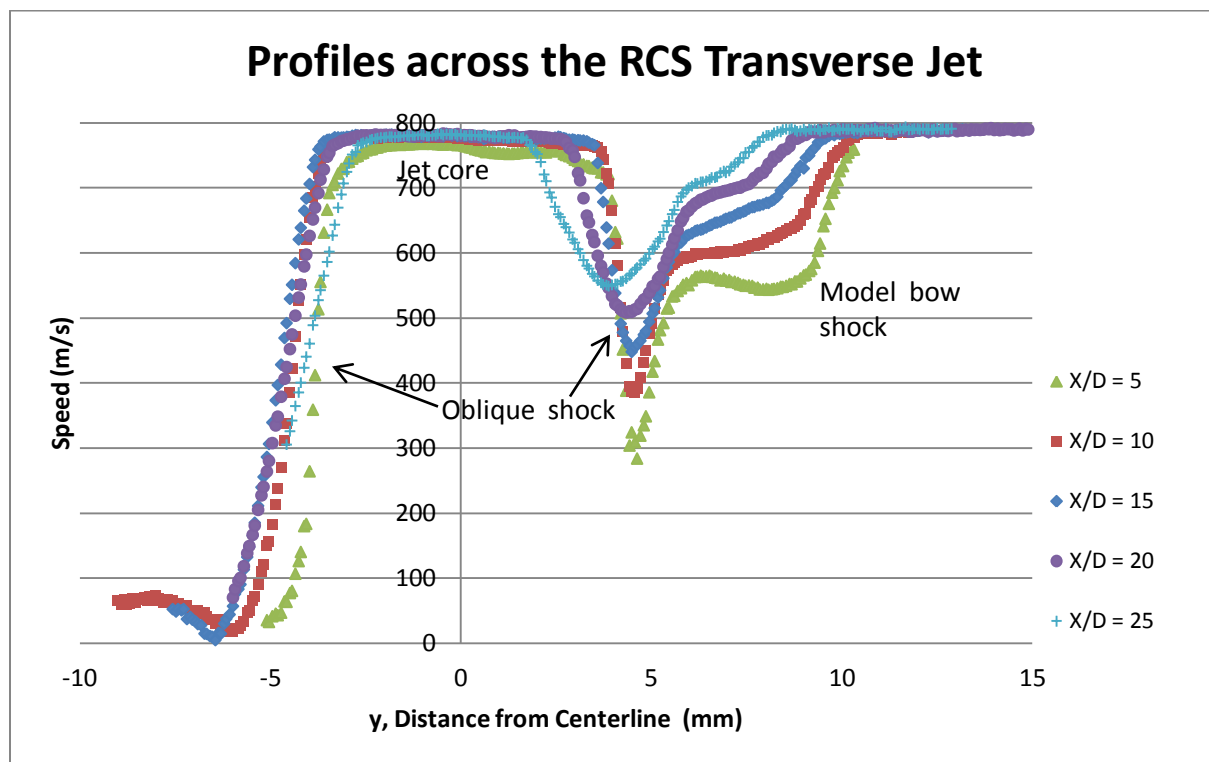
Figure 8.5 Velocity magnitudes at cross-sections normal to RCS transverse jet centerline with a thrust coefficient of 1.0.

In examining the cross-section profiles, a few observations can be made. First, as the RCS jet flow moves farther from the jet exit (increasing x), the jet structure widens and then narrows near the Mach disk. This is consistent with the shape of the shock barrel.

94

The widest part of the barrel shock structure occurs at the profile x/D = 15.   The oblique shock on the leeward side of the RCS jet in figure 8.2 (and 8.3) widens from a width of 1.81 mm along a cross-sectional profile 5 jet diameters from the RCS jet exit to a thickness of 2.85 mm along a cross-sectional profile 15 jet diameters from the RCS jet exit. Conversely, on the windward side of the jet, the jet actually narrows and the oblique shock shown in the profile moves closer to the centerline. Also, on the windward side of the jet, the minimum velocity between the barrel shock surrounding the RCS jet and the bow shock off the model increases with increasing distance along streamlines (from about 284 to 552 m/s), indicating an acceleration of this mixing region by the RCS jet. The cross-sectional profiles also show the behavior of the bow shock off the model as it moves further downstream (+x direction). The velocity gradient indicated the model bow shock is the thickest shock in the profiles, indicating instead a merged shock with the mixing region between the aeroshell bow shock and the RCS oblique shock. It has a thickness of 5.9 mm at x/D = 5 compared to the leeward oblique shock thickness of 1.81 mm. This merged model bow shock actually narrows slightly (from 5.9 mm to 4.52 mm) at greater x/D. The velocity gradient is very pronounced across the model bow shock but at greater distances from the jet exit, this velocity gradient becomes less pronounced.

8.8 Temperature

The temperature field for the RCS transverse jet is shown in figure 8.6, plotted on a semi-log scale in order to better highlight the small temperature variation.
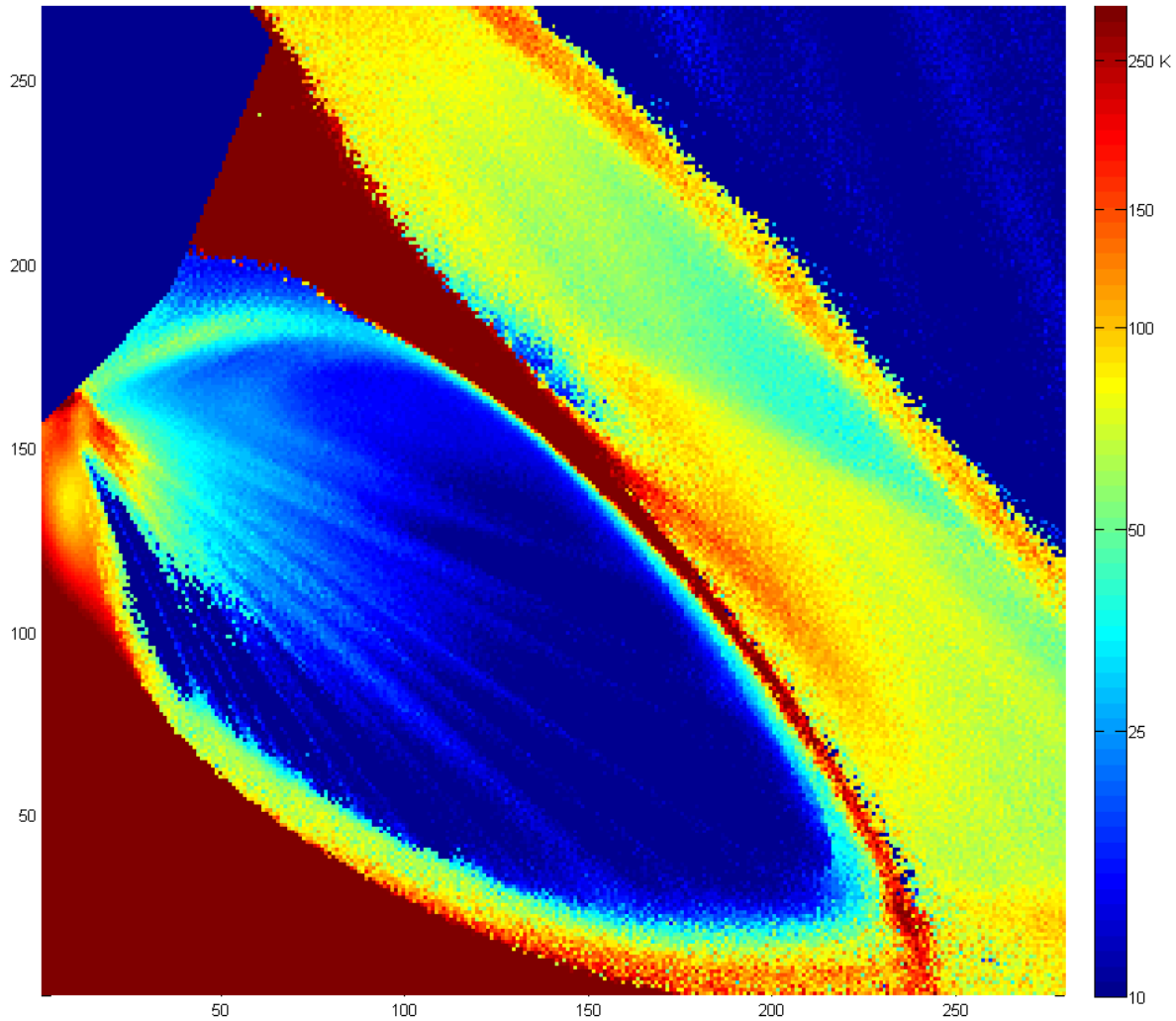
Figure 8.6 Temperature field for the RCS transverse jet with a jet thrust coefficient of 1.0.

Within the RCS jet core, the temperature decreases as the flow expands outward from the RCS jet exit. (The presence of streaking in the jet core currently cannot be explained, but must be an optical effect and not due to the flow mechanics.) The temperature rises downstream across the Mach disk. One either side of the RCS jet, in the flow recirculation region, the temperature is close to stagnation temperature. It is important to note that these recirculation regions at these higher temperatures are regions that are likely to result in total temperature recovery given MSL conditions, which could induce localized heating

on the back of the aeroshell. In the mixing region between the RCS oblique shock and the model bow shock, the temperature stays largely around 75 K. In the freestream, the temperature is cold, around 10 K.

The temperature along the centerline of the RCS jet can be plotted in comparison to the isentropic conditions of the flow, given the Ashkenas and Sherman relationship, as shown in figure 8.7 [103]. These values are plotted on a semi-log scale in order to better show the temperature variation in the jet core. The temperature in the experiment appears to reach a minimum temperature of 10 K, while the Ashkenas-Sherman relationship continues to decrease to very low absolute temperatures. The compression across the Mach disk is not included in the Ashkenas and Sherman relationship.
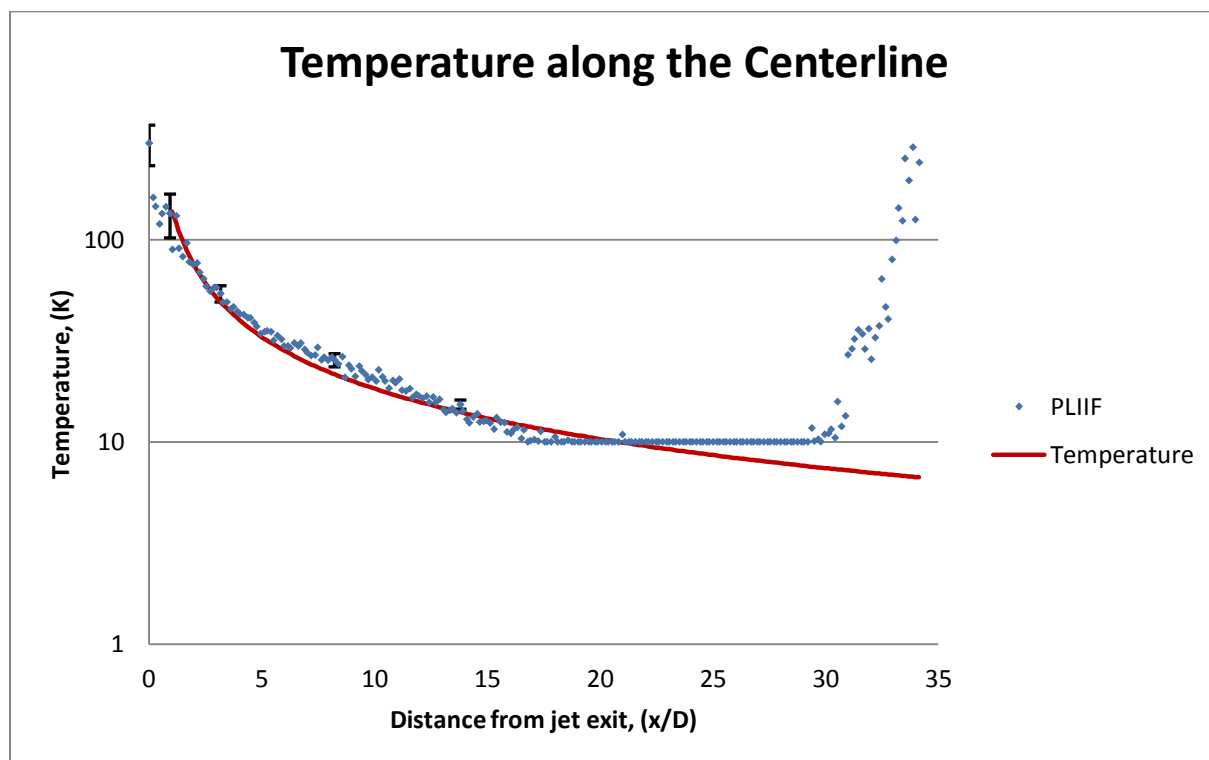
Figure 8.7 Temperature profile along centerline of RCS transverse jet with a thrust coefficient of 1.0, with error bars for temperatures at Mach 1, 2, 5, 8 and 10 conditions shown.

The temperature along the jet centerline matches quite closely with what is predicted using the isentropic relations in conjunction with the Ashkenas-Sherman relation, with an average temperature difference of 0.5 K, or 8.64% with a standard deviation of 4.8 K.

8.9 Mach Number

With the velocity and temperature calculated, it is possible also to calculate the planar Mach number field given the equation 8.2:

$$M = \frac{u}{\sqrt{\gamma RT}} \tag{8.2}$$

where γ is 1.4 for nitrogen, and R is the gas constant for nitrogen, 296.8 J/kgK. The Mach number field for the RCS transverse jet is given in figure 8.8.
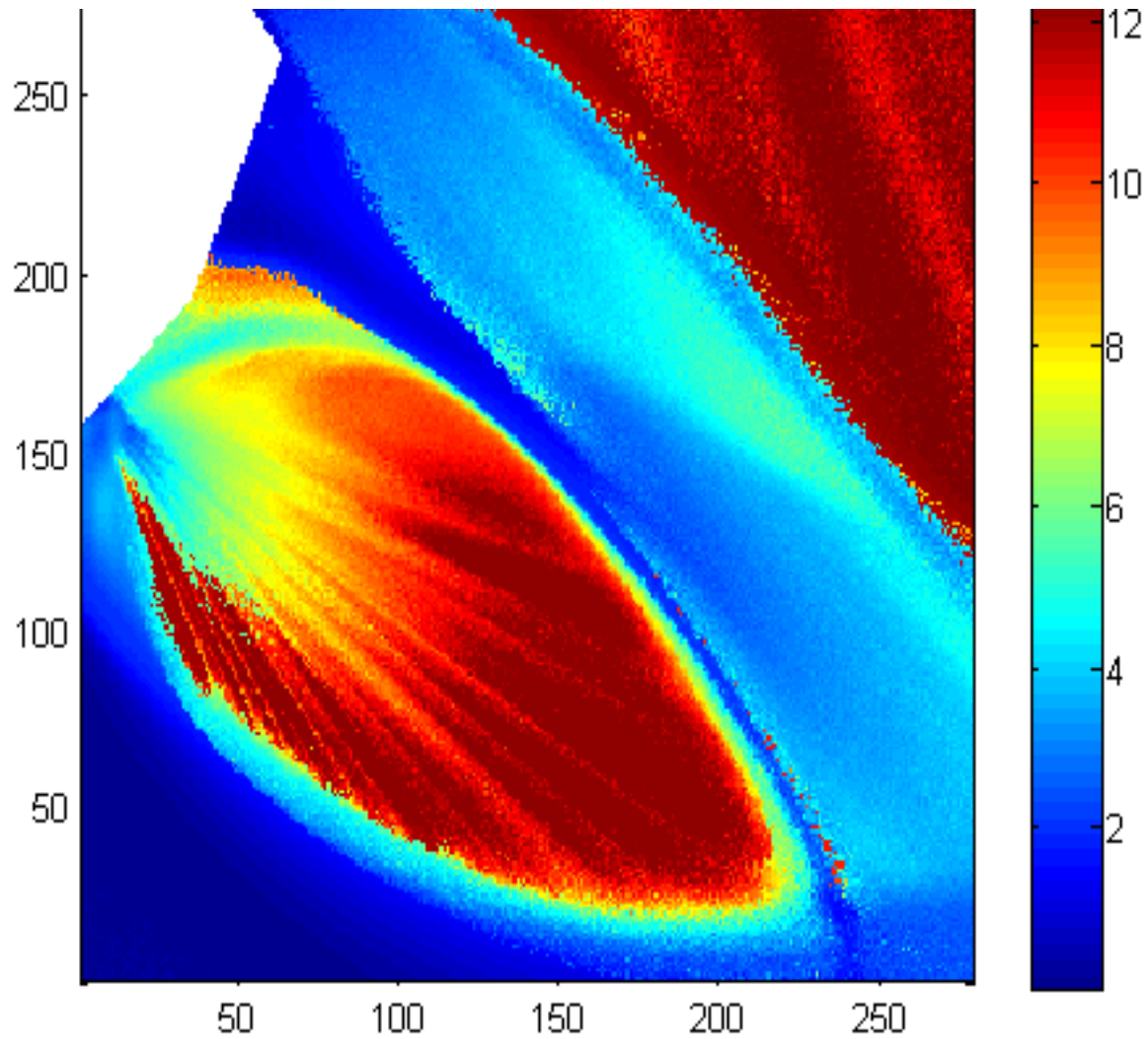
Figure 8.8: Mach number distribution for planar flowfield of RCS transverse jet with a thrust coefficient of 1.0.

According to the figure, the RCS jet core rapidly increases in Mach number to a terminal Mach number of 12 before the Mach disk. The Mach number decreases across the Mach disk normal shock, as expected. The mixing region between the RCS oblique shock and the aeroshell's bow shock shows a fairly low supersonic Mach number. The freestream region shows a value of Mach 12 and the recirculation regions shows Mach numbers around zero.

(Again the streaking structure in the jet core is likely due to an unexplained optical, not fluid mechanical, effect.)

CHAPTER NINE

PARALLEL JET QUANTITATIVE RESULTS

9.1 Introduction

The velocity and temperature fields for a parallel RCS jet configuration, at a jet thrust coefficient of 1.0, have been solved using the spectral data analysis program on the University of Virginia Unix Cluster. The results are presented herein and discussed in detail. Due to the fact that the parallel jet in the qualitative images showed very little interaction with the model bow shock, this orientation is more useful for CFD comparisons than the RCS transverse jet configuration. The results for the parallel jet are also compared to predictions made by the Ashkenas and Sherman relations based on the method of characteristics [103]. With the flowfield velocity and temperature determined, Mach number is also calculated and presented.

9.2 Velocity

The 2-D velocity vectors for the parallel RCS jet with a thrust coefficient of 1.0 are shown in the Figure 9.1. For clarity, the vectors are shown at every tenth pixel, rather than at every pixel. Magnitudes superimposed with flow streamlines are shown in figure 9.2.

In both of these images, the Mach 12 flow is from top to bottom and is parallel to the

edge of the image. The MSL model is shown blocked out in the top left hand corner of each
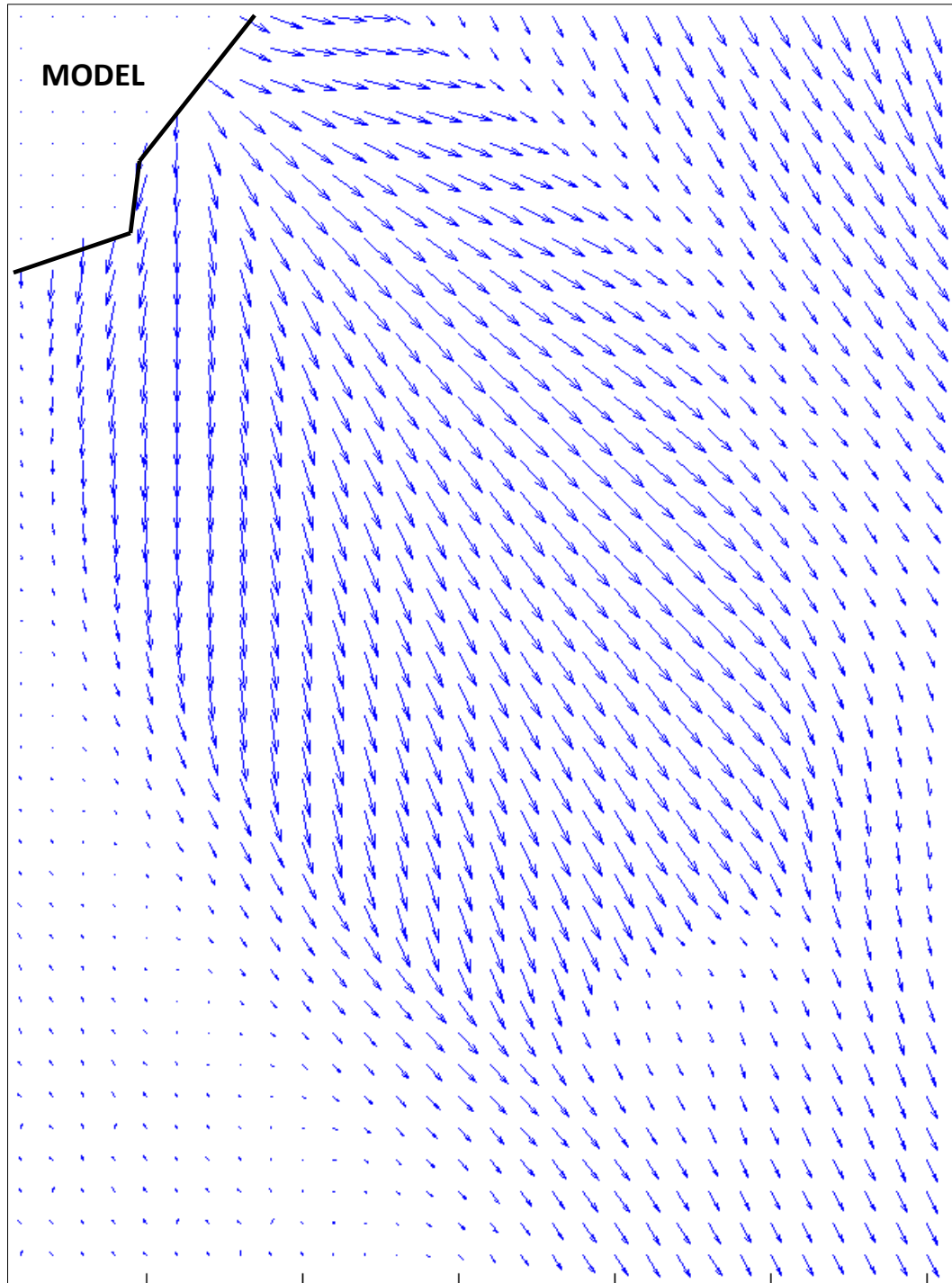
Figure 9.1 Planar velocity vector plot for parallel RCS jet with $M_\infty=12$ and a thrust coefficient of 1.0.

figure. The shoulder of the model is not seen in figures 9.1 or 9.2. The jet exit is located at the edge of the model where the RCS jet velocity vectors (or streamlines) radiate outward.
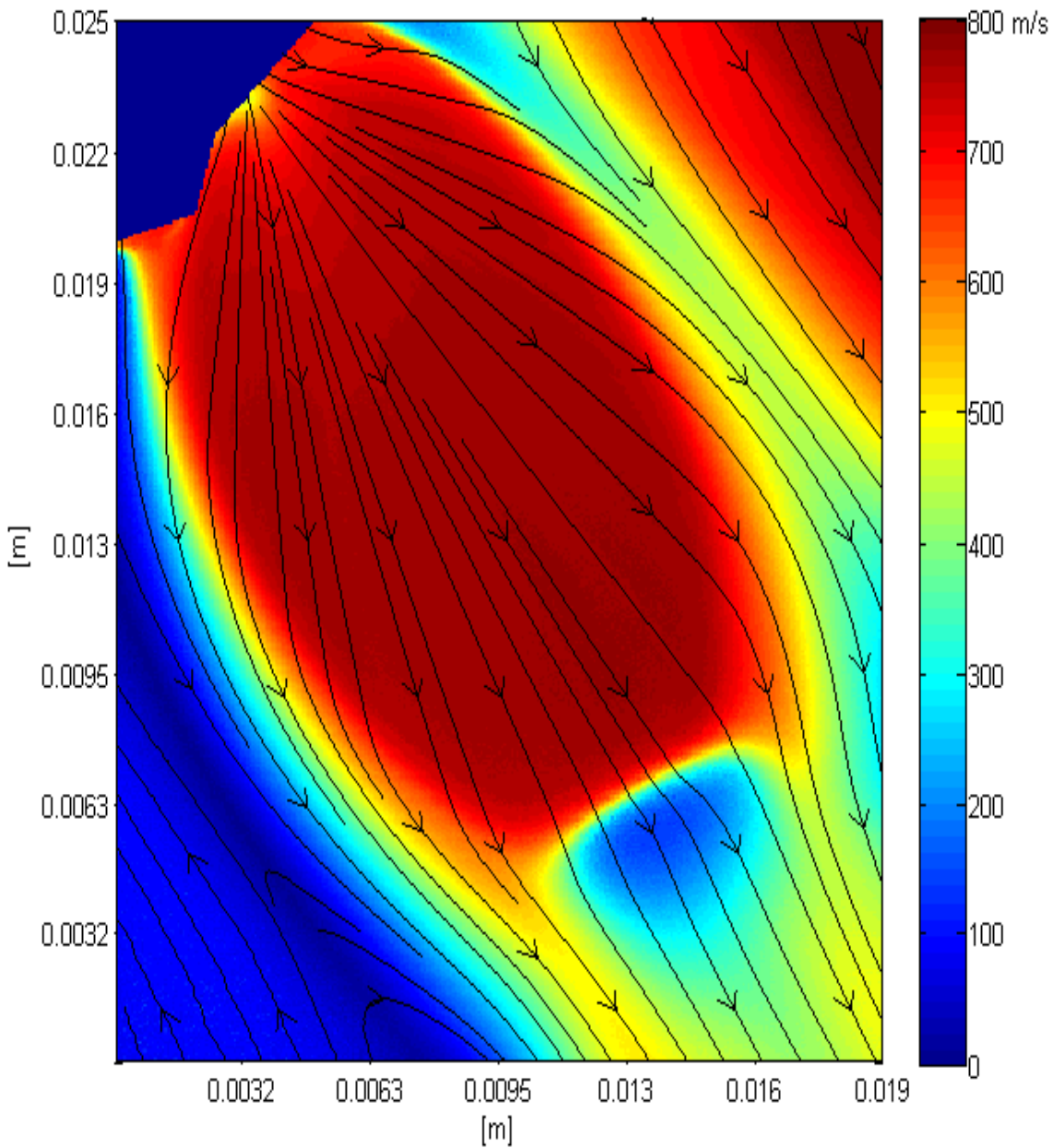
Figure 9.2 Planar velocity magnitude plot of a parallel RCS jet at M_∞=12 and a thrust coefficient of 1.0. Streamlines are also shown.

For ease of discussion of the velocity flowfield, figure 9.3 shows the velocity flowfield image superimposed with labels of features in the flowfield of interest. The same definitions and conventions used in Chapter Eight for the flowfield discussion are applied here. The x-direction for the field is taken along the centerline, extending out from the jet exit, while the y-direction is perpendicular to the centerline. The axial and radial directions refer to the x-direction and the y-direction, respectively. Each of the flowfield features will be discussed in turn.
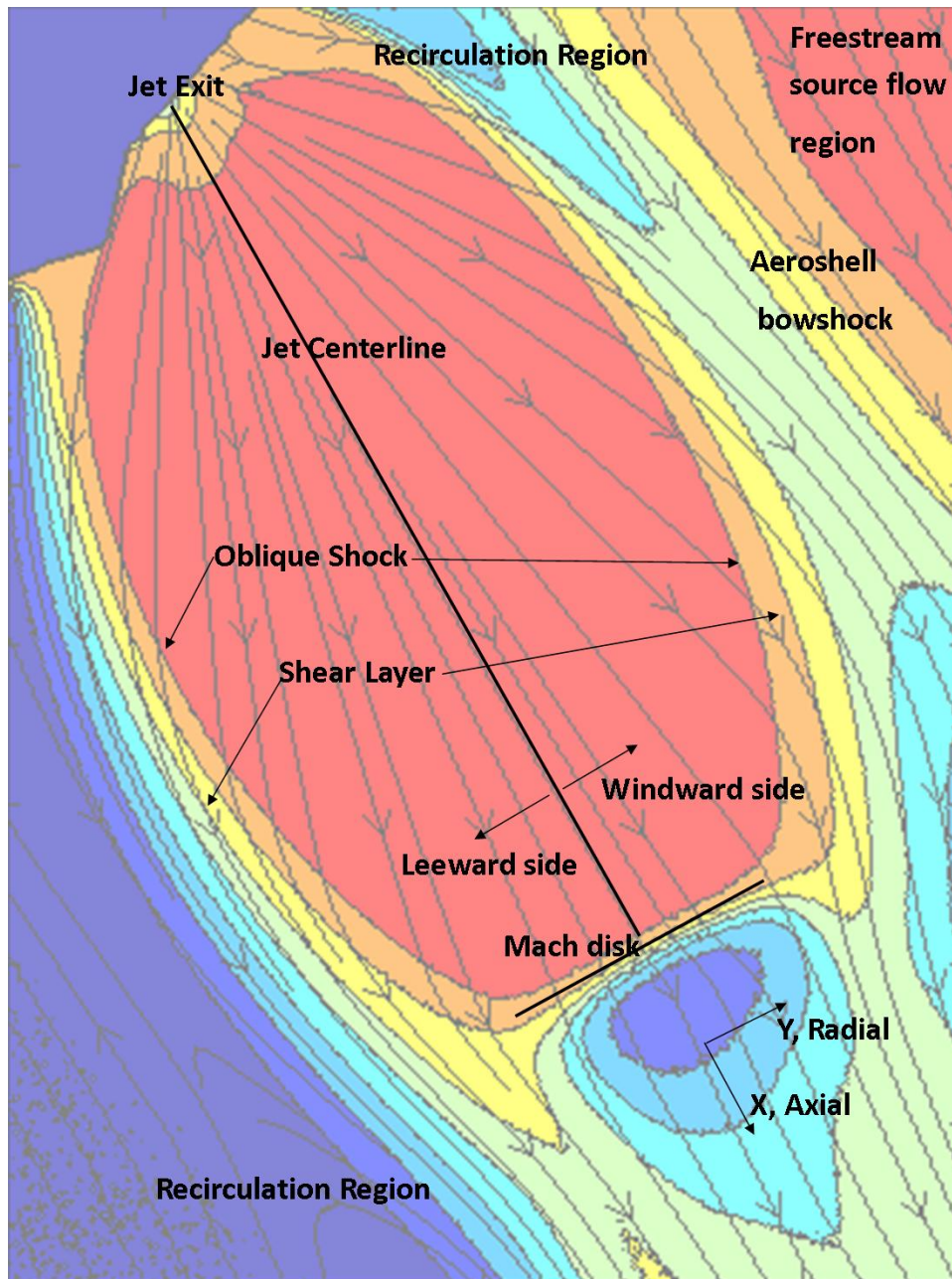
Figure 9.3 Features of the parallel RCS jet flowfield with $M_\infty=12$ and a thrust coefficient of 1.0.

9.3 RCS Jet Structure and Oblique Shock

As seen from the images above, the RCS jet expands from its sonic exit to form a symmetric jet that increases in speed until it terminates in a very distinct Mach disk, across which the velocity magnitude drops significantly. The oblique barrel shock around the RCS

jet structure has a distinct structure. Because the windward and leeward sides of the oblique shock boundary both show similar shape and structure, this suggests that the windward side is little affected by the bowshock that forms off the model. This lack of interaction between the bow shock and the RCS jet structure can also be seen clearly in the streamlines. As the streamlines show, the jet expands from the jet exit and radiate outward. This flow then bends as it crosses the barrel shock of the RCS jet. If one examines the streamlines in the jet core on either side of the centerline, it is clear that there is little influence from external conditions either on the leeward side or the windward side of the jet.

9.4 Aeroshell Bow Shock Structure

The shoulder of the model is not shown in the flowfield. However, when the freestream impinges on the shoulder, flow accelerates around the shoulder of the model behind the aeroshell bow shock, as labeled. The recirculation region behind the shoulder of the model can be seen. The bow shock off the model appears to have little interaction with the oblique shock of the RCS jet. The region between the freestream bow shock and the RCS jet structure indicates velocity values around 200 m/s, which is much lower than the freestream or the velocity magnitudes in the RCS jet. It can be assumed from the presence of this low velocity region, that the area downstream of the shoulder of the model is a separated or recirculating region, but one that is much larger than the one that exists in the RCS transverse jet case.

9.5 Freestream

In the top right hand corner of figures 9.1-9.3, the freestream can be seen upstream of the model bow shock. In the upper right corner, the freestream streamlines radiate outwards slightly, as expected from the underexpanded jet in the main flow. The average measured velocity in the freestream is 781 m/s, which only differs from terminal velocity of 785 m/s by a 0.5% difference.

9.6 Recirculation Region

The low velocity region in the leeward side of the RCS parallel jet (on the lower left hand side of the image) shows large recirculation near the barrel shock boundary of the RCS jet. This recirculation region indicates a vortex driven by the RCS jet.

9.7 RCS Jet Centerline Velocity

The centerline velocity variation is given in Figure 9.4, together with the Ashkenas-Sherman relationship for this underexpanded jet [103]. The Ashkenas and Sherman relationship is only plotted for x/D values above one, due to inaccuracy of the relationship at x/D near the jet.
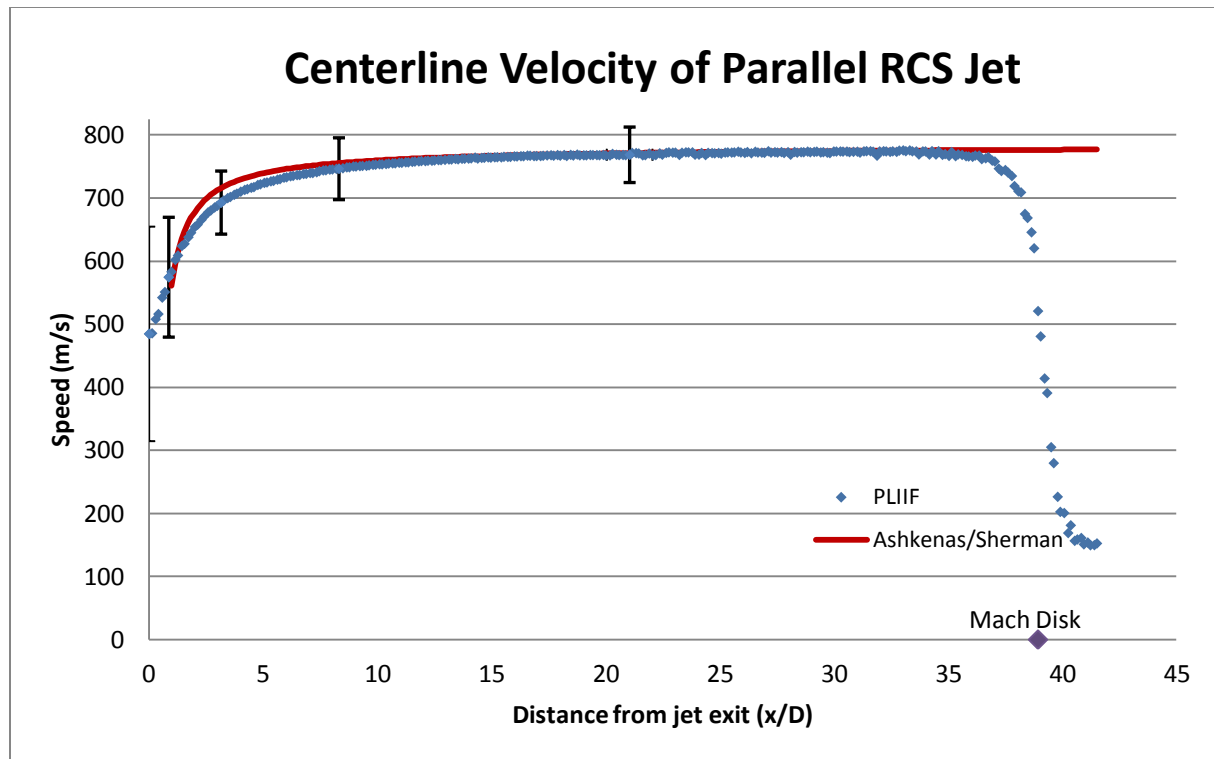
Figure 9.4 Centerline velocity magnitude for RCS parallel jet configuration with a thrust coefficient of 1.0, with error bars for velocities at Mach 1, 2, 5, 8 and 10 conditions shown.

The PLIIF quantitative data agrees very well with the Ashkenas and Sherman relationship, with an average difference of only about 3.3 m/s, or 0.5%, downstream of x/D = 8; however, nearer the jet exit (from a distance of 1 to 8 x/D), the difference is greater, ranging from a difference of 5 – 25 m/s (0.7 to 3.6% error). This figure shows very good agreement, giving confidence in the PLIIF measurements. The velocity change across the Mach disk is also very clearly evident and from this profile. The Mach disk location, shown in figure 9.4, was calculated by taking the derivatives of the velocities across the Mach disk to find the inflection point within the velocity gradient. It is also possible to calculate the Mach disk thickness, which is 1.46 mm. In a continuum region, the normal shock is a sharp discontinuity but at this rarefied condition, the shock broadens considerably.

Cross-sections of the RCS jet taken normal to the jet centerline at various distances from the jet exit are shown in figure 9.5. The y-axis (x=0) marks the centerline of the parallel jet and positive y indicates the windward side of RCS jet structure. To orient the reader, the flowfield features are labeled.

Parallel RCS Jet, $C_T = 1.0$
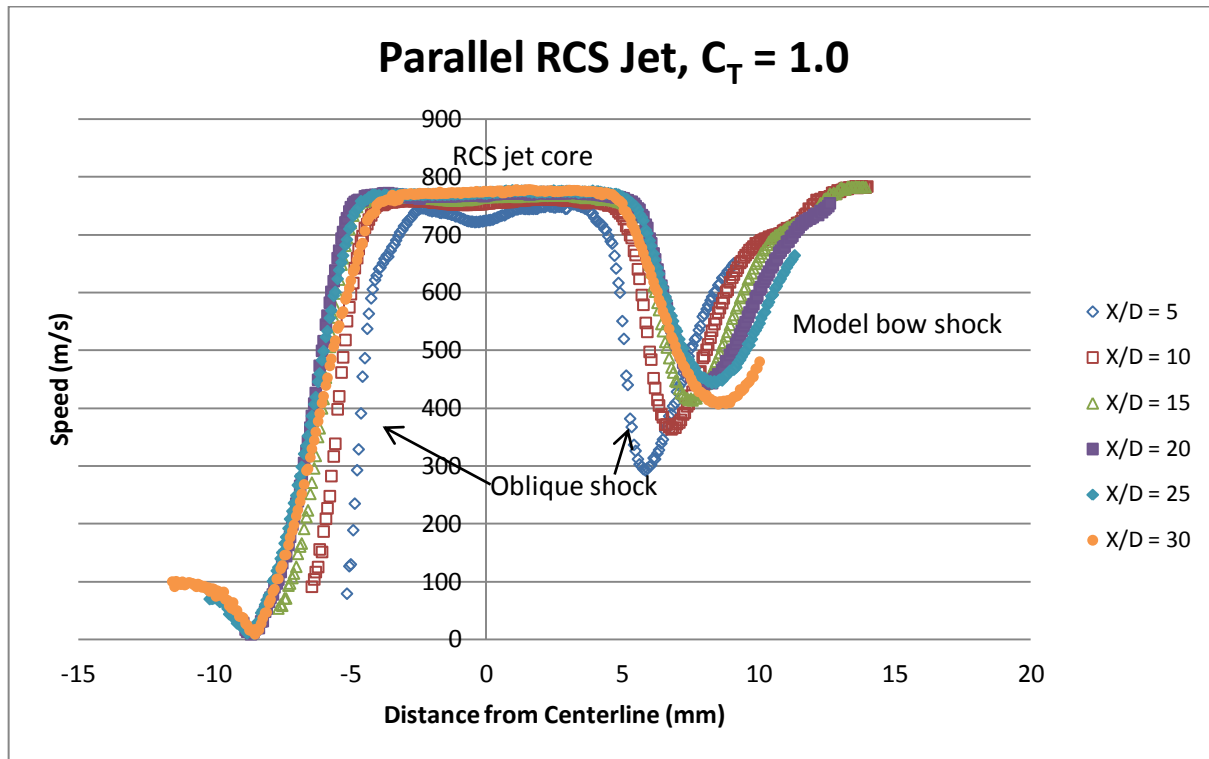
Figure 9.5 Velocity magnitudes at cross-sections through the RCS parallel jet with a thrust coefficient of 1.0.

It is clear that as the RCS jet expands from the exit, the isentropic jet core widens somewhat; however, at x/D = 20, the jet reaches its widest point and then narrows in width as it nears the Mach disk. This behavior is demonstrated on both boundaries of the RCS jet. The oblique barrel shock and shear layer thickness increases slightly downstream from the jet

exit from 3.3 mm at a cross section at 15 jet diameters to a thickness of 4.5 mm at a distance of 30 jet diameters.

Due to the presence of the freestream and the bow shock off the model, the minimum velocity on the windward side (positive y-direction) of the RCS jet does not reach the same minimum velocities as it does on the leeward side. The minimum velocity at a distance of x/D = 5 is 302 m/s, increasing to 451 m/s at a cross-section 25 jet diameters from the jet. The magnitude of this minimum velocity actually decreases at the cross-section that is 30 jet diameters from the exit to a value of 409 m/s (9% decrease). From the velocity gradient across the model bow shock, it appears that the shape and thickness is little affected by the RCS jet oblique shock and jet structure. Furthermore, it is clear from the symmetric shape of the RCS jet and oblique shocks that the model bow shock does not influence the RCS jet structure, as was seen with the transverse case (compare to figure 8.5). This would indicate that there is little interaction between the RCS jet and the model bow shock.

9.8 Temperature

The temperature field, plotted on a semi-log scale, for the parallel RCS jet with a thrust coefficient of 1.0 is shown in figure 9.6.
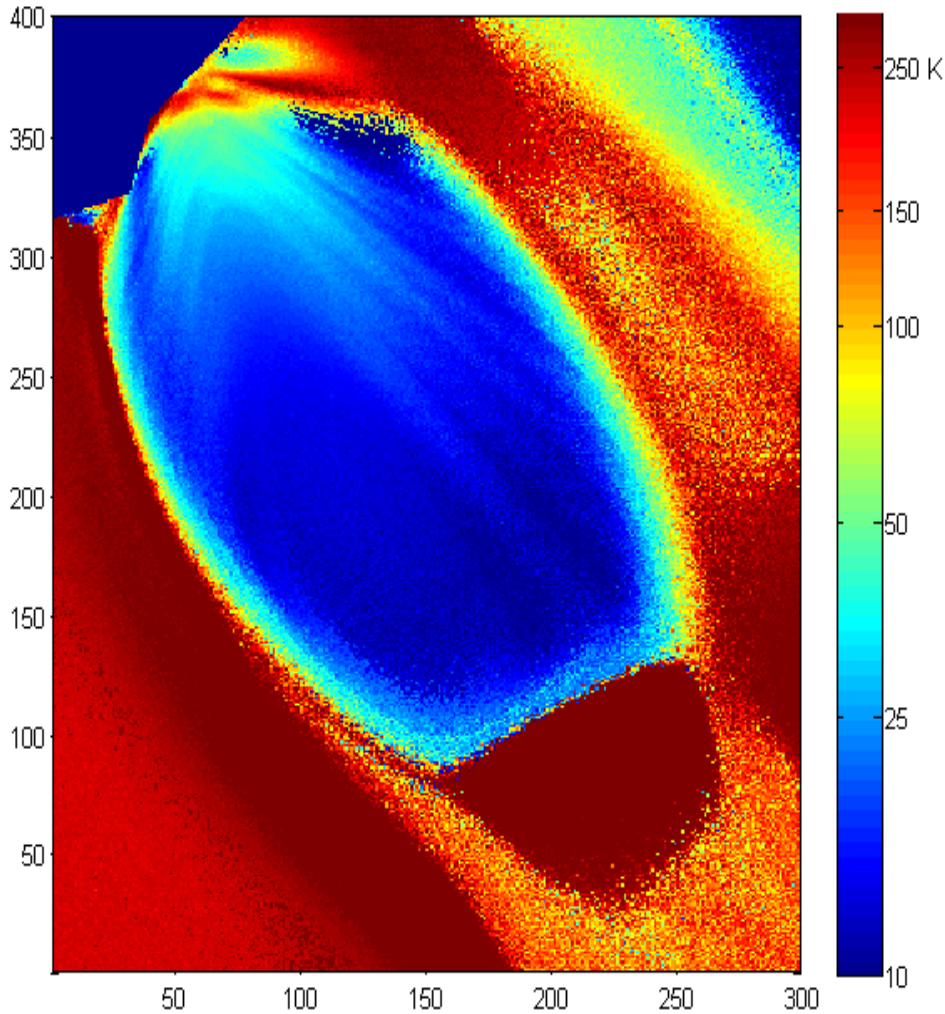
Figure 9.6 Temperature field for the RCS parallel jet with a jet thrust coefficient of 1.0.

In examining the temperature field closely, it is apparent that temperature throughout the core of the RCS jet is very cold (around 10K) and increases to about the stagnation temperature of 300 K in the oblique shock/shear layer region just outside of the RCS jet structure. The freestream region upstream of the model bow shock also exhibits low temperatures, and increases in temperature through the bow shock. In the region between the oblique shock and the bow shock, temperatures range between 75 and 125 K. In the leeward region of the RCS jet, the temperature is around 250 K. The Mach disk shows

compression, increasing the temperature to 250 K through the shock. However, in the subsonic region, after the shock, the temperature appears to decrease again, although the data here is noisy. For application to the MSL and potential of the RCS jet's influence on the aeroshell, the temperature field gives some insight. Near the model, on both the leeward and windward sides of the RCS jet, the temperature has recovered to near stagnation temperature conditions. It is important to note that these high-temperature, low velocity recirculation regions are potential regions where total temperature recovery could occur, resulting in augmented or localized heating on the MSL aeroshell.

The temperature field along the jet centerline is plotted on a semi-log scale in figure 9.7 below. Also shown are the temperature calculated using isentropic flow equations with the Ashkenas and Sherman relationship [103].
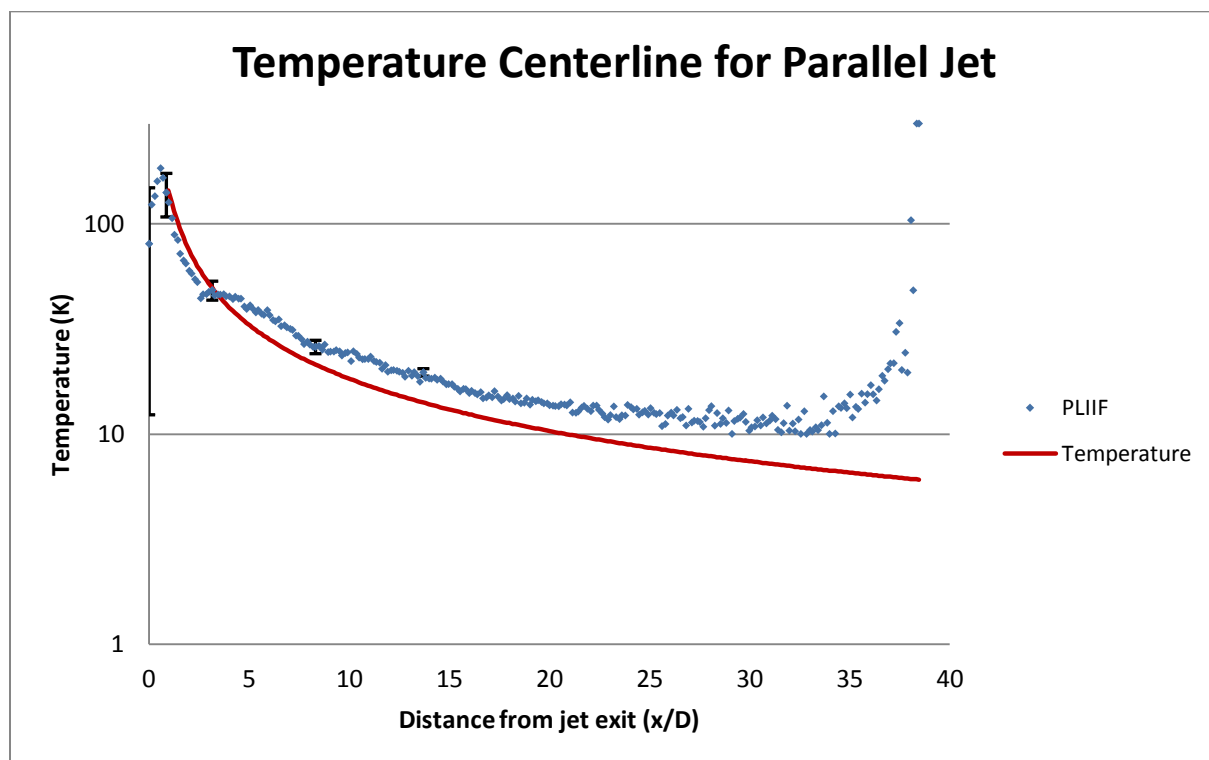
Figure 9.7 Temperature along parallel RCS jet centerline, with error bars for temperatures at Mach 1, 2, 5, 8 and 10 conditions shown.

The experimental data shows an average difference of 5.1 K (average 25% difference) from the temperatures calculated from the Ashkenas and Sherman relationship and the isentropic relationships throughout the length of the centerline. Overall, there is good agreement in trend and magnitudes.

9.9 Mach Number

With the velocity and temperature fields measured, it is possible to calculate the Mach number field, which is shown in figure 9.8.
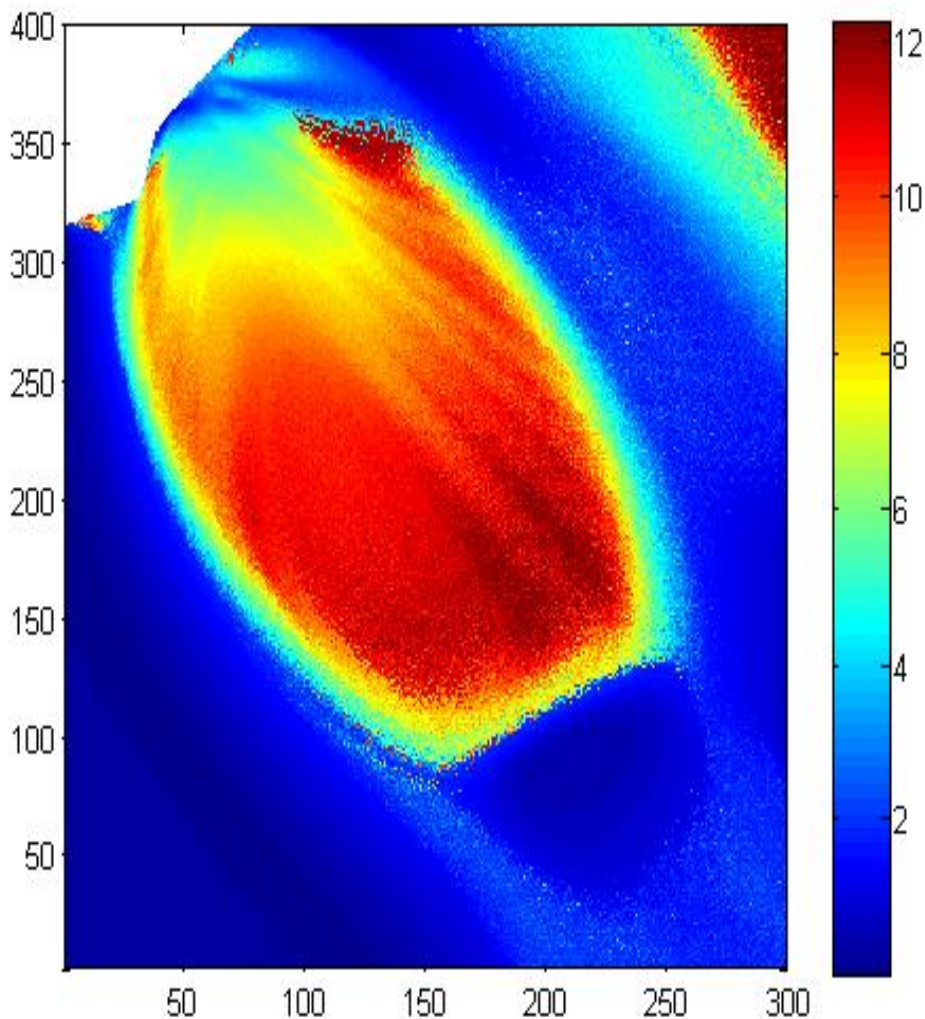
Figure 9.8 Mach number field for parallel RCS jet with a thrust coefficient of 1.0.

From this figure, it is clear that as the RCS jet expands in the jet core, the Mach number increases to a maximum value of Mach 12. Because the Mach disk is a normal shock, it is possible to compare pre- and post-shock conditions using the normal shock relations. The post-shock Mach number for a normal shock wave is given in equation 9.1

$$M_2^2 = \frac{(\gamma-1)M_1^2+2}{2\gamma M_1^2-(\gamma-1)} \tag{9.1}$$

in which 1 and 2 refer to pre- and post-shock conditions, respectively and γ is 1.4 for nitrogen gas. The value of the post-shock Mach number in this flowfield is 0.44, which is a 15% difference from the value of that predicted from normal shock relations at Mach 12. In the oblique shock/shear layer regions, the Mach number drops across the shock to low subsonic conditions. The freestream is at Mach 12 and then drops in Mach number across the model bow shock to subsonic conditions as well.

9.10 Comparison to RCS Transverse Jet Structure

It is possible to compare the two RCS jets and their structures in order to better understand the effect of the model bow shock on the structure of the RCS jet. The centerlines of the velocity magnitudes of the two configurations are plotted in figure 9.9. Again, the shock thicknesses of the Mach disk for the parallel and transverse cases are 2.6 mm and 2.7 mm respectively. These shocks are thickened because the jets are in rarefied flow. The Mach disk is located farther from the jet exit in the parallel case. From the characterization of the underexpanded jet by Ashkenas and Sherman, it is possible to calculate the back pressure downstream of the Mach disks, given the distance to the Mach disk [103]. (Note that this back pressure is expected to be different from the chamber back

114

pressure because the model and RCS jet are located within the test section formed by the barrel shock of the main jet.)
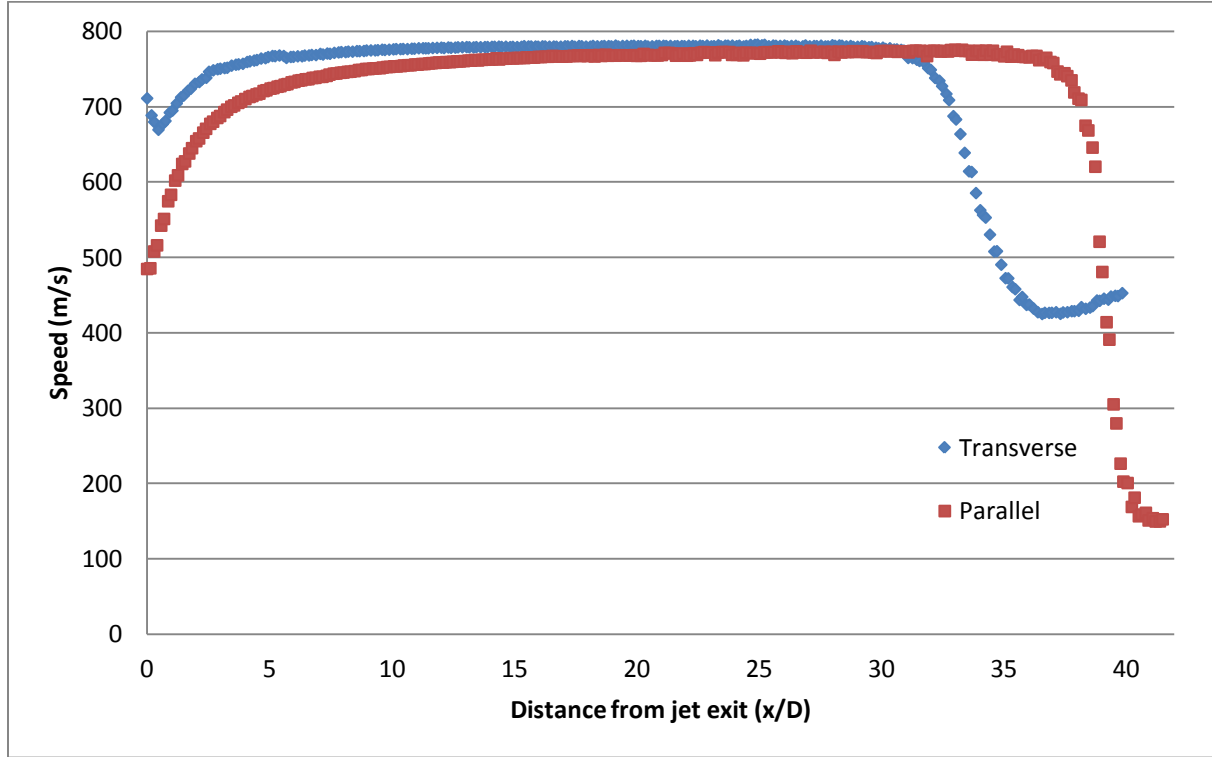
Figure 9.9 Centerline velocity comparison of transverse and parallel RCS jet configurations for a jet thrust coefficient of 1.0.

The Ashkenas and Sherman relationship for the Mach disk location is given in Equation 9.2 [103]:

$$p_b = p_{0,jet} \left(\frac{0.67}{x_M/D_{jet}} \right)^2 \qquad (9.2)$$

in which p_b is back pressure behind the Mach disk, $p_{0,jet}$ is the RCS jet stagnation pressure, and x_M/D_{jet} is the distance to the Mach disk, x_M, normalized by the jet diameter. Using this equation, the calculated back pressures of the parallel and transverse RCS jet configurations are 360 and 476 mTorr, respectively. It is significant that a 100 mTorr

difference in pressure results in a longer (and as will be seen later, a wider) jet structure. With a larger pressure difference, the parallel underexpanded jet expands further into the low pressure region.

The velocity magnitudes on cross-sections of the RCS jet are shown in figures 9.10 through 9.13 at different locations along the jet centerline.

Figure 9.10 Cross-section velocity for x/D = 5

Figure 9.11 Cross-section velocity for x/D = 10

Figure 9.12 Cross-section velocity for x/D = 15

Figure 9.13 Cross-section velocity for x/D = 20

From the discussion above, it is expected, and shown in these figures, that the parallel RCS jet not only has a longer jet structure th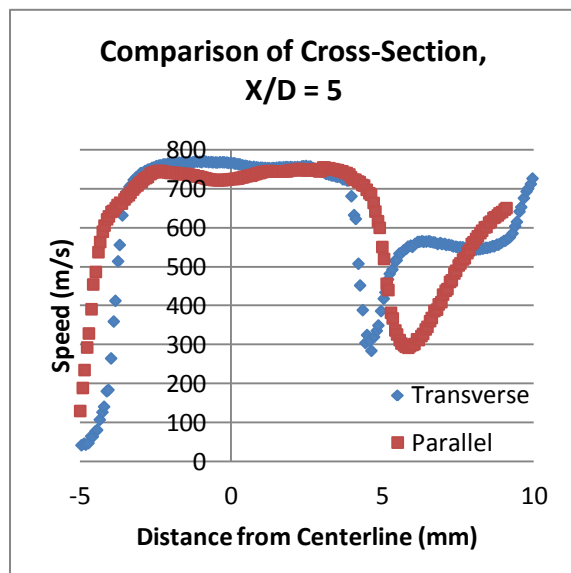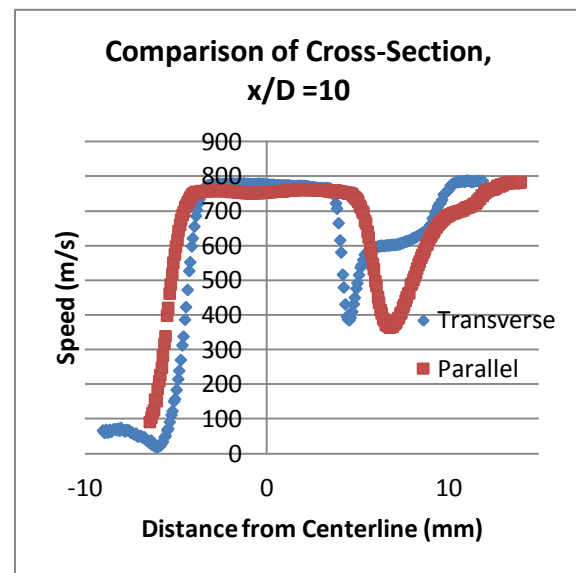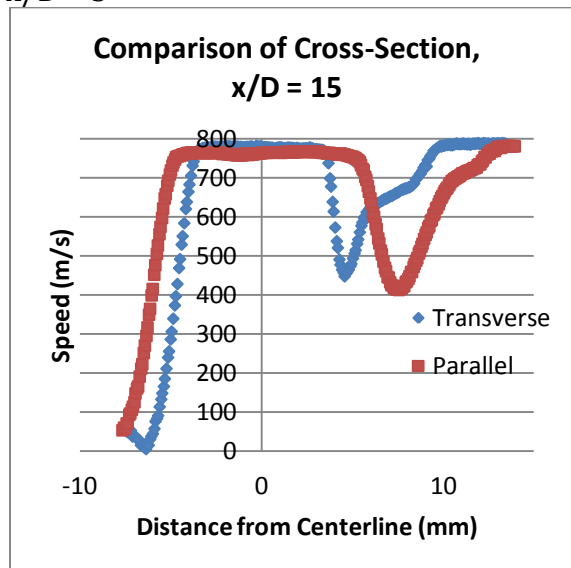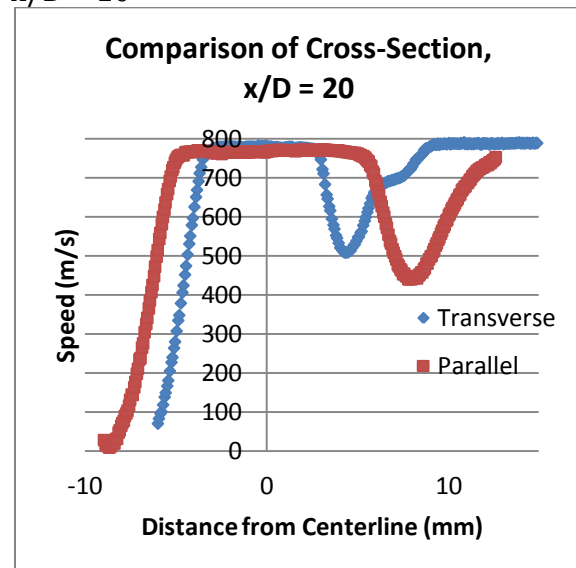an the transverse RCS jet configuration but it also forms a wider jet. The structures of the jets also show similar characteristics with similar slope in the decrease of velocity across the barrel shock on either side of the jet. Since the parallel jet is largely unaffected by the model bow shock, this would indicate that the RCS oblique barrel shock structure remains undisturbed. However, it can be noted that the difference in widths of the two jets is greater on the windward side and continues to increase with distance at a greater rate than it does on the leeward side of the jet. The boundary decreases from 4.72 mm from the centerline at x/D = 10 to 4.49 mm from the centerline at x/D = 20. It appears that the presence of the bow shock inhibits the expansion of the RCS jet.

Just as the bow shock affects the RCS jet, the RCS jet appears to greatly impact the model bow shock structure. In the parallel jet case, the region on the windward side of the jet between the oblique shock and the model bow shock clearly shows two shock profiles with a low velocity region in between. However, in the transverse configuration, it appears that the model bow shock is actually a very thick merged shock with the mixing region between the oblique shock and the model bow. This is especially apparent in the x/D = 5 cross-section, which is near the model and would necessarily have the most interactions with the bow shock as well as the model itself. It can be concluded that the transverse RCS jet more significantly affects flow conditions than the parallel RCS jet, especially close to the model. This strong RCS jet/bow shock interaction results in a different RCS structure, a different bow shock structure and must necessarily include changes to the surface

pressures and forces and moments on the aeroshell surface. This could be responsible for

the change in forces and moments on the MSL vehicle.

CHAPTER TEN

COMPARISONS TO CFD

10.1 Introduction

This chapter focuses on the comparison of the experimental work presented in this research to the computations that were completed using a CFD method at the University of Michigan in the joint research project. Details regarding LeMANS were previously discussed in Chapter One. In this chapter, some details regarding the numerical simulation are given. Then, the qualitative comparison that was made for the RCS parallel jet configuration at a thrust coefficient of 0.5 is presented. Following this, computed results of the RCS transverse and parallel jet configurations at a thrust coefficient are 1.0 are given and compared to the quantitative PLIIF results.

10.2 Numerical Simulation

Three-dimensional numerical simulations were performed using LeMANS, assuming thermo-chemical equilibrium and the results are compared to the experimental data. The

model used in the numerical simulations includes the converging section of the RCS nozzle to better match the experimental setup. The computations were only conducted along half the aeroshell due to the symmetry of model in order to cut down on computational time. The computational grid contains approximately 9 million hexahedral cells, with clustering near the MSL surface and RCS jet [107]

10.3 RCS Parallel Jet Qualitative Comparison at a Thrust Coefficient of 0.5

Figure 10.1 shows Mach number contours on the plane of symmetry as predicted by LeMANS for the parallel RCS jet configuration with a nozzle thrust coefficient equal to 0.5.
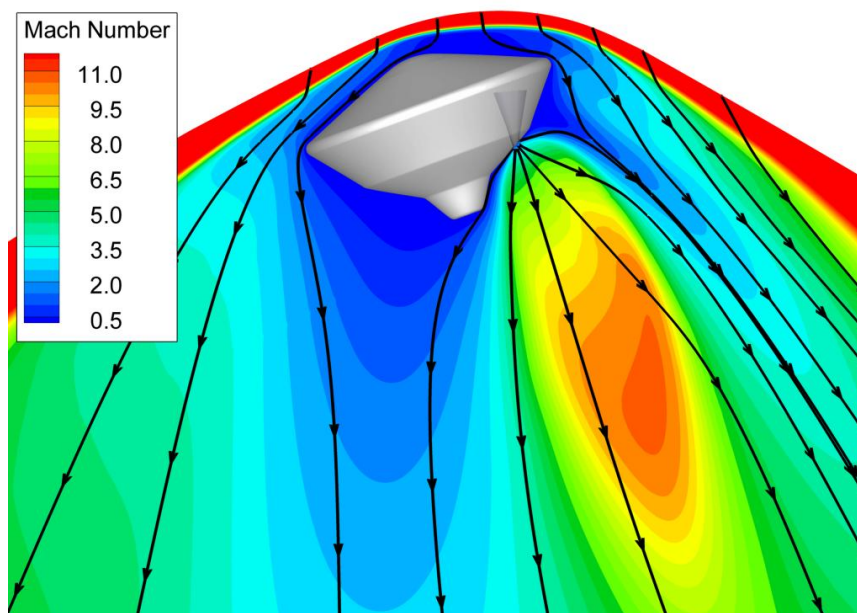

Figure 10.1 Computed Mach numbers for RCS parallel jet configuration with a jet thrust coefficient of 0.5.

The RCS jet expands from sonic conditions at the nozzle exit to supersonic and hypersonic conditions downstream in the wake region. The jet also disturbs most of the wake region

on the windward side, but does not seem to interact with the aeroshell bow shock. The Mach number distribution of the RCS jet is asymmetric in most of the wake region but eventually becomes symmetric at approximately 60 jet-exit diameters from the nozzle. This is the same trend seen in the PLIIF images in Chapter Seven.

Initial qualitative comparisons between the experimental and numerical results are also performed for the RCS jet exiting parallel to the freestream at a thrust coefficient of 0.5. The RCS density distributions, normalized to jet exit conditions, along the jet centerline for the experimental measurements and numerical calculations are presented in 10.2a. This figure shows that the experimental values are not proportional to density in a region near the nozzle exit (0-10 jet-exit diameters). The normalized density values should not increase in an expansion. The reason for this discrepancy is that the diagnostic technique produces results that are not directly proportional to density in the continuum regions of the flowfield near the jet exit, which was described in Chapter Three [49]. Between 10 and 25 jet-exit diameters away from the nozzle, the experimental and numerical results in the rarefied region are in relatively good agreement, with a maximum difference of less than 10%.

Figure 10.2b shows the normalized density values for the two methods in the y-direction across the RCS jet at 15 jet-exit diameters away from the nozzle exit. Near the jet core (-4.5 to +4.5 jet-exit diameters), there is relatively good agreement between the experimental and CFD results, with a maximum difference of 14%. Close to the jet boundary, however, there is a large disagreement between the two methods. CFD predicts higher normalized density values near the jet boundary with differences as large as 120%

compared to the experimental measurements. The reasons for this are that CFD predicts a larger RCS jet width relative to the experimental measurements. Also, the PLIIF signal is not proportional to density in the more continuum regions of the jet boundary. A second comparison can be seen in Figure 10.2c, which shows the normalized density values for the numerical and experimental methods across the RCS jet at 20 jet-exit diameters away from the nozzle exit. The comparison again shows that the differences between the numerical and experimental results are relatively small near the jet core, but increase near the jet boundary.
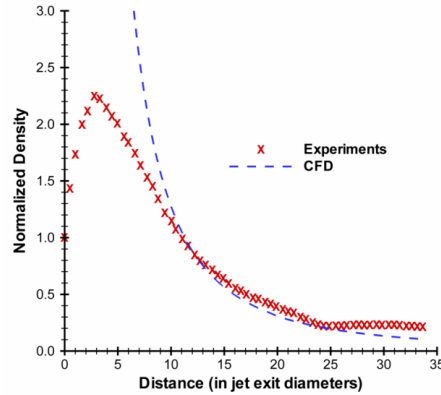
(a) jet centerline
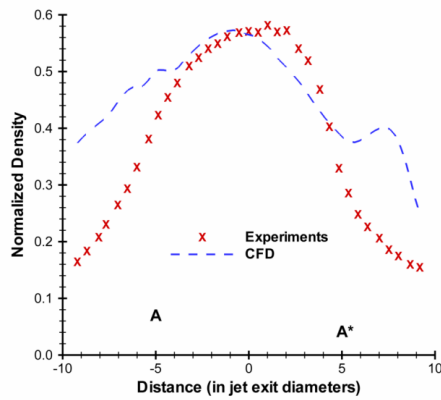
(b) 15 jet exit diameters
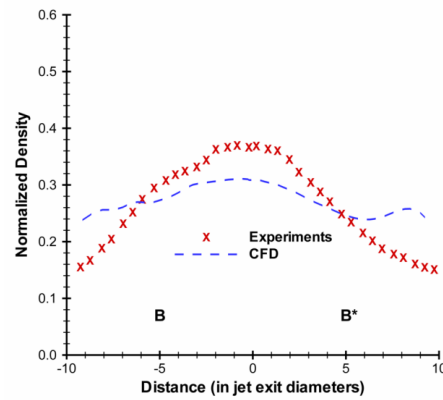
(c) 20 jet exit diameters

Figure 10.2 Normalized density distributions for experimental and numerical results for a 0.5 thrust coefficient with an RCS jet exiting parallel to the freestream: (a) along the jet centerline (b) across the jet at 15 jet-exit diameters (c) across the jet at 20 jet-exit diameters.

Figures 10.3a and 10.3b show density contours on the plane of symmetry from the experimental and numerical methods, respectively. In Figure 10.3a, the image on the left shows experimental PLIIF contours which are proportional to density in the rarefied regions of the flowfield, while the image on the right shows the same results at a different contrast ratio to highlight the density distribution and the fluid structure of the RCS jet. The contour levels in Figure 10.3b for the numerical results show normalized density

values from the calculation. Figure 10.3 shows overall agreement between the two results in regards to the expansion of the jet along the centerline. The bow shock shape around the model in both the PLIIF and the CFD shows good agreement, indicating that there is limited interaction with the freestream test section barrel shock and triple point. The figure also shows that CFD, however, predicts an RCS jet width larger than observed in the experiments and higher density values near the jet exit. These differences in the RCS jet profile between the numerical and experimental methods may be caused by slight differences in the internal nozzle geometry of the MSL model and the RCS nozzles.
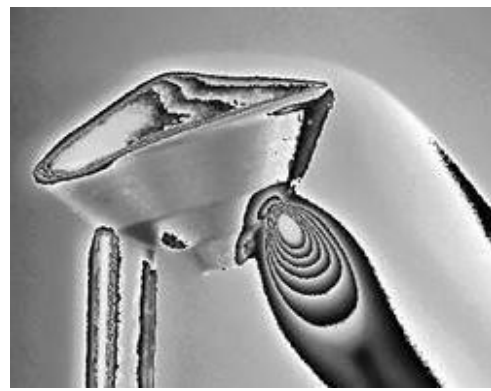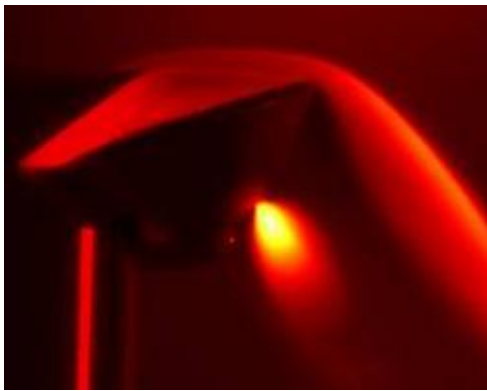
(a) experimental results
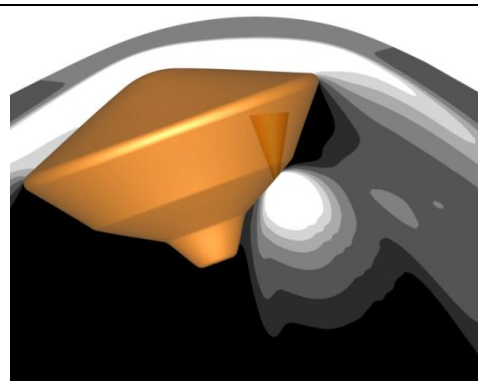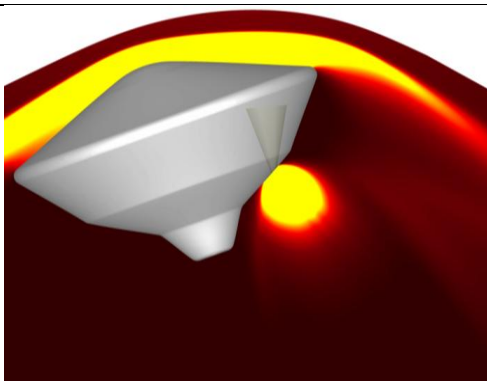
(b) numerical results

Figure 10.3 Flowfield density distribution for parallel RCS jet configuration at a jet thrust coefficient of 0.5: (a) experimental results (b) numerical results

10.4 RCS Transverse Jet Quantitative Comparison at a Thrust Coefficient of 1.0

The velocity contours overlaid with streamlines on the plane of symmetry as predicted by LeMANS for the transverse RCS jet configuration with a nozzle thrust coefficient of 1.0 is shown in figure 10.4. Figures 10.5 and 10.6 show computed temperature contours and Mach number contours, respectively. In all of these figures, the model mounting sting is also shown.
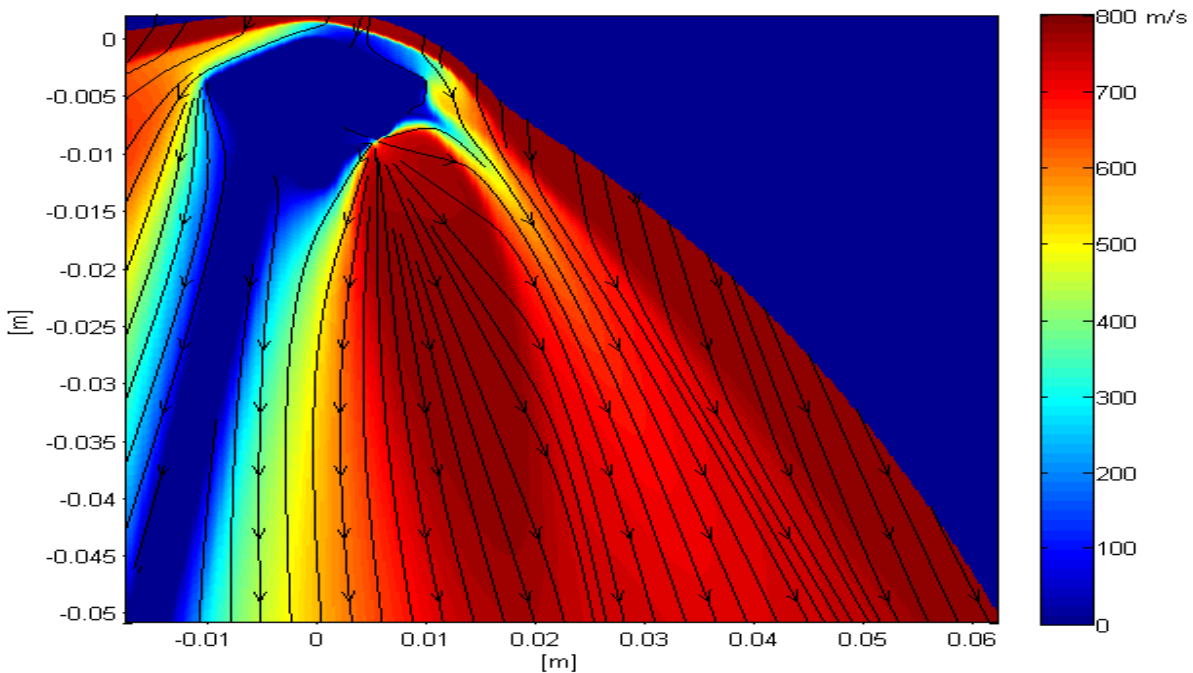
Figure 10.4 Computed velocities for RCS transverse jet configuration with a jet thrust coefficient of 1.0.
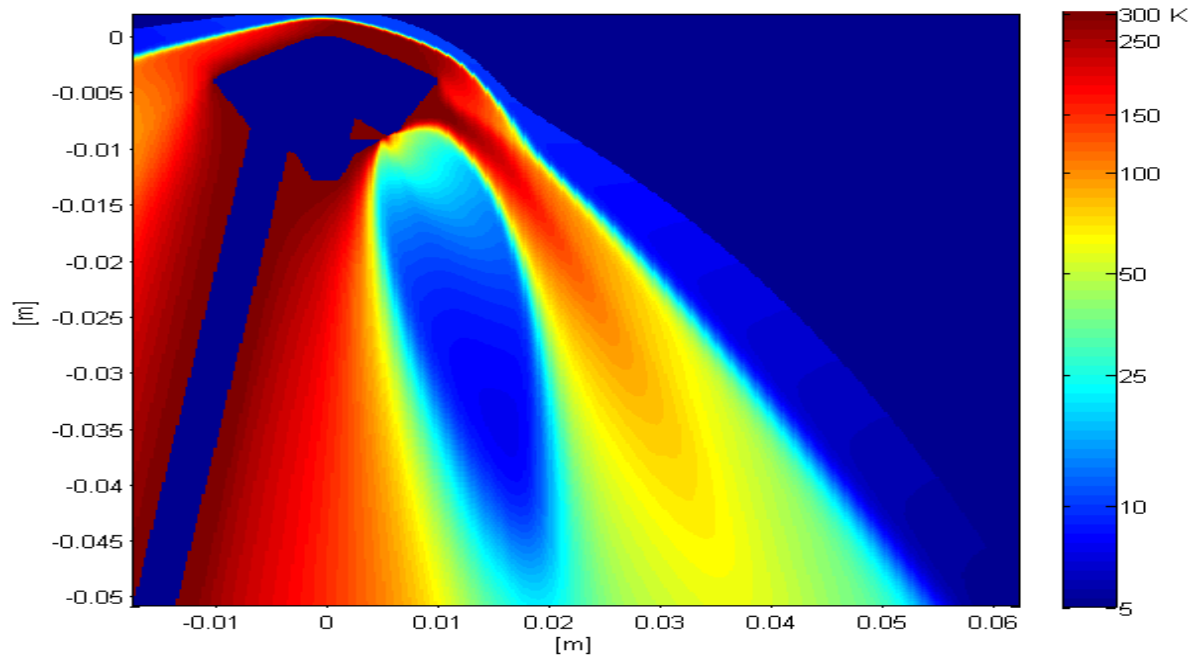
Figure 10.5 Computed temperature contours for RCS transverse jet configuration with a jet thrust coefficient of 1.0.
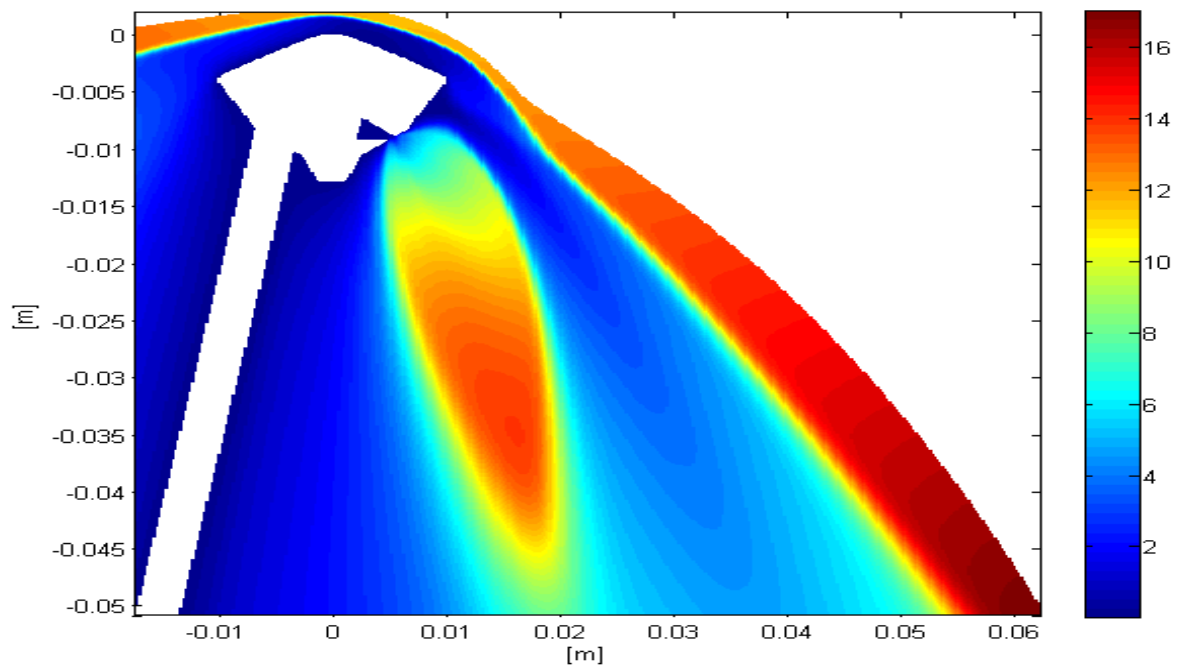
Figure 10.6 Computed Mach numbers for RCS transverse jet configuration with a jet thrust coefficient of 1.0.

As shown in these figures, the RCS jet expands from sonic conditions at the nozzle exit to supersonic and hypersonic conditions downstream in the wake region. The jet disturbs the wake region in the windward side and interacts with the aeroshell bow shock, resulting in turning the RCS jet flow downstream and pushing the aeroshell bow shock farther away from the shoulder. Within the RCS jet core, velocities reach a maximum of 782 m/s. Unlike the PLIIF RCS jet, no shock Mach disk can be seen for the computed RCS jet. Temperatures in the RCS jet fall in a short distance to low temperatures that reach a minimum of 7.9 K. Around the aeroshell and in the leeward wake region, temperatures remain around 300 K. Mach number distribution of the RCS jet is asymmetric in most of the wake region.

The flow features and behavior of the flow is similar to that of the PLIIF results reported in Chapter Eight. In both, a recirculation region near the shoulder of the aeroshell occurs between the RCS jet and the aeroshell bow shock. Farther downstream, between the RCS jet and the model bow shock is a region where velocities are reduced to magnitudes on the order of 400-500 m/s. Temperatures in this mixing region, which are calculated as 100 K, are higher than for the PLIIF quantitative results, which reports temperatures on the order of 75 K.

In order to compare results within the RCS jet structure, the computed velocities and temperatures are plotted with PLIIF results in figures 10.7 and 10.8, respectively. Temperatures are plotted on a semi-log scale.
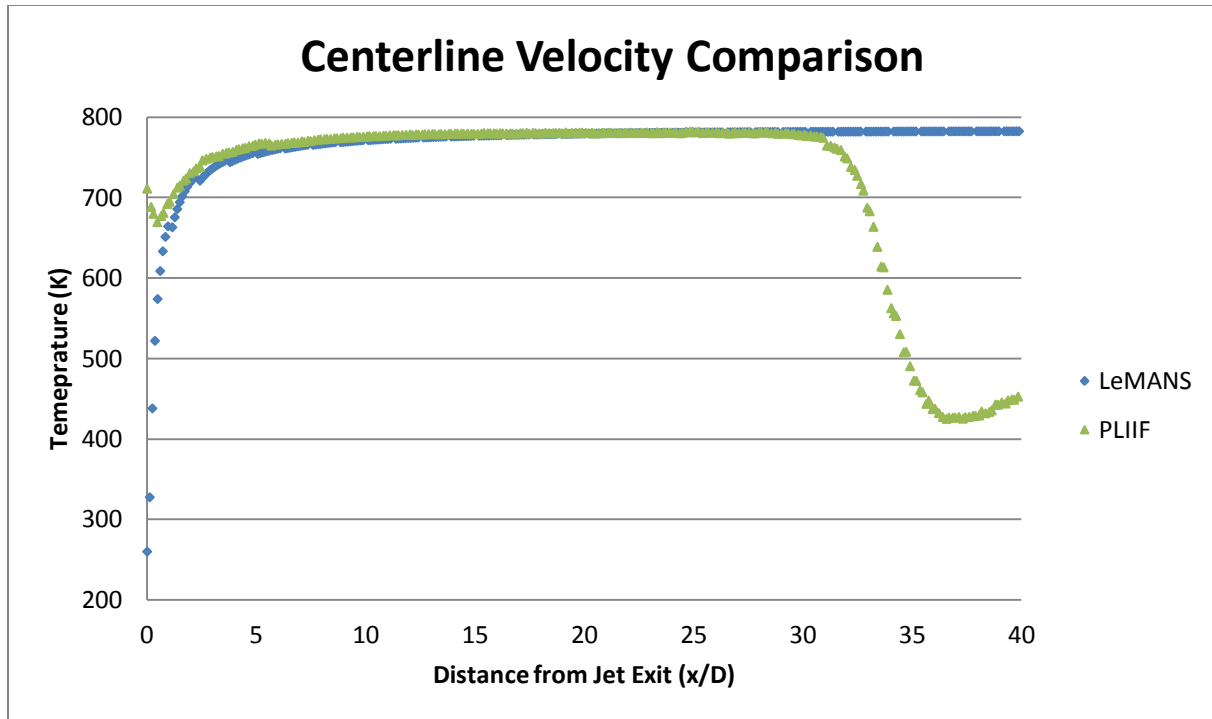
Figure 10.7 Comparison of velocities from LeMANS results and PLIIF data along the RCS transverse jet centerline
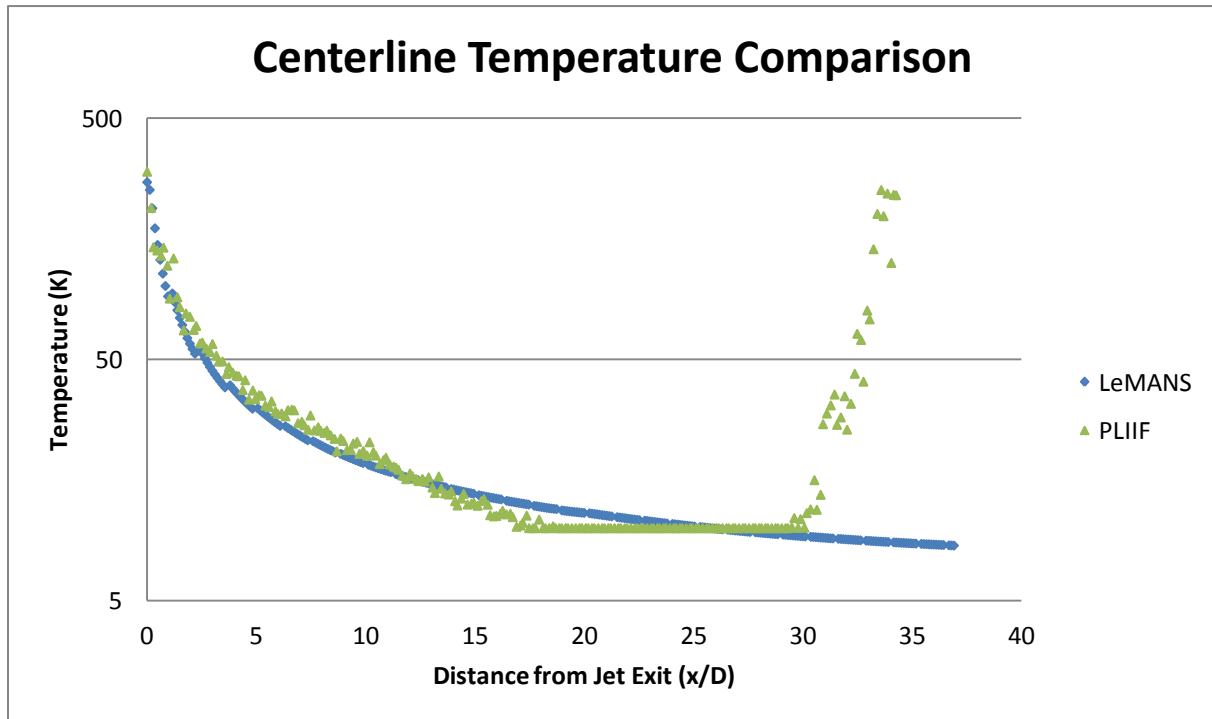
Figure 10.8 Comparison of temperatures from LeMANS results and PLIIF data along the RCS transverse jet centerline

The centerline profiles shown in the figures actually compare more favorably than the PLIIF data does with the Ashkenas and Sherman relationship. For the velocity centerline profile, the shape and magnitudes align closely with an average 5.5 m/s difference (0.8%) throughout the length of the RCS jet, with the exception of no terminating Mach disk in the LeMANS calculation. The temperatures also show similarity with an average 2.3 K (10%) difference throughout the RCS jet. These results show good agreement between the LeMANS computation and the PLIIF measurement, both validating the CFD and the PLIIF measurement for the RCS jets.

The large discrepancy between the two approaches is most apparent, however, upon examining the velocities at cross-sections in the y-direction normal to the RCS transverse jet centerline. In figure 10.9, a plot of the velocity magnitudes of the RCS transverse jet at various cross-sections are shown.
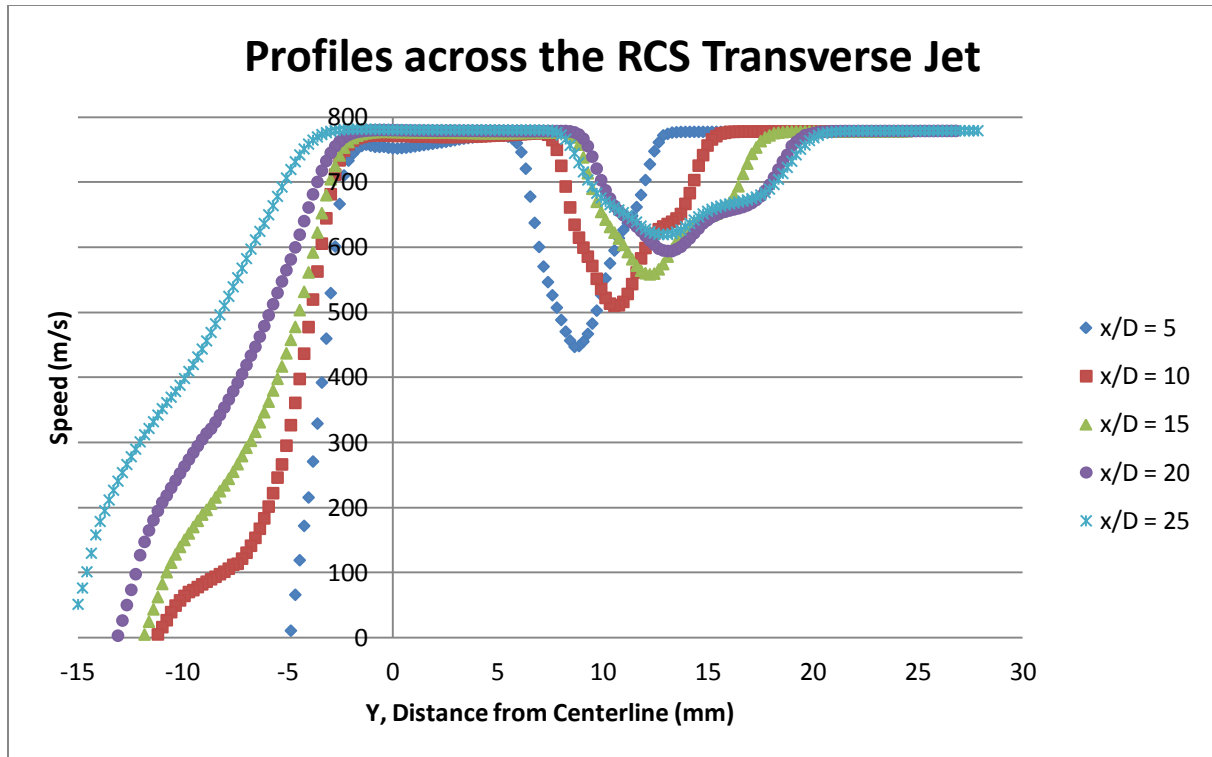
Figure 10.9 Velocity magnitudes at cross-sections normal to RCS transverse jet centerline with a thrust coefficient of 1.0 as computed by LeMANS.

These computed cross-sections show similar behavior to the RCS transverse jet cross-sections from the PLIIF method. In the figure, from negative y-direction to positive y-direction, the following features can be seen: a low velocity region in leeward region of RCS transverse jet, constant velocity region within jet core, drop in velocity across oblique shock and rise in velocity across aeroshell bow shock to freestream. However, it can be seen that the computed aeroshell bow-shock and RCS jet oblique shock interaction occurs at a much greater distance from the centerline than for the PLIIF method (at a distance of 10 mm rather than a PLIIF value of 5 mm from the centerline). This can also be seen in figure 10.10 which shows the profiles of x/D = 5 and x/D = 25 for the two methods.
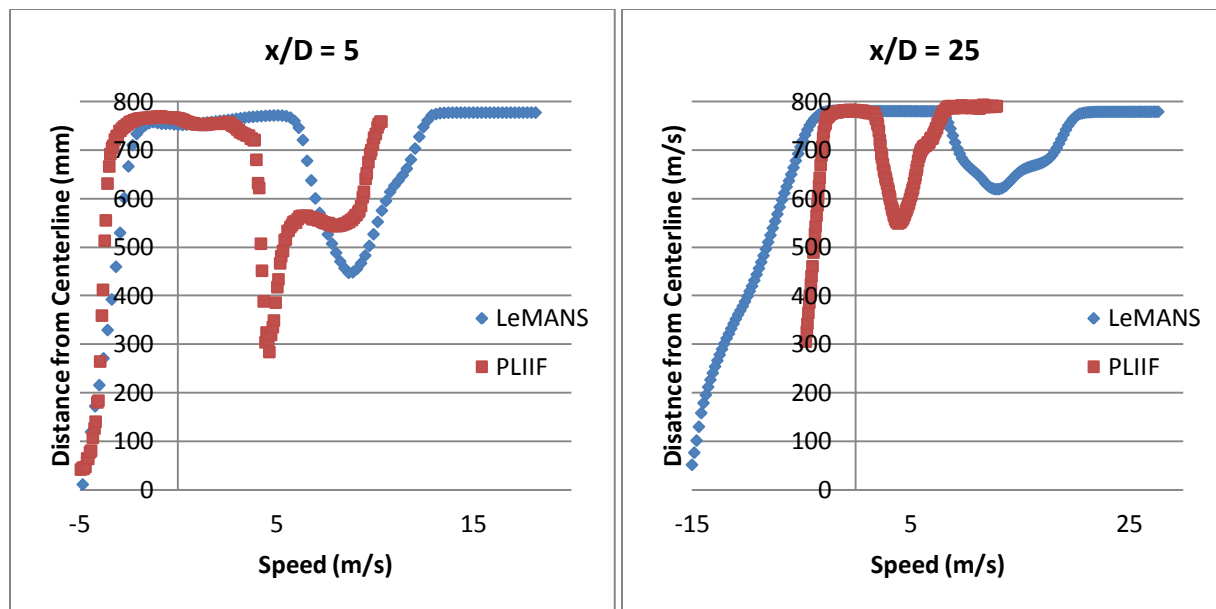
Figure 10.10 Comparisons of profiles of RCS transverse jet

It can be seen that the RCS transverse jet computed using LeMANS predicts a much wider jet shape, with the RCS transverse jet penetrating farther into to the aeroshell bow shock region. Also, the RCS transverse jet does not narrow farther away from the jet exit, which can be explained because the computed RCS transverse jet is not terminating in a Mach disk as the RCS transverse jet does for the PLIIF method. This wider jet structure that does not terminate in a shock is apparent in figure 10.4 but also in the qualitative comparison. It is uncertain why there is such a large discrepancy in RCS jet width. However, it could be a combination of several things. For one, there could be some differences in jet nozzle geometry between the experimental method and the computational method. A second reason could be due to a different calculated back pressure in the CFD than existed for the PLIIF method. The back pressure was not held constant in the LeMANS simulations like it was for the experiments. Also, the freestream

131

test section barrel shock and triple point could have some effect on the conditions in the wake of the experimental method that were not calculated. Overall, there is good agreement between the two approaches.

10.5 RCS Parallel Jet Quantitative Comparison at a Thrust Coefficient of 1.0

Figure 10.11 shows velocity contours overlaid with velocity streamlines on the plane of symmetry as predicted by LeMANS for the parallel RCS jet configuration with a nozzle thrust coefficient equal to 1.0. Figures 10.12 and 10.13 show computed temperature contours and Mach number contours, respectively.
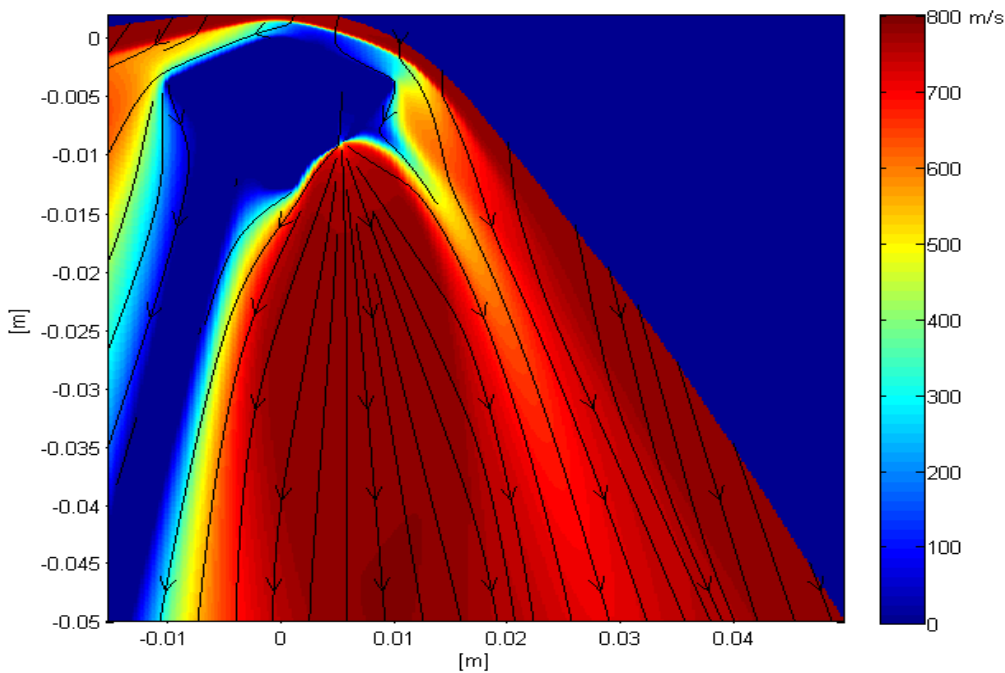
Figure 10.11 Computed velocities for RCS parallel jet configuration with a jet thrust coefficient of 1.0.
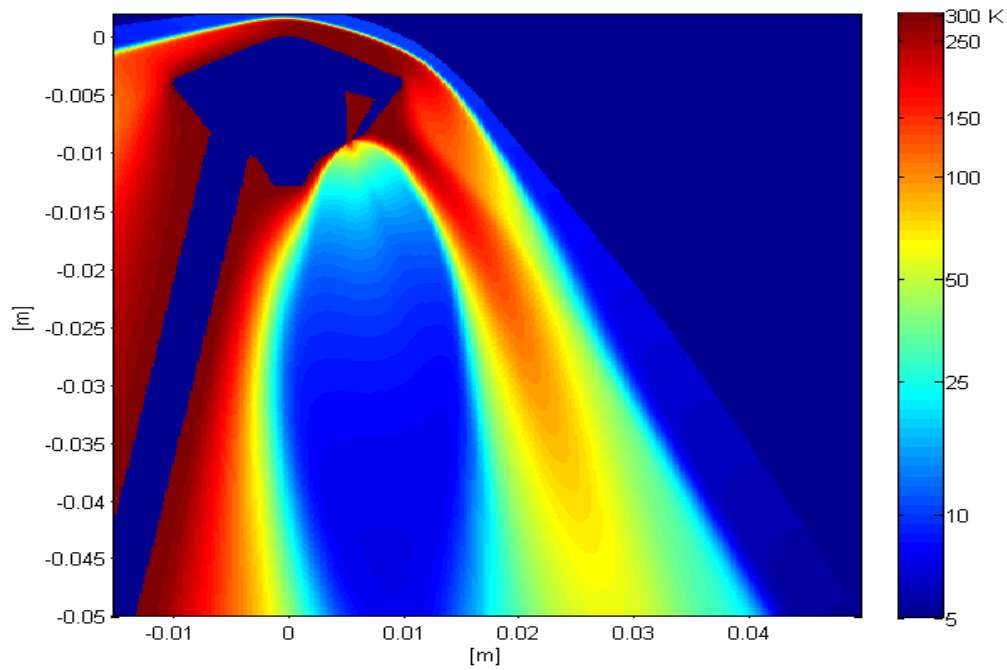
Figure 10.12 Computed temperature contours for RCS parallel jet with a jet thrust coefficient of 1.0.
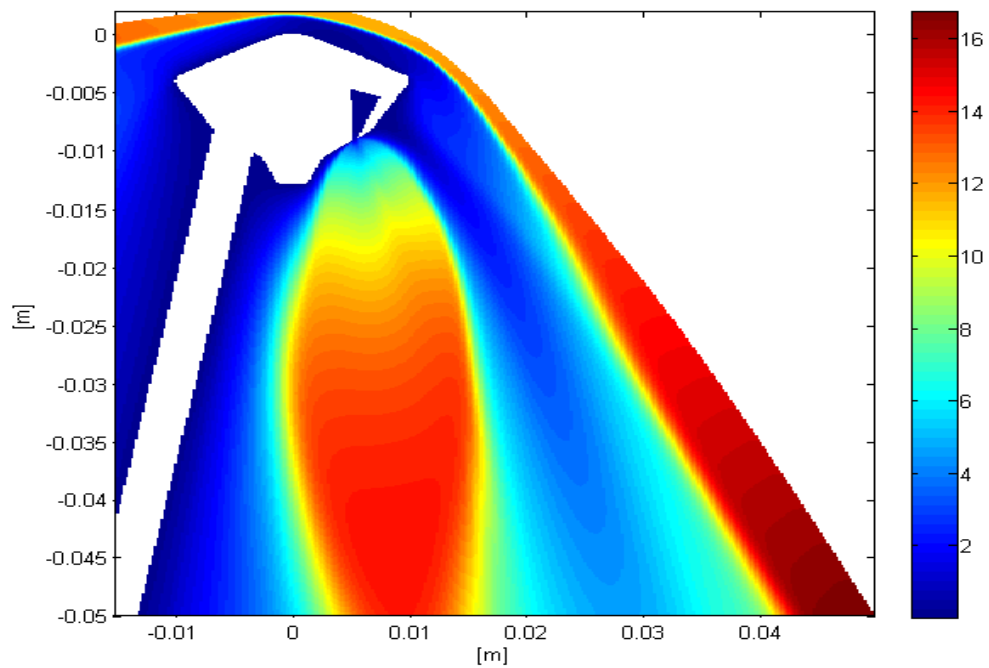
Figure 10.13 Computed Mach numbers for RCS parallel jet with a jet thrust coefficient of 1.0.

The RCS parallel jet expands from sonic conditions at the nozzle exit to supersonic and hypersonic conditions downstream in the wake region. The jet extends almost symmetrically but Mach numbers show asymmetry until 68 jet diameters away from the jet exit. On the windward side of the RCS jet, the RCS jet disturbs much of the wake region but does not appear to affect the aeroshell bow shock. Like with the RCS transverse jet results, the RCS jet structure itself does not appear to terminate in a Mach disk but velocities continue to increase farther away from the jet exit until the edge of the computed region is reached. At this distance (82 jet diameters away from the jet exit), velocity has reached a magnitude of 787 m/s. Temperatures in the RCS parallel jet decrease quickly from 300 K as the flow moves away from the jet exit, down to a calculated minimum temperature of 7.5 K before the edge of the computed region is reached.

The flow features, like with the RCS transverse case, show strong similarity to the PLIIF data. A separation region appears at the shoulder of the aeroshell between the RCS jet and the bow shock. This separation region is larger than was seen in the RCS transverse case. Downstream of this separation region, there is a region between the RCS jet and the bow shock where velocities are reduced only slightly from the velocities in the freestream or in the RCS jet core. These velocities on the order of 650 m/s are much higher than the 400 m/s reported for the PLIIF case. Temperatures in this region though give similar results (around 150 K). In order to compare results within the RCS jet structure, the computed velocities and temperatures are plotted with PLIIF results in figures 10.14 and 10.15, respectively. Temperatures are plotted on a semi-log scale.
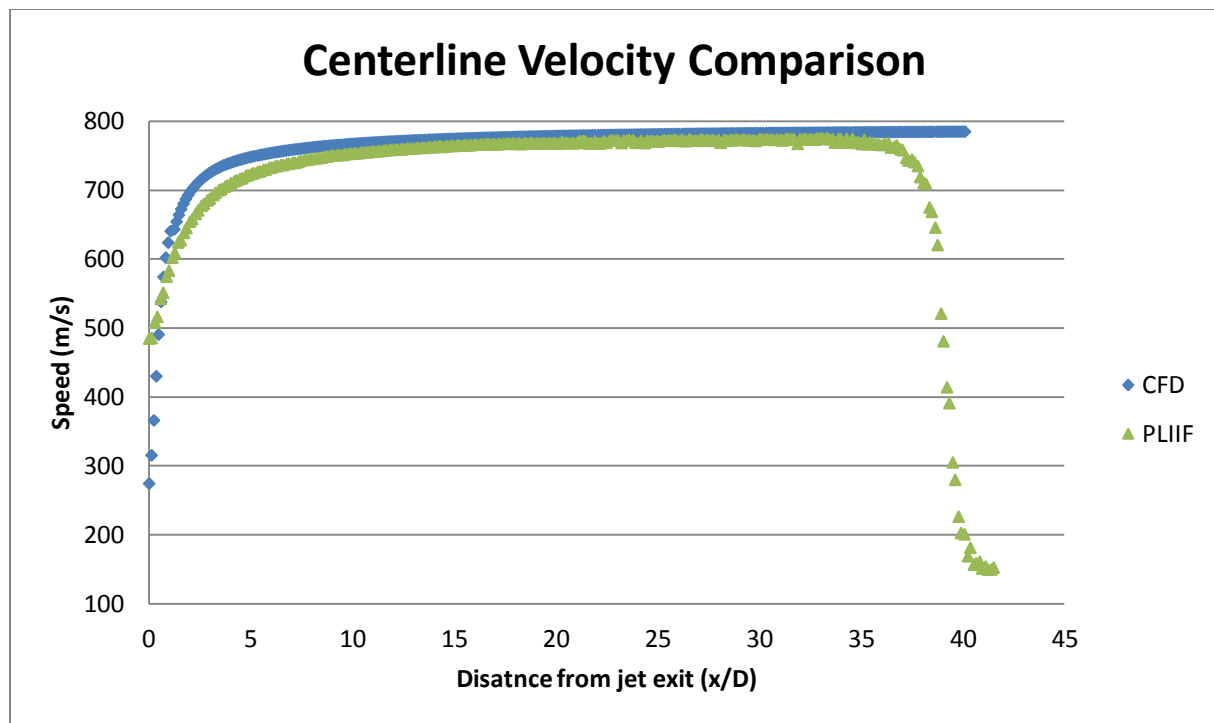
Figure 10.14 Comparison of velocities from LeMANS results and PLIIF data along the RCS parallel jet centerline with a jet thrust coefficient of 1.0.
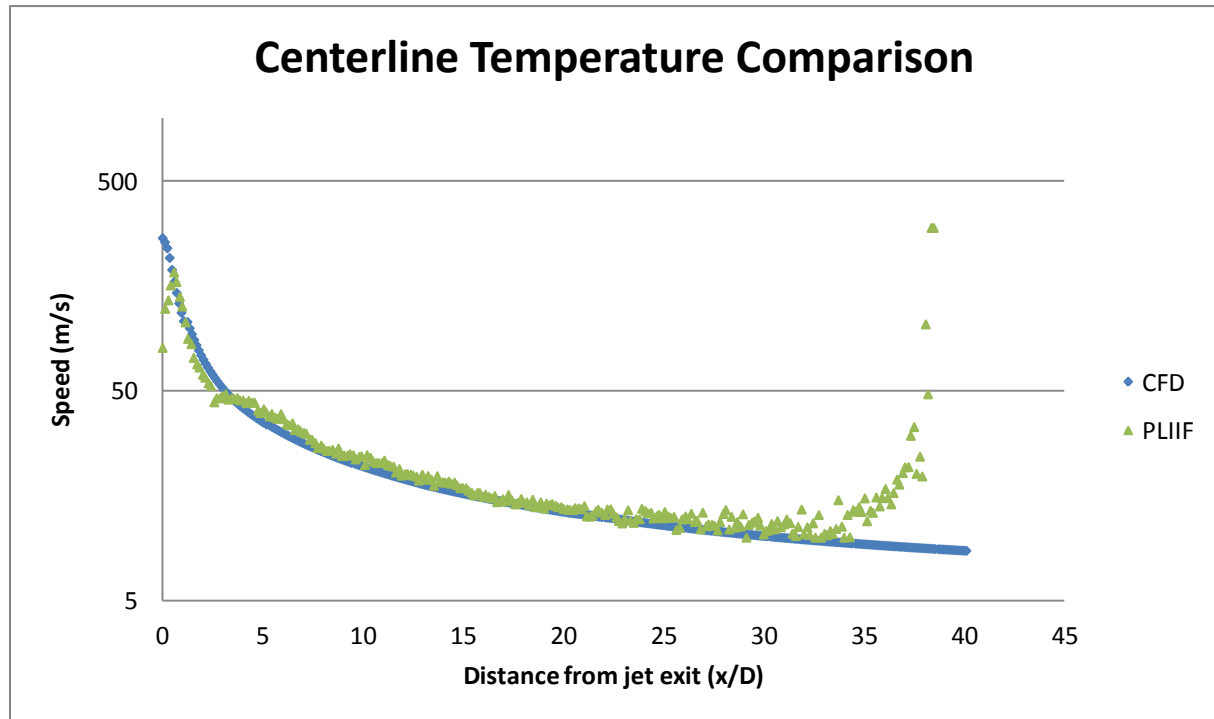
Figure 10.15 Comparison of temperatures from LeMANS results and PLIIF data along the RCS transverse jet centerline with a jet thrust coefficient of 1.0.

The velocity and temperatures along the centerline show good agreement between the two methods. Throughout the jet, there is an average difference of 15 m/s (2.3 %) in velocity and a difference of 3.4 K (10%) in temperature. As with the RCS transverse comparison, though, the largest discrepancy between the two approaches is the difference in RCS jet size. Again, this could be due to a combination of back pressure differences, freestream test section barrel shock and triple point interactions or differences in the jet nozzle geometries between the two methods.

The velocity magnitudes of cross-section normal to the centerline at various distances from the jet exit are shown in figure 10.16.
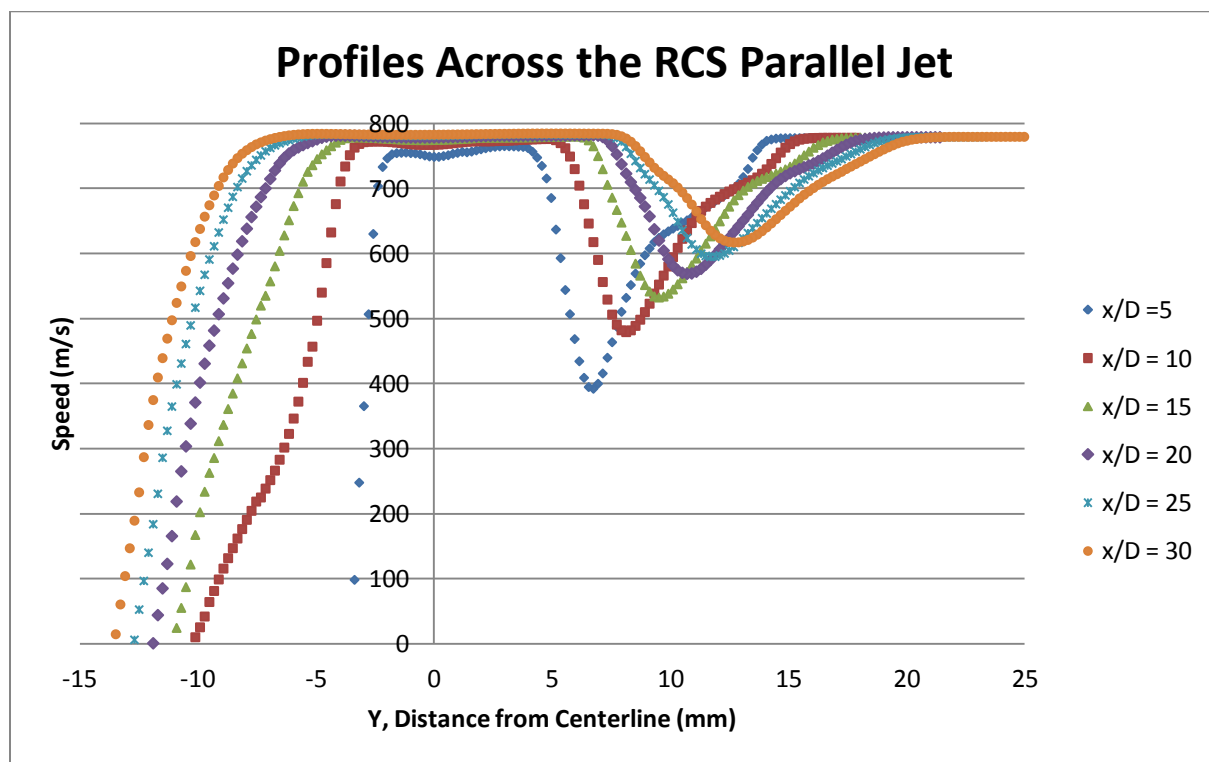
Figure 10.16 Velocity magnitudes at cross-sections normal to RCS parallel jet centerline with a thrust coefficient of 1.0 as computed by LeMANS.

The figure shows two regions of constant velocity – across the RCS jet and in the freestream. At cross-sections farther from the jet exit, the computed RCS jet continues to widen without any narrowing. This is different from the RCS parallel jet obtained using PLIIF, in which the jet narrows before terminating in a Mach disk. However, although there is this difference in the structure of the RCS jet, the actual width and size are comparable.

Figure 10.17 shows the profiles of velocity magnitudes at cross-sections of x/D = 5 and x/D = 10, respectively, for the two methods.
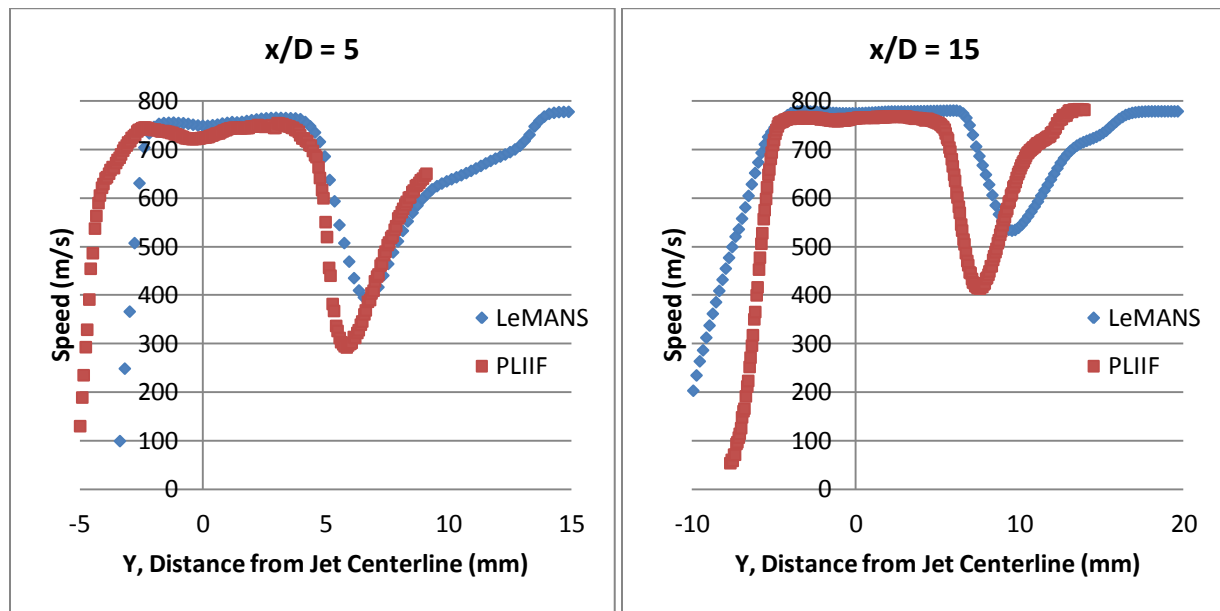
Figure 10.17 Comparisons of profiles of RCS parallel jet

At x/D = 5, the two jet profiles line up quite well with only some variation in the leeward region oblique shock. At x/D = 15, the jet computed using LeMANS is wider than the RCS jet from PLIIF but the behavior in the profile though the shocks are similar. Thus, for the parallel jet, although the LeMANS method does not compute a terminating shock for the

RCS jet, the jets actually show good similarity in structure and size. For the RCS parallel jet, there is good agreement between the two approaches.

Due to the good similarity in flow properties and features, as well as quantitative values, it can be deduced that the LeMANS method provides generally good results.

10.6 RCS Control Gain Analysis

Because the CFD computations are able to calculate surface pressures, it can analyze the forces and moments on the aeroshell caused by the firing of the RCS jets. In order to determine the effectiveness of control by the RCS jet, the control gain can be analyzed [111]. Control gain is defined as [110]:

$$Gain = \frac{C_{M_{thrust}} + C_{M_{Inteference}}}{C_{M_{thrust}}}$$

(10.1)

in which $C_{Mthrust}$ is coefficient of the moment caused by the thrust of the jet and $C_{Minterference}$ is the coefficient of the moment caused by the aerodynamics interference caused by the RCS jet (versus the no jet firing scenario). Ideally, this number is one, indicating the thrust performs as expected. Alkandry found that the parallel RCS jet does indeed have a control gain of 1.0, indicating ideal control effectiveness but that the transverse jet resulted in a control deficit [107, 110]. For the parallel jet, the axial and normal components of thrust contribute to a net positive moment of thrust but the transverse produces one component with a positive moment and one with a negative moment, resulting in a net reduced moment from thrust, with respect to the center of gravity. Plus, the parallel jet had a longer moment arm than the transverse jet so that the parallel jet had a more effective thrust moment [110]. Another reason the transverse jet has reduced control gain is due to the higher interference moment than the parallel jet, which augments pressures on the surface

of the aeroshell, creating counteracting moments in the wake region [107, 110]. At higher thrust coefficients for the transverse jet, the counteracting moments cancel each other more than at lower thrust coefficients, resulting in an improvement in control. Selecting an orientation that allows for thrust components to act in the same direction, and carefully designing a jet that induces few fluid interactions, or produces counteracting effects to result in small interference is recommended [110].

CHAPTER ELEVEN

CONCLUSION

11.1 Introduction

In this chapter, a summary of the important conclusions from each chapter is presented. The chapter also provides recommendations for future research.

11.2 Summary

In Chapter 1, it was asserted that a good fundamental understanding of RCS jets is necessary in order to help improve the landing accuracy that is necessary for future manned, missions to Mars. A discussion of the value of joint experimental and computational investigation was given. This chapter concluded with research aims: to determine experimental parameters for the study of the fundamental aerodynamics of RCS jets, to obtain high-quality qualitative and quantitative flowfield data for two – transverse and parallel – RCS jet configurations using the PLIIF method, and to compare these results to LeMANS/CFD calculations completed at the University of Michigan.

Chapter Two discusses relevant research and found that, while RCS jet aerodynamics have been studied for several decades, no experimental study completed using a non-intrusive method for blunt bodies has resulted in quantitative velocity and temperature flowfield measurements.

Chapter Three gives the theory of laser-induced fluorescence as well as the principles utilized to obtain spatially-resolved qualitative images and quantitative temperature and velocity flowfield measurements. The temperature was reported to have an error of less than 10% and a velocity error of less than 6% for hypersonic conditions.

In Chapter Four, the experimental facilities are explained. Using a low-pressure chamber and the Ashkenas and Sherman relationship, which characterizes underexpanded jets in low-density wind tunnels, it is possible to place the model in a freestream at a specified Mach number. For this research, a freestream Mach number of 12 was chosen.

The discussion in Chapter Five focuses on designing the experiment to allow for good comparisons between the CFD calculations and the experimental measurements. Minimizing the interactions from the freestream test section barrel shock and triple point is necessary in order to have meaningful data for comparison to CFD. Therefore, a parametric study was conducted to investigate this interaction. Based on this study, a 2 cm diameter MSL model was designed and placed in a Mach 12 freestream at a 20 degree angle of attack. Two RCS jet configurations, which were located at the same location on the model and had the same jet exit sonic conditions, were chosen for investigation. These two configurations consisted of a jet issuing parallel to the freestream and a jet issuing transverse to the freestream and simulated the different firing directions used on Mars

landers. The qualitative experiments would obtain images for thrust coefficients between 0.5 and 3.0 in increments of 0.5. The quantitative experiments would focus on the study of the RCS jet interactions at a thrust coefficient of 1.0 for both configurations.

Chapter Six outlines the data acquisition system and data analysis methods used for the PLIIF experimental technique.

In Chapter Seven, qualitative images were shown and discussed for both the parallel and transverse jet configurations. In examining these images, it was concluded that the transverse jet had a much greater interaction with the model bow shock than did the parallel jet configuration. This interaction likely affects aeroshell surface properties and can likely induce desirable and undesirable forces and moments.

In Chapter Eight, the quantitative planar velocity and temperature measurements were reported for the RCS transverse jet configuration at a thrust coefficient of 1.0. Measurements were compared to the Ashkenas and Sherman relationship [103] and isentropic conditions. Good agreement was found between them.

Chapter Nine reports the quantitative planar velocity and temperature measurements for the RCS parallel jet configuration at a thrust coefficient of 1.0. Good agreement was found between the Ashkenas and Sherman relationship and the isentropic conditions using the Ashkenas and Sherman relationship [103]. In this chapter, the parallel and transverse jet structures were compared. It was concluded that the transverse jet had a larger interaction with the model bow shock than the parallel jet had with the bow shock. This interaction resulted in a model bow shock that was pushed away from the model and also resulted in a smaller RCS jet expansion width and length.   In both RCS jet

configurations, recirculation regions at low velocities and high temperature indicated regions on the aeroshell for total temperature recovery and thus regions of localized heating on the actual MSL.

Chapter Ten compares the experimental and CFD qualitative results of the parallel jet configuration at a thrust coefficient of 0.5 and the quantitative measurements for both jet configurations at a thrust coefficient of 1.0. Overall good agreement was found between the PLIIF measurements and the calculated LeMANS data. The bow shock structure around the model showed good similarity, indicating little interaction of the test section barrel shock and triple point, per the experiment design. The computed RCS jet width and length for both configurations was much greater than what was shown for the PLIIF method. Also, there was no calculated terminating Mach disk shown in either configuration, as appeared in the PLIIF data. It is uncertain why this is the case but is likely due to variations in the wake region back pressure conditions. Once the data was compared and the CFD approach validated, the computations for surface pressure and forces on the aeroshell induced by the RCS jet/bow shock interactions were examined [107, 110]. It was found that the control gain for the parallel jet configuration is close to ideal conditions for effective RCS control and the control gain for the transverse jet configuration results in diminished RCS control [107, 110].

11.3 Future Work

This dissertation provided spatially-resolved planar velocity and temperature flowfield measurements for two configurations of the RCS jets in a Mach 12 freestream.

143

Such measurements have not previously been possible and are due to the unique capability for the PLIIF technique in mixed continuum/rarefied flows. Further, this experimental research provides a comparison to CFD computations that were made by establishing common conditions for a meaningful comparative analysis. However, there are still research directions that can still be undertaken. For one, the RCS jet thrust coefficients used in this experiment were much higher than those used for the actual Mars landers. However, obtaining such a low jet thrust coefficient is not possible given the pressure ranges available in the experimental setup. It would be valuable to obtain, at the very least, quantitative experimental data for a thrust coefficient of 0.5 for both jet configurations. Most advantageous would be to create an experimental setup and design that would allow for low jet thrust coefficients to better understand RCS aerodynamics pertinent to realistic devices.

It would be very useful to add more fidelity to the spectral model and use more frequency resolution for the fitting program to solve. The laser profile has access to three large blended transitions, one of which was not used in this research. Expanding the spectral model to include more transitions as well as hyperfine regions could give more frequency resolution for the fitting model to use to determine temperature and pressure. Including a third blended transition is advantageous because it is near the P13/R15 peak (within 2 GHz).

A third area of future research that may be undertaken is to investigate and understand the discrepancy of the computed RCS jet width and length with the

experimental results. It is unclear exactly why this occurs and would be important in better understanding the fundamental aerodynamics of the flowfield.

Appendix A

Error and Uncertainty Analysis

A.1 Introduction

As stated throughout the dissertation, the velocity measurement is highly dependent on accurate temperature and pressure measurements. It is important to understand how accurate the temperature and pressure measurements are as well as their effect on the accuracy of the velocity measurement due to the calculation of the impact shift. This appendix focuses on an error analysis in the following steps: identification of systematic error, characterization of error in the collected data, sensitivity analysis of the fitted program, as well as calculation of overall uncertainty for temperature, pressure and velocity.

A.2 Identification of Error

Due to the complicated setup of the PLIIF measurement, there can potentially be numerous sources of systematic error. These errors are reduced as much as possible through careful experimental set-up and through monitoring and adjustment throughout

146

the experiment run time. The nature of the experiment itself relies only on the information at one pixel at multiple laser frequencies to construct a spectrum from which to determine the velocity, temperature and pressure properties. Errors which cause different pixels to behave differently - differences in sensitivity across the CCD, stray light reflections, laser sheet intensity variation, etc. - are accounted for in background subtraction and normalization and are made negligible. However, there are still some sources of error that can affect the planar flowfield measurements as a whole. One source of systematic error includes misalignment of the laser sheet on the model jet exit. Another can include the miscalculation of the two laser propagation angles which contribute to the measurement of velocity. There is also some error due to the fitting program's ability to resolve spectra. And another is the contribution of noise in the data that introduces error into the spectral calculation. Each of these will be discussed in turn.

A.3 Fitting Program Error

One of the first considerations in the error analysis is how well the fitting program can resolve the iodine spectral model. The iodine spectral model is very complicated and has many points of local minima that can result in miscalculation of properties. Previous students had used various other techniques and programs but for this body of work, a global solver was used [21,49, 109]. This global solver is designed to detect and avoid local minima and come up with a best global fit of the data.

To determine the ability of the model to handle frequency shifts in the spectra, data was generated from the theoretical model, perturbed in frequency, and fed into the solver.

Because the width of the peaks in the iodine spectrum is broaden in continuum regions and narrow in more rarefied regions of the flow, spectra at Mach 1, 2, 5, 8 and 10 were generated with the 50 MHz frequency step size of the experiment. These idealized spectra were then perturbed by introducing a frequency shift of 1.0 GHz, 0.5 GHz, 100 MHz, 50 MHz, 10 MHz, 5 MH and 1 MHz. The spectra were put into the solver to resolve the spectra and solve for pressure, temperature, and frequency in order to determine how small a resolution the program could resolve. In all Mach flows and for all the perturbations, the program was able to resolve the frequency down to the 0.5 MHz frequency which is only 1% of the frequency step size. Thus, the contribution to error from the fitting program alone is negligible. This gave confidence that the program could resolve the peak at high resolution at many Mach numbers and frequency shifts.

A.4 Characterization of Error

Within the fluorescence signal collected, there is some amount of error. Determining what portion of that data is signal and what is noise is important in order to determine how much error of the properties is due to the noise within the measured spectra. By characterizing the noise within the data, spectra with this noise can be generated and then input into the error solver to perform a sensitivity analysis. From this, the amount of error in the measured parameters is due to the noise in the signal can be determined.

Examining several spectra in each data set, there was no evidence of wavelength-correlated noise, but localized white noise did appear to be present. White noise can in

general have both an additive and multiplicative element. Additive noise can result from random background radiation and other sources external to the model; multiplicative noise can result from variations in laser strength, vibrations of the geometry, or other sources internal to the experiment. Because noise between distinct exposures is not correlated, it can be effectively isolated via a high-pass filter. It is possible that the experimental data contains high frequency components in addition to the noise. Thus a Fast Fourier Transform was applied to the data in order to examine it for high frequency content. For data that showed hyperfine structure, these frequencies showed up in the transform results but not so for the broadened peaks that exist in the continuum region.

The median of the amplitude of the high frequency components was calculated to determine the vertical (additive) element of the noise. This bias was subtracted from the high frequency information and then the data was normalized to determine the multiplicative element of the noise. Across the data, the multiplicative amplitude of high-frequency data was approximately 1.5% times the signal amplitude. For three of the data sets examined, the vertical shift from noise occurred on the order of 0.75% of the maximum signal amplitude. However, for one set of data, the vertical shift was much higher near the jet exit (about 3% of the maximum signal level) before noise dropped off to a 0.75% level farther away from the jet. It is unknown why this one data set had a higher contribution of noise in the region near the jet exit. This could be due to some perturbation in the flow, vibrations of the geometry, or could also be caused by the increased spatial sensitivity near the jet exit. A characteristic image of each data set and the calculated amplitudes of the vertical shift of the noise are shown in the figures A1 – A4.
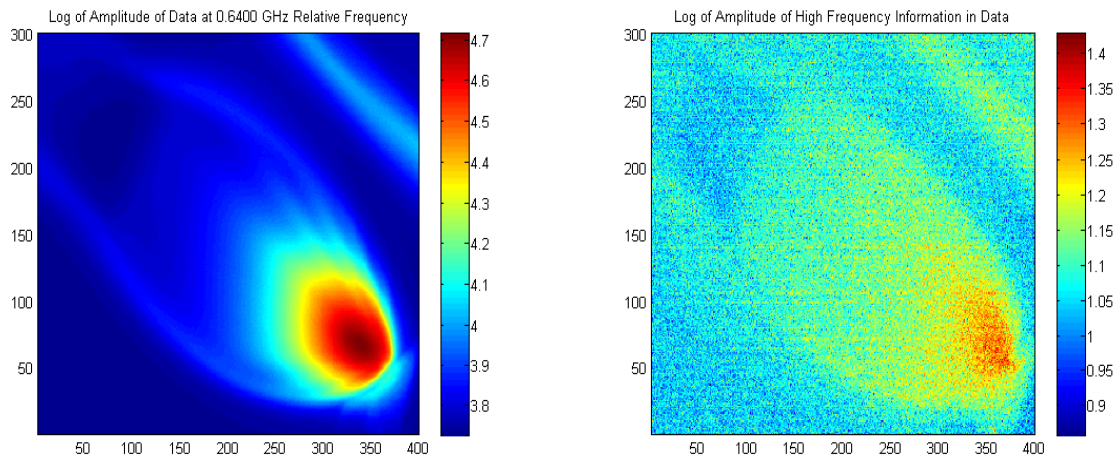
Figure A.1 RCS parallel jet data with additive error of 0.75% of signal
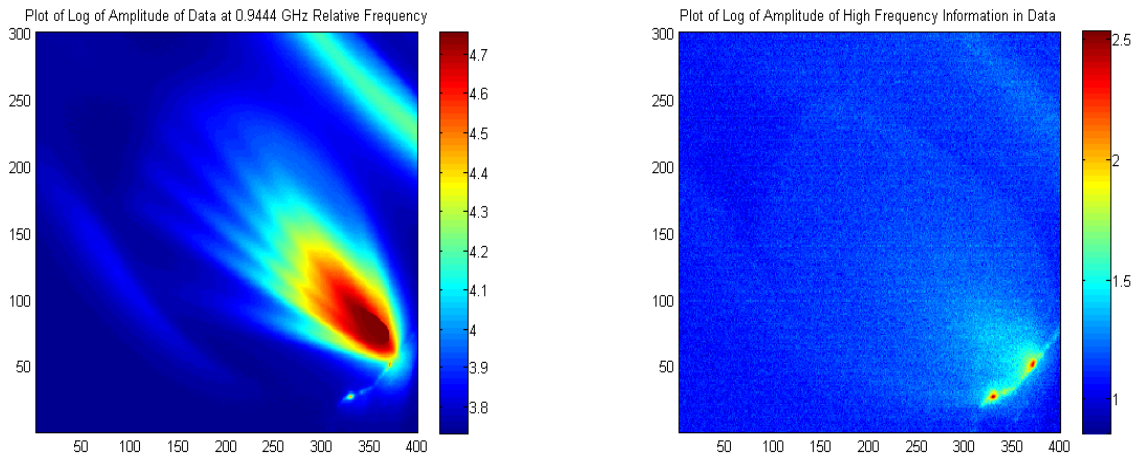
Figure A.2 RCS parallel jet data with additive error of 3% of signal
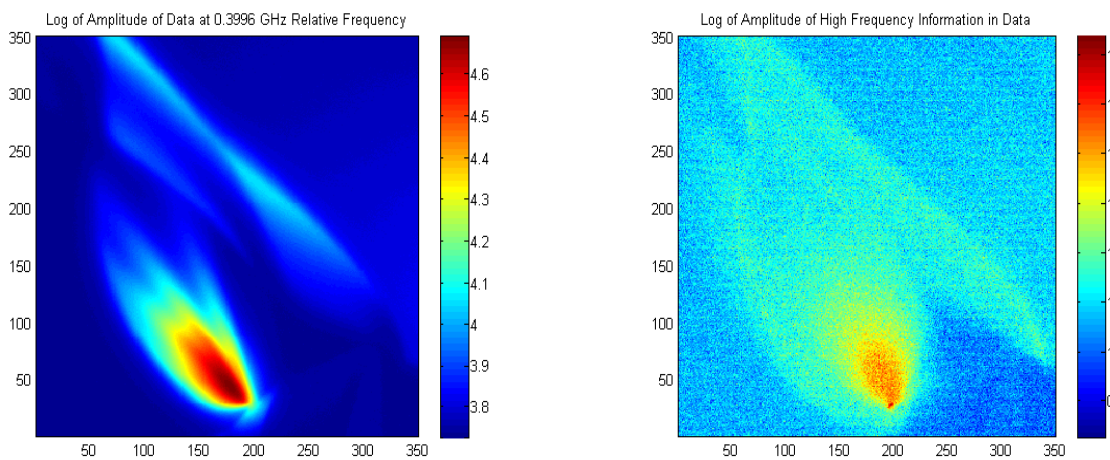
Figure A.3 RCS transverse jet data with additive error of 0.75% of signal

150
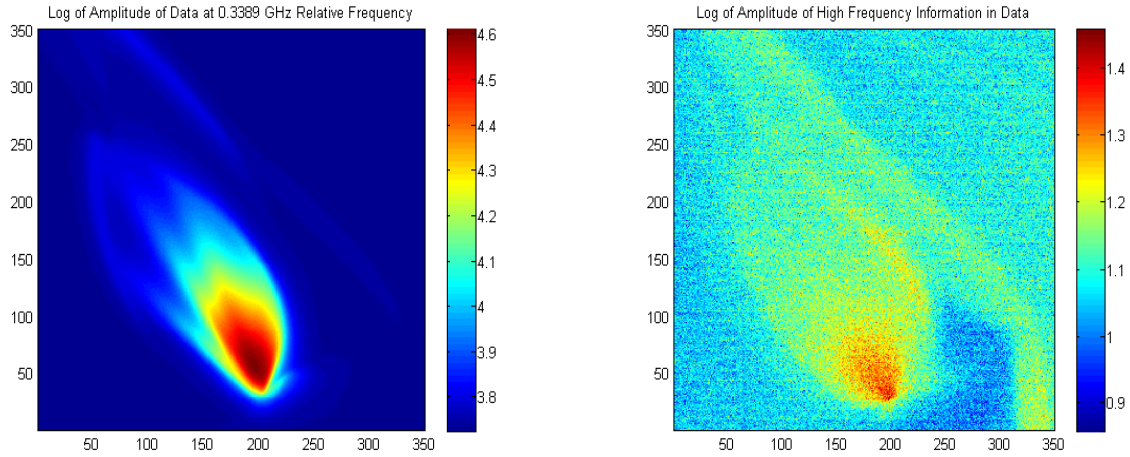
Figure A.4 RCS transverse jet data with additive error of 0.75% of signal

A.5 Sensitivity Analysis

Once the data was characterized, the next step was to determine how the fitting program would determine pressure, temperature, and velocity given a noisy spectrum. Based on the noise analysis in the previous section, spectra at Mach 1, 2, 5, 8 and 10 conditions were subjected to a 1% additive noise component and a 1.5% multiplicative noise component. For the unusually noisy run, a 3% additive noise effect was also analyzed. Thirty different noisy data sets were generated for each of several different Mach numbers; each was input into the fitting program to solve for pressure, temperature and shift. Uncertainty was solved for by calculating the standard deviation of the resulting fitted temperatures and pressures.

Computed standard deviations are summarized in the table.

Table A.1 Uncertainty Results from Sensitivity Analysis

Sensitivity Analysis and Noise Uncertainty						
Mach Number	Temperature (K)		Pressure (atm)		Shift (GHz)	
	1% noise	3% noise	1% noise	3% noise	1% noise	3% noise
1	68	130	0.091	0.19	0.0020	0.0033
2	33	53	0.092	0.13	0.0019	0.0058
5	5.0	9.2	0.023	0.029	0.0014	0.0027
8	1.9	3.6	0.010	0.018	0.0014	0.0031
10	0.80	1.7	0.0068	0.012	0.0011	0.0029

This gives the uncertainty in the flowfield property measurements from the noise in the data sets. Uncertainty for temperature is quite high but decreases significantly in magnitude with increasing Mach number. Uncertainty for pressure likewise decreases in magnitude with increasing Mach number. This is because the sharper features in the iodine spectrum at lower pressures and temperatures are fit more accurately.

A.6 Laser Misalignment Uncertainty

One potential source of errors can be introduced if the laser sheet is not perfectly aligned with the flow. There can be two types of misalignment, linear misalignment and angular misalignment. Linear misalignment occurs when the laser sheet is shifted horizontally to the side of the jet exit. Angular misalignment occurs when the laser sheet is not perpendicular to the jet exit and introduces error when calculating the velocity components.

Linear misalignment could mean that flow streamlines pass into and out of the laser sheet and hence into and out of the images captured. This provides error since the velocity

in the laser sheet plane was assumed to not have an out-of-plane component. The laser

sheet has a thickness of 0.264 mm on the jet exit. This is approximately half a jet diameter

thick. With a misalignment uncertainty of half a jet diameter to either side, linear

misalignment is not expected to have a major contribution to the error.

Regarding angular misalignment, if the laser and flow are misaligned by 3°, because

the laser sheet is 0.264 mm thick an in-plane streamline would enter the image in one pixel

and exit it 78.5 pixels later. This is at least 10 jet diameters in length. This distance is long

enough to be out of the more spatially sensitive region near the jet exit (which extends to

about 3 jet diameters away from the jet exit). At the greater distances than this from the jet

exit, adjacent streamlines exhibit similar velocity, pressure and temperature and the actual

meaningful range is assumed to be considerably longer than 78.5 pixels.

Thus, laser sheet alignment is not considered to be a major source of error in this

work.

A.7 Impact Shift Uncertainty

Impact shift, based on temperature and pressures, has an effect on the calculation of

velocity. The overall uncertainty due to impact shift, S_{impact} can be calculated from the

following equation

$$S_{impact} = \sqrt{\left(\frac{\partial \Delta v_I}{\partial p}\right)^2 (S_p)^2 + \left(\frac{\partial \Delta v_I}{\partial T}\right)^2 (S_T)^2}$$ (A1)

in which Δv_I is the impact shift, and S_p and S_T are the uncertainty in pressure and uncertainty in temperature, respectively. The uncertainty in temperature and pressure are derived from the sensitivity analysis, which was reported in section A.5. The corresponding uncertainty due to impact shift is reported in Table A2.

Table A.2 Impact shift uncertainty (GHz) based on temperature and pressure uncertainties for two noise levels.

Impact Shift Uncertainty (GHz)		
Mach Number	1% noise	3% noise
1	0.15	0.29
2	0.11	0.15
5	0.058	0.075
8	0.046	0.080
10	0.041	0.071

A.8 Laser Propagation Angle Uncertainty

The accurate measurement of the laser propagation angles is necessary in solving for the two components of velocity, especially since the angles are not nearly orthogonal and can contribute significantly to the overall magnitude of the velocity. For one laser angle, the laser sheet is almost perfectly horizontal and so uncertainty in the measurement was taken as ±0.5 degrees while the other angle had a steep angle with a slightly higher uncertainty of ±1 degree. The transverse and parallel data from both laser propagation angles was subjected to the velocity calculation with the uncertainty in angle measurement included. The resulting difference in calculated velocity contributed to the overall error.

The uncertainty for both the transverse and parallel cases due to laser propagation angle miscalculation is 1.4% of the velocity.

A.9 Overall Temperature Uncertainty

The overall uncertainty in temperature, S_T, was calculated by taking the square root of the sum of the squares of uncertainty due to the noise in the data and fitting program and the uncertainty due to the laser misalignment. The temperature fields that are reported in this research do not include the more noisy data and so only the uncertainty based on the 1% additive error are reported in Table A3. The more noise data, though, does contribute to the velocity uncertainty and so has been included in the calculation of error thus far.

Table A3 Temperature Uncertainty for Temperature Fields

Temperature Uncertainty		
Mach Number	(K)	(%)
1	68	28
2	33	20
5	5.0	10
8	1.9	8.8
10	0.80	5.6

A.10 Overall Velocity Uncertainty

The overall velocity uncertainty, S_V, can be calculated from the contributions of uncertainty due to the noise in the data, uncertainty in velocity due to uncertainty of pressure and temperature in the impact shift calculation, uncertainty from the laser propagation angle, and uncertainty from the laser misalignment. Due to the fact that there are two velocity components that contribute to the overall velocity, the uncertainty in impact shift and shift must be accounted for each direction as shown in the following equation:

$$S_v = \sqrt{S_{impact,1}^2 + S_{shift,1}^2 + S_{impact,2}^2 + S_{shift,2}^2 + S_{angle}^2} \qquad (A3)$$

For the transverse configuration, the noise for both components of velocity is characterized by the 1% additive noise. For the parallel configuration, the noise for one of the components of velocity is characterized by 1% additive noise and one component of velocity is characterized by 3% additive noise. Accounting for these differences in noise between the two components, uncertainty for velocity is given in Table A4.

Table A4 Velocity Uncertainty for RCS Parallel and Transverse Configurations

Velocity Uncertainty				
Mach Number	Transverse		Parallel	
	m/s	%	m/s	%
1	110	35	170	53
2	77	15	95	18
5	43	6.0	50	6.9
8	35	4.6	49	6.4
10	32	4.2	44	5.7

A.11 Note on the Uncertainty

It is obvious that the experimental method has a lot of uncertainty in the continuum, low-velocity regions of the flow. However, it must be noted that since the underexpanded RCS jets quickly expand into low-pressure region, this continuum regime is actually only a small portion of the overall flowfield. Above Mach 5 conditions, the uncertainties in temperature are under 10% and uncertainties in velocity are less than 6%. If one accounts for the regions of the flow below Mach 5 and at high to moderate pressures, these regions compose less than 10% of the entire flowfield. Thus, throughout most of the flow, the measured velocities and temperatures are very accurate. The PLIIF technique is, therefore, shown to be capable of producing accurate quantitative results.

APPENDIX B

RCS CAD DRAWINGS

These drawings were given to the machinist to machine the models for the experiment. The drawings were completed by UVA Aerospace Engineering undergraduate Jerry Kahn with input and specifications.
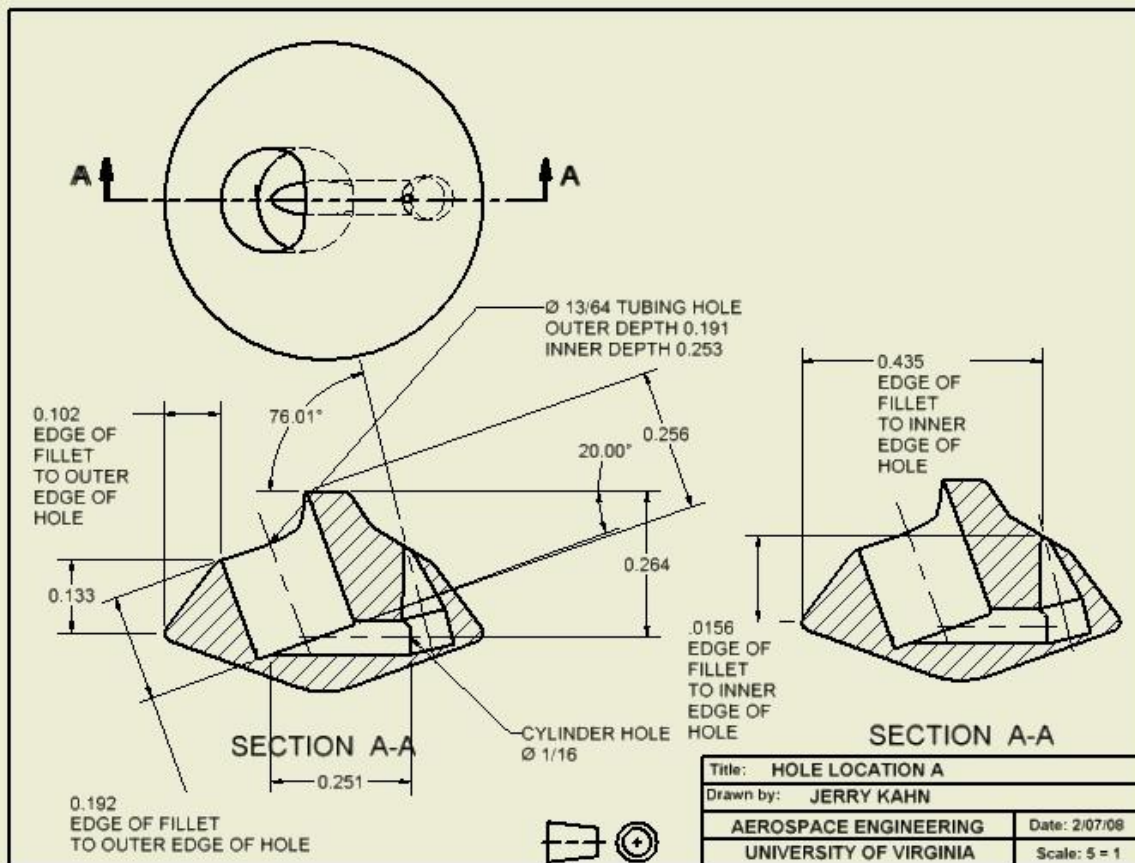
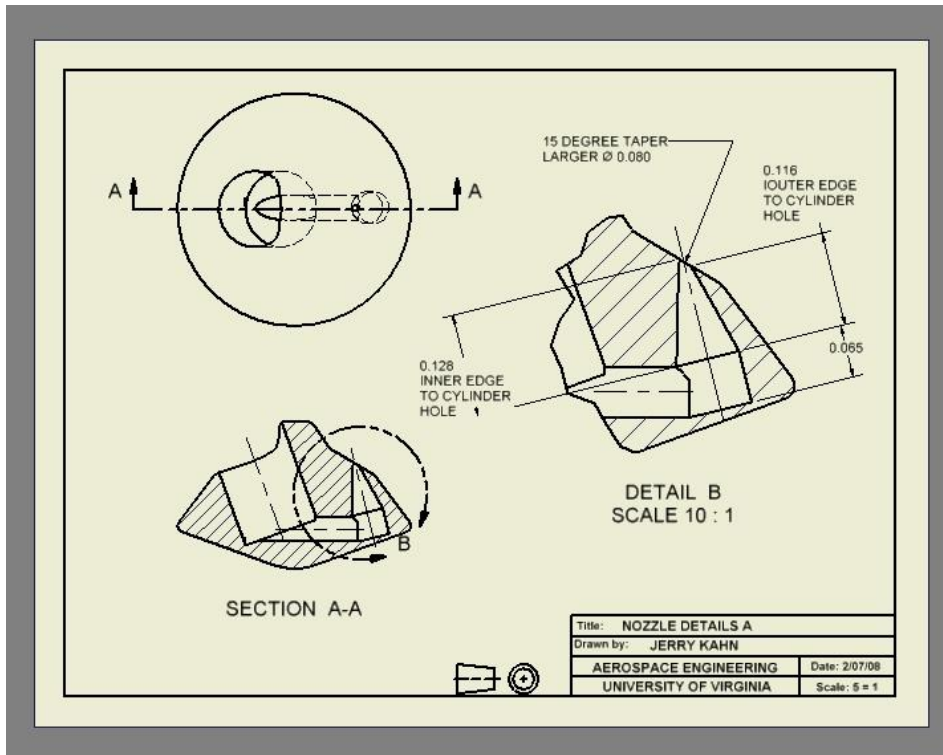Figure B.1: RCS Parallel Jet Configuration

Figure B.2: RCS Parallel Jet Configuration, Internal Detail
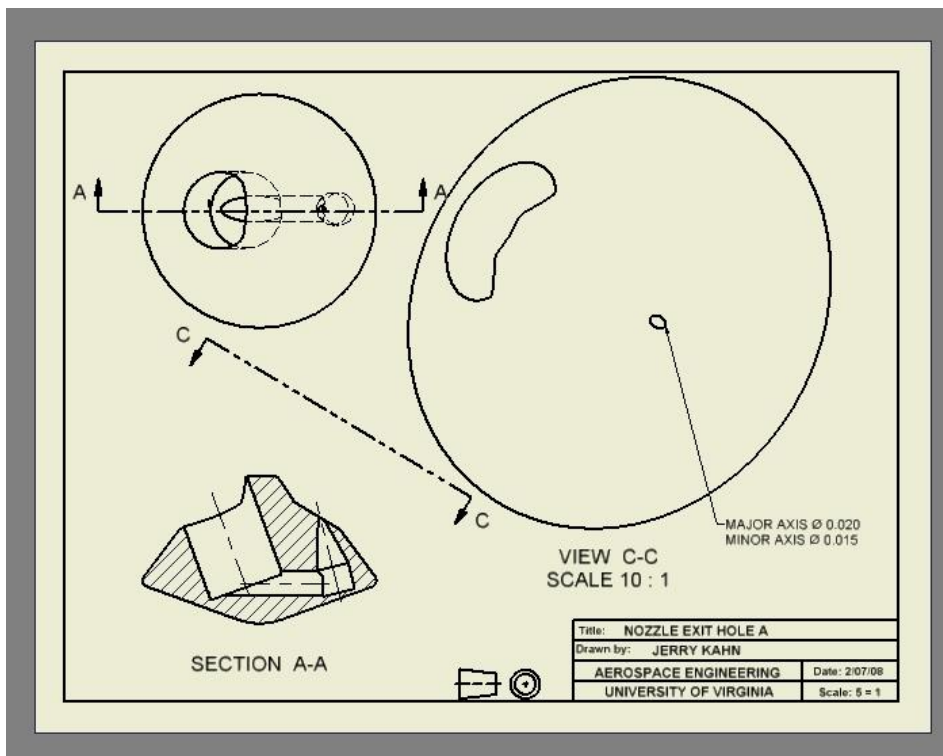
Figure B.3: RCS Parallel Jet Configuration, External Detail
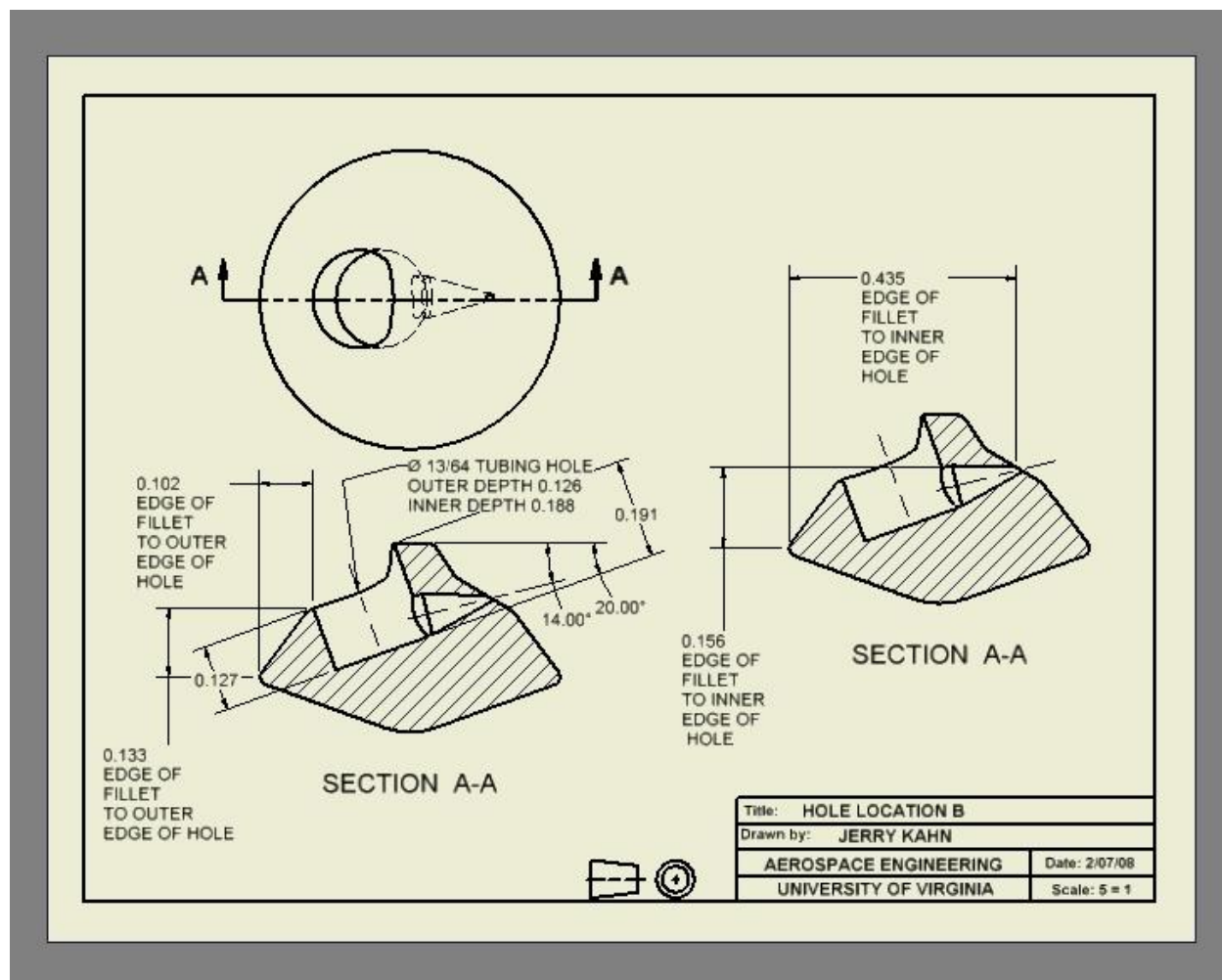
Figure B.4: RCS Transverse Jet Configuration
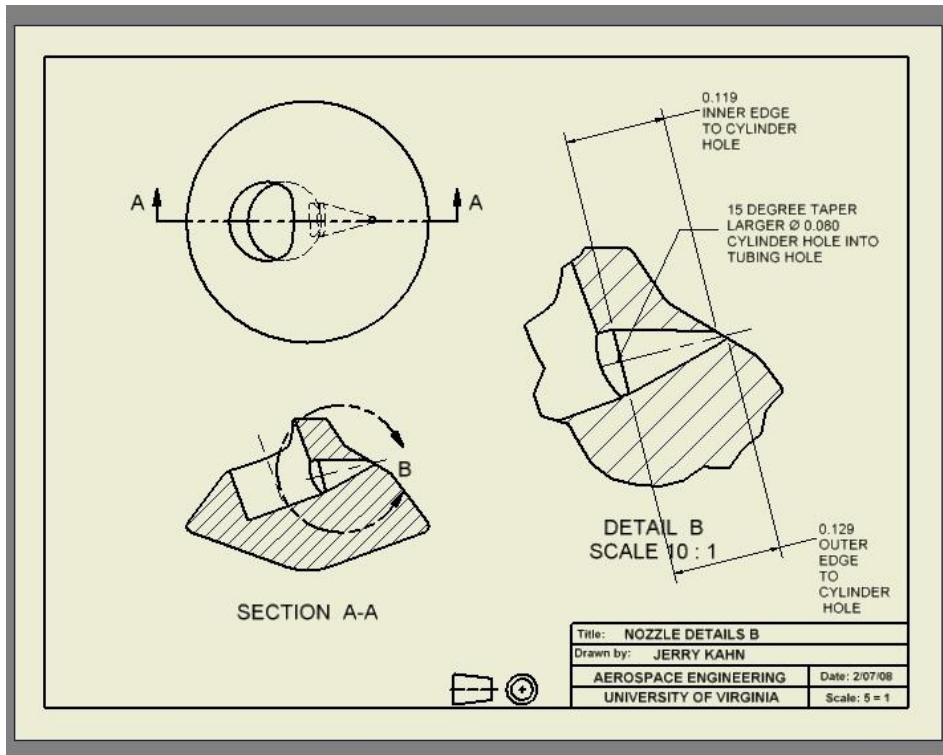
Figure B.5: RCS Transverse Jet Configuration, Internal Detail
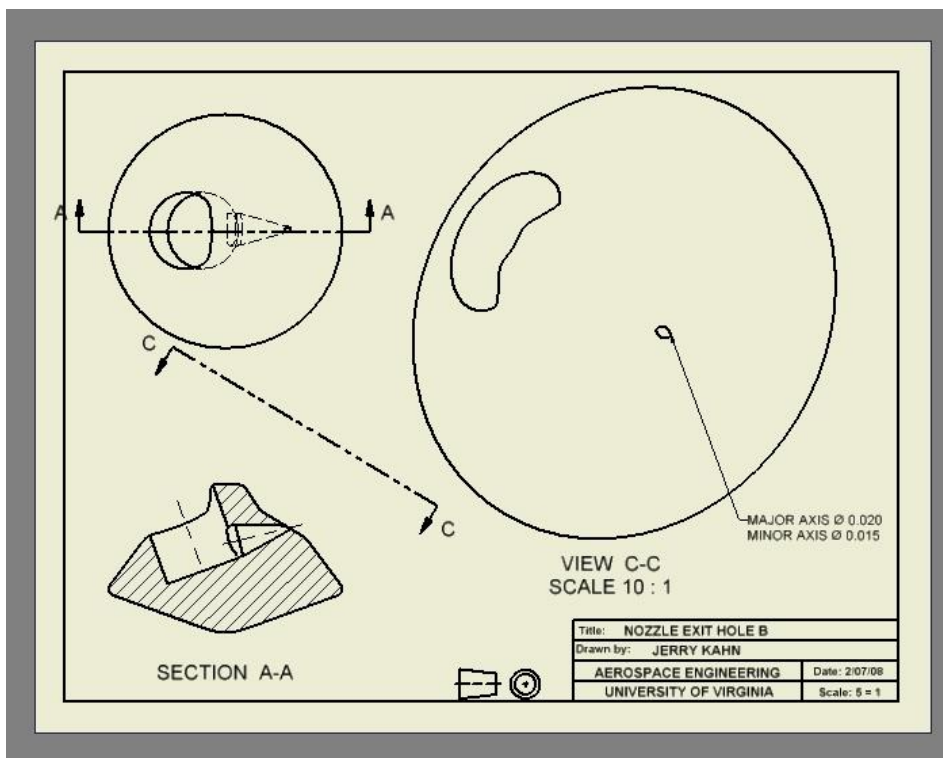
Figure B.6: RCS Transverse Jet Configuration, External Detail

APPENDIX C

DATA COLLECTION PROCEDURE

To run the experiment, the following steps are taken:

(1) Turn on the laser and the etalon heater and allow both to warm up. This is generally given a period of one to two hours. Because the laser cavity is sensitive to temperature, it is important to give the laser adequate time to warm up so that the laser frequency and sheet location do not drift during the rest of the experiment run.

(2) Adjust the optics to allow for proper alignment on the model. This should be performed after the laser has warmed up so that the optics will properly focus on the RCS jet exit on the model.

(3) Turn on the vacuum pumps to bring down chamber to a low back pressure. Each pump is turned on and pressure is monitored until it no longer continues to decrease before turning on the next pump. Five to ten minutes is generally required before the next stage pump is turned on.

(4) Turn on the liquid nitrogen to cool the baffle on the chamber. The liquid nitrogen is important to help trap the iodine leaving the vacuum chamber in order to allow for

proper exhaust. The iodine and nitrogen are pulled through the pumps and into a piping system that includes a tank of carbon iodine scrubbers to clear the nitrogen of any iodine before exhausting to the ambient. With the liquid nitrogen on, the back pressure of the vacuum chamber can be nominally controlled or maintained throughout the run.

(5) Open up the Labview program to set up files and set the camera temperature on the camera and start cooling it down. The camera temperature is usually set at -90 degrees C and can effectively remain this temperature throughout the entire run. This low temperature greatly reduces shot noise and helps maintain desirable quantum efficiency levels, resulting in low background levels.

(6) Open up the nitrogen farm outside and bring nitrogen into the mixing chamber to seed iodine. Up to eighteen nitrogen tanks may be opened up for any given run. On an average run about 1/3 to ½ of full nitrogen farm capacity is used, depending largely on the thrust coefficient being used. At the nitrogen farm, the valve is opened up to about 30-50 psig. From the nitrogen tank, the gas in introduced into the iodine settling chamber where the pressure in the tank is allowed to raise to match the open valve conditions. The gas is introduced into the iodine chamber through various actuated valves and the system is set up to allow for both the main jet and the RCS jet to be seeded, for just the RCS jet to be seeded, or for both jets to remain unseeded.

(7) Open up flow into the vacuum chamber and through the model. The main jet flow and the RCS jet flow are controlled through two separate lines even when both are seeded. Controlling these separately allows for the RCS jet to be adjusted to various

thrust coefficients. The desired valve is opened and adjusted and then the resulting flow is monitored and adjusted as needed. (The RCS jet pressure especially takes some time to stabilize)

(8) Take preliminary images to check for iodine levels in the flow to adjust for proper exposure times. Because the fluorescence levels are due to a number of different uncontrollable factors, there is no specific guarantee on the resulting signal levels. This step is important in changing the exposure times to optimize use of the dynamic range of the CCD camera. If the experiment being conducted is a quantitative one, the frequency can first be tuned to the P13/R15 peak for peak signal levels to avoid over-saturation of the CCD. If the experiment being conducted is qualitative, this step is not necessary as the exposure times and signals are adjusted for each thrust coefficient. Several images are taken at several different exposure times in order to ensure best use of the sensitivity range for fluorescence signal levels. In order to reduce noise from outside light sources (other than the laser) the lights in the room are turned off and a laser curtain is pulled in front of the computer area of the room to minimize glare from the computer screens.

(9) Scan through laser profile using Labview program. This step is not completed for qualitative work since the laser profile is not scanned through but is being run in broadband mode (without the use of the etalon). For the quantitative experiments, the user must first specify folders to save the data in and filenames. The user then uses the program to tune the laser to a desired starting frequency. Once the scan is started, it runs automatically from the starting frequency to a user-specified ending

frequency in user-specified frequency steps (usually 20-25 MHz). Scans can be stopped mid-run and re-started as necessary.

(10) Make adjustments to the system as necessary. During a laser scan, it is necessary to make minor, occasional adjustments to RCS jet pressures and main jet pressures, as well as minor laser sheet position adjustments. It is also important to check on the water levels for the laser cooling system, liquid nitrogen levels and nitrogen farm levels.

(11) Once a scan is completed, background images are taken to account for reflections from the laser sheet as well as noise from the camera. These images are taken with the laser sheet in place and the laser on but with the flow turned off so that there is no fluorescence seen.

(12) Shut down system in opposite order from start up. The vacuum system is brought back to atmospheric conditions by filling the pumps and the vacuum chamber with dry nitrogen air. It is important to refill with dry nitrogen air because iodine reacts strongly with water vapor and so refilling with normal air could cause residual iodine to react and create iodic acid, thus corroding the system.

APPENDIX D

PHOTOMETRIC CAMERA IMAGES

The following images are images from the Photometric Camera which was discussed previously. These images are shown here for completeness of the body of research.

$C_T = 0.5$ $C_T = 1.0$
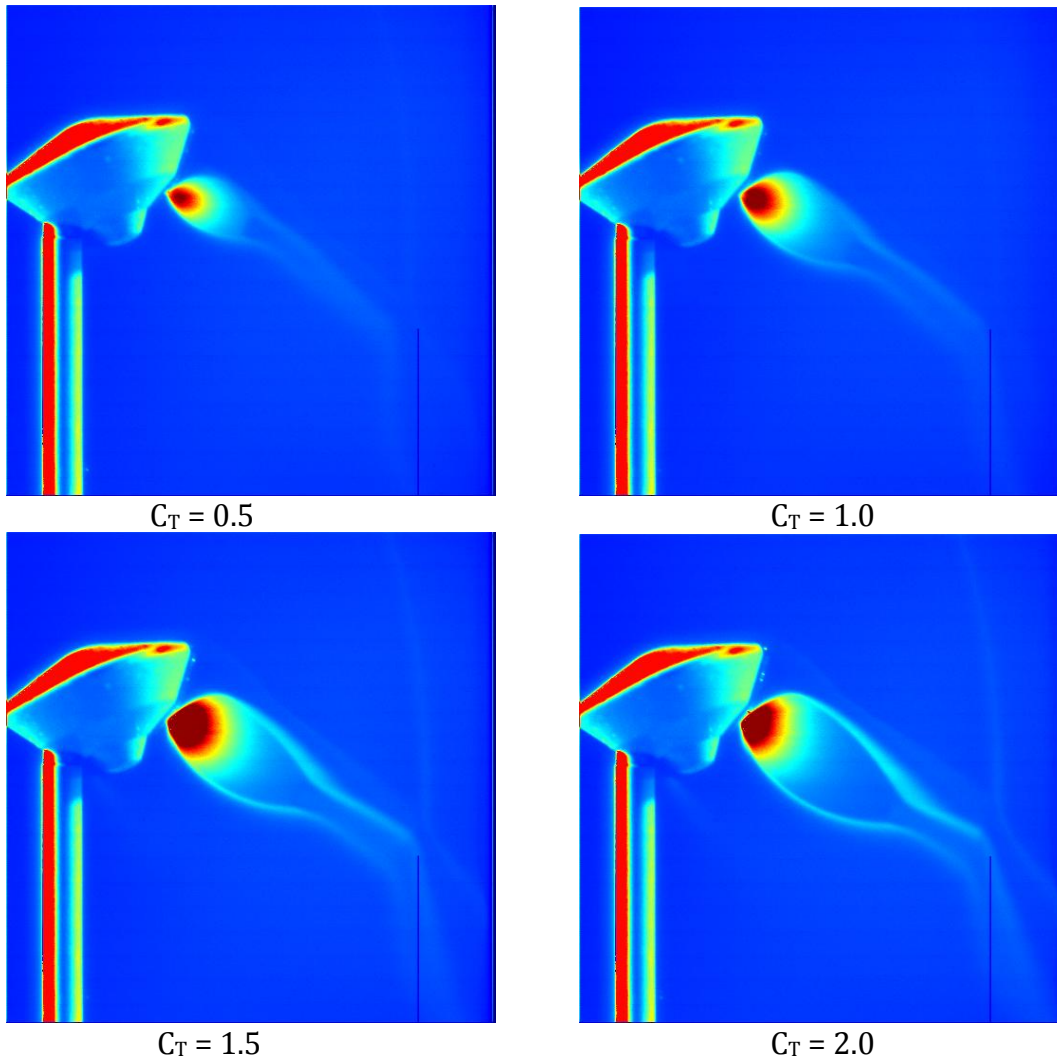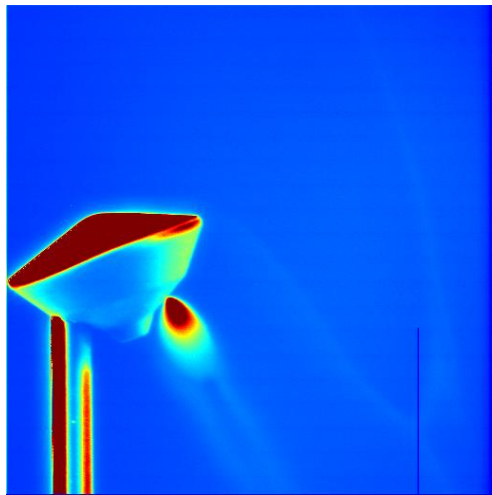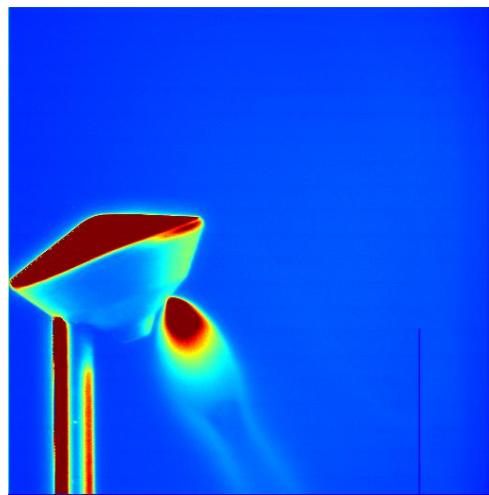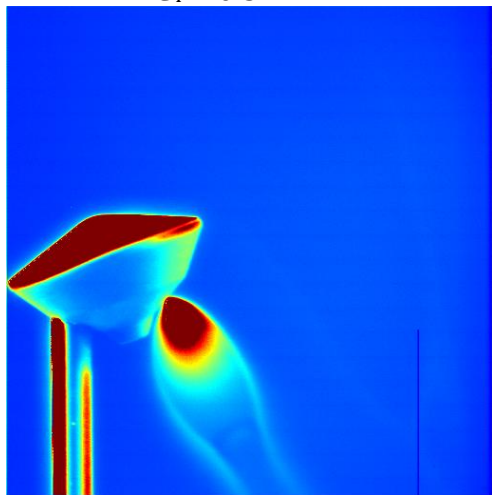
$C_T = 1.5$ $C_T = 2.0$

Figure D.1: RCS Transverse Jet Images, 2 cm model, Mach 12 freestream
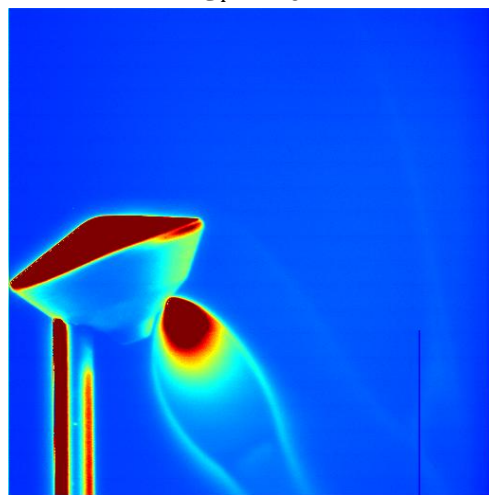
C_T = 0.5   C_T = 1.0

C_T = 1.5   C_T = 2.0

Figure D.2: RCS Transverse Jet Images, 2 cm model, Mach 12 freestream

WORKS CITED

[1] Braun, R.D., Manning, R.M., "Mars Exploration Entry, Descent and Landing Challenges." Aerospace Conference, IEEE, 2006. Paper #0076.

[2] Rivellini, Tommaso. "The Challenges of Landing on Mars." *Frontiers of Engineering, Tenth Symposium*. National Academy of Engineering: Washington DC, 2004.

[3] Way, D.W., Powell, R.W., Chen, A., Steltzner, A.D., San Martin, A.M., Burkhart, P.D., Mendeck, G.D., "Mars Science Laboratory: Entry, Descent and Landing System Performance." IEEE, 2006. Paper #1467.

[4] Braun, R.D., "Importance of Simulation." *Planetary Entry, Descent and Landing – Hypersonic Educational Initiative*. Hampton, VA: National Institute of Aerospace, April 1, 2008.

[5] Lockwood, M.K., "Introduction: Mars Science Laboratory: The Next Generation of Mars Landers." *Journal of Spacecraft and Rockets*. Vol. 43, No. 2, (2006) p.257.

[6] Steltzner, A., Kipp, D., Chen, A., Burkhart, D., Guernsey, C., Mendeck, G., Mitcheltree, R., Power, R., Rivellini, T., San Martin, M., Way, D., "Mars Science Laboratory Entry, Descent, and Landing System." Aerospace Conference, IEEE, 2006. Paper #1497.

[7] Mitcheltree, R., Steltzner, A., Chen, A., San Martin, M., Rivellini, T., "Mars Science Laboratory Entry Descent and Landing System Verification and Validation Program." IEEE, 2006. Paper #1498.

[8] Edquist, K.T., Dyakonov, A.A., Wright, M.J., Tang, C.Y., "Aerothermodynamics Environments Definition for the Mars Science Laboratory Entry Capsule." *45th AIAA Aerospace Sciences Meeting*, Reno NV, 2007, Paper AIAA 2007-1206.

[9] Dyakonov, A.A., Glass, C.E., Desai, P.N., Van Norman, J.W., "Analysis of Effectiveness of Phoenix Entry Reaction Control System," *Journal of Spacecraft and Rockets*, Vol. 48, No. 5 (2011), pp. 746-755.

[10] Prince, J.L.H, Chavis, Z.Q., Wilmoth, R.G., "Modeling Reaction-Control-System Effects on Mars Odyssey," *Journal of Spacecraft and Rockets*, Vol. 42, No. 3 (2005), pp. 444-449.

[11] Danehy, P.M., Inman, J.A., Brauckmann, G.J., Alderfer, D.W., Jones, S.B., Patry, D.P., "Visualization of a Capsule Entry Vehicle Reaction-Control-System Thruster," *Journal of Spacecraft and Rockets*, Vol. 46, No. 1 (2009), pp. 93-102.

[12] Rault, D.F., Cestero, F.J., Shane, R.W., "Spacecraft Aerodynamics During Aerobraking Maneuver in Planetary Atmosphere," *AIAA Thermophysics Conference*, New Orleans, LA, 1996, Paper 96-1890.

[13] Chavis, Z.Q., Wilmoth, R.G., "Plume Modeling and Application to Mars 2001 Odyssey Aerobraking," *8th AIAA/ASME Joint Thermophysics and Heat Transfer Conference*, 2002, Paper 2002-2896.

[14] Romeo, D.J., Sterrett, J.R., "Aerodynamic Interactions Effects Ahead of a Sonic Jet Exhausting Perpendicularly From a Flat Plate Into a Mach Number 6 Free Stream," Washington, DC: Nasa, Technical Note D-743, April 1961.

[15] Rausch, R.R., Roberts, B.B., "Reaction Control System Plume Flow Field Interaction Effects on the Space Shuttle Orbiter," *AIAA/SAE 10th Propulsion Conference*, 1971, Paper 74-1104.

[16] Spaid, F.W., Cassel, L.A., "Aerodynamic Interference Induced by Reaction Controls," Huntington Beach, CA: McDonnell Douglas Corporation, 1973, AGARD-AG-173.

[17] Scalabrin, L. C., and Boyd, I. D., Development of an Unstructured Navier-Stokes Solver for Hypersonic Nonequilibrium Aerothermodynamics, *AIAA 2005-5203*, June 2005.

[18] Scalabrin, L. C., and Boyd, I. D., Numerical Simulation of Weakly Ionized Hypersonic Flow for Reentry Configurations, *AIAA 2006-3773*, June 2006.

[19] Karypis, G., and Kumar, V., *METIS: A Software Package for Partitioning Unstructured Graphs, Partitioning Meshes, and Computing Fill-Reducing Orderings of Sparse Matrices*, University of Minnesota, 1998.

[20] Hiller, B., "Combined Planar Measurements of Velocity and Pressure Fields in Compressible Gas Flows using Laser-Induced Iodine Fluorescence," High Temperature Gasdynamics Laboratory: Stanford University, Topical Report T-256, November 1986.

[21] Cecil, D.E., "Planar Laser-Induced Iodine Flourescence Measurements in Rarefied Hypersonic Flow Over a Reaction Control Jet Model in a Free Jet Wind Tunnel," *Masters of Science Thesis*, Charlottesville VA: University of Virginia, January 2004.

[22] Lengrand, J.C., Allegre, J., Raffin, M., "Electron Beam Fluorescence Technique at Relatively High Density," *Rarefied Gas Dynamics, Vol. I* ed. Hakuro Oguchi, Tokyo, Japan: University of Tokyo Press, 1984, pp. 423-429.

[23] Gochberg, L.A., "Electron Beam Fluorescence Methods in Hypersonic Aerothermodynamics," *Prog. Aerospace Sci.,* Vol. 33 (1997), pp. 431-480.

[24] Tsuboi, N., Matsumoto, Y., "Interaction Between Shock Wave and Boundary Layer in Nonequilibrium Hypersonic Rarefied Flow," *JSME International Journal*, *Series B*, Vol. 45, No. 3 (2006), pp. 771-779.

[25] Munz, E.P., "The Electron Beam Fluorescence Technique," France: NATO-AGARD, AGARD-AG-132, December 1968.

[26] McDaniel, J.C., "Investigation of Laser-Induced Iodine Fluorescence for the Measurement of Density in Compressible Flows," *PhD Dissertation*, Palo Alto, CA: Stanford Univeristy, 1981.

[27] Tellinghuisen, J., "Intensity Factors for I_2 B↔X Band System," *Journal of Quantitative Spectroscopy and Radiative Transfer,* Vol. 19 (1978), pp. 149-161.

[28] Steinfeld, J.I., "Wavelength Dependence of the Quenching of Iodine Fluorescence," *Journal of Chemical Physics*, Vol. 44, No. 7 (1966), pp. 2470-2749.

[29] Gerstenkorn, S., Luc, P., *Atlas du Spectre d'Absorption de la Molécule d'Iode.* Éditions du Centre National de la Recherche Scientifique, Paris, France: 1978, p. 89.

[30] Capelle, G.A., Broida, H.P., "Lifetimes and Quenching Cross Sections of I_2 ($B^3\Pi_{0u}^+$)," *Journal of Chemical Physics,* Vol. 58, No. 10 (1973), pp. 4212-4222.

[31] Herzberg, G., *Molecular Spectra and and Molecular Structure: III. Electronic Spectra and Electronic Structure of Polyatomic Molecules*, Princeton, NJ: D. Van Nostrand Company, Inc., 1966.

[32] Fletcher, D.G., McDaniel, J.C., "Laser-Induced Iodine Fluorescence Technique for Quantitative Measurement in a Nonreacting Supersonic Combustor," *AIAA Journal*, Vol. 27, No. 5 (1989), pp. 575-580.

[33] Hartfield, R.J., Hollo, S.D., McDaniel, J.C., "Experimental Investigation of a Supersonic Swept Ramp Injector using Laser-Induced Iodine Fluorescence," *Journal of Propulsion and Power*, Vol. 10, No. 1 (1994), pp. 129-135.

[34] Donohue, J.M, McDaniel, J.C., "Complete 3-D Multi-Parameter Mapping of a Swept Ramp Fuel Injector using Planer Laser-Induced Iodine Fluorescence," *AIAA Aerospace Sciences Meeting,* Reno, NV, Jan. 1995, AIAA 1995-0423.

[35] Hollo, S.D., "Planar Mole Fraction and Velocity Imaging of Compressible Mixing in a Nonreacting Mach 2 Combustor," *Masters of Science Thesis*, Charlottesville, VA: University of Virginia, May 1991.

[36] Staack, D., McDaniel, J.C., Glass, C.E., Miller, C., "Experimental Study of Interacting Rarefied and Continuum Flow," *35th AIAA Thermophysics Conference,* Anaheim, CA, 2001, Paper 2001-2762.

[37] Exton, R.J., Balla, R.J., Shirinzadeh, B., Hillard, M.E., Brauckmann, G., "Flow Visualization Using Fluorescence from Locally Seeded I_2 Excited by an ArF Excimer Laser," *Experiments in Fluids,* Vol. 26 (1999), pp. 335-339.

[38] Alderfer, D.W., Danehy, P.M., Inman, J.A., Berger, K.T., Buck, G.M., Schwartz, R.J., "Fluorescence Visualization of Hypersonic Flow over Rapid Prototype Wind-Tunnel Models," *45th AIAA Aerospace Sciences Meeting*, Reno, NV, 2007, AIAA 2007-1063.

[39] Danehy, P.M., Wilkes, J.A., Alderfer, D.W., Jones, S.B., Robbins, A.W., Patry, D.P., Schwartz, R.J., "Planar Laser-Induced Fluorescence (PLIF) Investigation of Hypersonic Flowfields in a Mach 10 Wind Tunnel (invited)," *25th AIAA Aerodynamic Measurement Technology and Ground Testing Conference*, San Francisco, CA, 2006, AIAA 2006-3442.

[40] Jiang, N., Webster, M., Lempert, W.R., Miller, J.D., Meyer, T.R., Ivey, C.B., Danehy, P.M., "MHz-Rate Nitric Oxide Planar Laser-Induced Fluorescence Imaging in a Mach 10 Hypersonic Wind Tunnel," *Applied Optics*, Vol. 50, No. 4 (2011), pp. A20-A28.

[41] Danehy, P.M., Garcia, A.P., Borg, S., Dyakonov, A.A., Berry, B.A., Inman, J.A., Alderfer, D.W., "Fluorescence Visualization of Hypersonic Flow Past Triangular and Rectangular Boundary-Layer Trips," *45th AIAA Aerospace Sciences Meeting,* Reno, NV, 2007, AIAA 2007-536.

[42] Wilkes, J.A., Glass, C.E., Danehy, P.M., Nowak, R.J., "Fluorescence Imaging of Underexpanded Jets and Comparison with CFD," *44th AIAA Aerospace Sciences Meeting*, Reno, NV, 2006, AIAA 2006-910.

[43] Ni-imi, T., "Optical Diagnostics of Nonequilibrium Phenomena in Highly Rarefied Gas Flows," Rarefied Gas Dynamics, American Institute of Physics, Vol. 663 (2003), pp. 1025-1032.

[44] Ni-imi, T., Fujimoto, T., Ishida, T., "Selection of Absorption Line for I_2-Planar Laser-Induced Fluorescence Measurement of Temperature in a Compressible Flow, *Applied Optics*, Vol. 34, No. 27 (1995), pp. 6275-6281.

[45] Hiller, B., Hanson, R.K., "Simultaneous Planar Measurements of Velocity and Pressure Fields in Gas Flows Using Laser-Induced Fluorescence," *Applied Optics*, Vol. 27, No. 1 (1988), pp. 34-48.

[46] McDaniel, J.C., "Quantitative Measurement of Density and Velocity in Compressible Flows Using Laser-Induced Iodine Fluorescence," *AIAA Aerospace Sciences Meeting*, 1983, AIAA 83-0049.

[47] Donohue, J.M., McDaniel, J.C., Haj-Hariri, H., "Experimental and Numerical Study of Swept Ramp Injection into a Supersonic Flowfield," *AIAA Journal*, Vol. 32, No. 9 (1994), pp. 1860-1867.

[48] Hartfield, R.J., Hollo, S.D., McDaniel, J.C., "Planar Temperature Measurement in Compressible Flows Using Laser-Induced Iodine Fluorescence," *Optics Letter*, Vol. 16 (1991), p. 2.

[49] Reed, E.M., Codoni, J.R., McDaniel, J.C., Alkandry, H., Boyd, I.D., "Investigation of the Interactions of Reaction Control Systems with Mars Science Laboratory Aeroshell," *AIAA Aerospace Sciences Meeting,* Orlando, FL, 2010, AIAA 2010-1558.

[50] Hirai, E., Teshima, K., Kurita, K., Takahara, S., "Velocity Measurement of Free Jets Using Nuclear Hyperfine Structure of I_2," *JSME International Journal,* Series B., Vol. 40, No. 3 (1997), pp. 501-508.

[51] Gross, K.P., McKenzie, R.L, Logan, P., "Measurements of Temperature, Density, Pressure and Their Fluctuations in Supersonic Turbulence Using Laser-Induced Fluorescence," *Experiments in Fluids,* Vol. 5 (1987), pp. 372-380.

[52] McDaniel, J.C., Cecil, D.E., Reed, E.M., Codoni, J.R., Boyd, I.D., Alkandry, H., "Planar Laser-Induced Iodine Fluorescence Technique for Flow Visualization and Quantitative Measurements in Rarefied Flow," *27th International Symposium on Rarefied Gas Dynamics,* Pacific Grove, CA, July 2010, invited paper.

[53] Cecil, D.E., McDaniel, J.C., "Direct Monte Carlo Simulations of a Binary Gas Free-Jet Flow over a Flat Plate," *International Rarefied Gas Dynamics Symposium,* Monterey, CA, July 2010.

[54] McDaniel, J.C., Cecil, D.E., Reed, E.M., Codoni, J.R., "Planar Laser-Induced Iodine Fluorescence Technique for Flow Visualization and Quantitative Measurements in Rarefied Flows," *International Rarefied Gas Dynamics Symposium,* Monterey, CA, July 2010.

[55] Cecil, D.E., McDaniel, J.C., "Planar Laser-Induced Iodine Fluorescence Measurements in Rarefied Hypersonic Flow," *Proceedings of the International Rarefied Gas Dynamics Symposium,* Toronto, Canada, 2005, pp. 1325-1350.

[56] Staack, D.A., "Experimental Study of Interacting Rarefied and Continuum Flows Using Planar Laser-Induced Iodine Fluorescence," *M.S. Thesis*, Charlottesville, VA: University of Virginia, January 2001.

[57] Viti, V., Neel, R., Schetz, J.A., "Detailed Flow Physics of the Supersonic Jet Interaction Flow Field," *Physics of Fluids,* Vol. 21 (2009) 046101-1.

[58] Orth, R.C., Funk, J.A., "An Experimental and Comparative Study of Jet Penetration in Supersonic Flow," *Journal of Spacecraft and Rockets*, Vol. 4, No. 9 (1967), pp. 1236-1242.

[59] Tartabini, P.V., Wilmoth, R.G., Rault, D.F.G., "A Systems Approach to a DSMC Calculation of a Control Jet Interaction Experiment," *AIAA 28th Thermophysics Conference*, Orlando, FL, 1993, AIAA 83-2798.

[60] Glass, C.E., LeBeau, G.J., "Numerical Study of a Continuum Sonic Jet Interacting with a Rarefied Flow," *32nd Thermophysics Conference*, Atlanta, GA, 1997, AIAA 97-2536.

[61] Zakkay, V., Calarese, W., Sakell, L., "An Experimental Investigation of the Interaction between a Transverse Sonic Jet and a Hypersonic Stream," *AIAA Journal*, Vol. 9, No. 4 (1971), pp. 674-82.

[62] Gülhan, A., Shütte, G., Stahl, B., "Experimental Study on Aerothermal Heating Caused by Jet-Hypersonic Crossflow Interaction," *Journal of Spacecraft and Rockets,* Vol. 45, No. 5 (2008), pp. 891-899.

[63] Ebrahimi, H.B., "Numerical Investigation of Jet Interaction in a Supersonic Freestream," *Journal of Spacecraft and Rockets,* Vol. 45, No. 1 (2008), pp. 95-103.

[64] Gimelshein, S.F., Levin, D.A., Alexeenko, A.A., "Modeling of Chemically Reacting Flows from a Side Jet at High Altitudes," *Journal of Spacecraft and Rockets*, Vol. 41, No. 4 (2004), pp. 582-591.

[65] Moss, J.N., Anderson, E.C., Bolz, C.W, Jr., "Aerothermal Environment for Jovian Entry Probes," *AIAA 11th Thermophysics Conference,* San Diego, CA, 1976, AIAA 76-469.

[66] Moss, J.N., Price, J.M., "Review of Blunt Body Wake Flows at Hypersonic Low Density Conditions," *31st AIAA Thermophysics Conference,* New Orleans, LA, 1996, AIAA 96-1803.

[67] Romeo, D.J., Sterrett, J.R., "Exploratory Investigation of the Effect of a Forward-Facing Jet on the Bow Shock of a Blunt Body in a Mach Number 6 Free Stream," Washington DC: NASA, Technical Note D-1605, February 1963.

[68] McGhee, R.J., "Effects of a Retronozzle Located at the Apex of a 140° Blunt Cone at Mach Numbers of 3.00, 4.50, and 6.00," Washington DC: NASA, Technical Note D-6002, January 1971.

[69] Jarvinen, P.O., Adams, R.H., "The Effects of Retrorockets on the Aerodynamic Characteristics of Conical Aeroshell Planetary Entry Vehicles," *AIAA 8th Aerospace Sciences Meeting,* New York, NY, 1970, AIAA 70-219.

[70] Swink, D.G., Morgan, O.M., Robinson, J.C., "Design and Analysis of a Low-cost Reaction Control System for GPS IIF," AIAA Paper 99-2469.

[71] McCullough, M.G., "Integration and Test of the EO-1 Reaction Control System," AIAA Paper 2001-3392.

[72] Stechman, R.C., Sumpter, D., "Development History of the Apollo Reaction Control System Rocket Engine," AIAA Paper 89-2388.

[73] Sholl, M., Leeds, M., Holbrook, J., "THEMIS Reaction Control System – From I&T Through Early Mission Operations," *43rd AIAA/ASME/SAE/ASEE Joint Propulsion Conference,* Cincinnati, OH, 2007, AIAA 2007-5579.

[74] McGregor, R.D., Lohn, P.D., Haflinger, D.E., "Plume Impingement Study for Reaction Control System of the Orbital Maneuvering Vehicle," *AIAA/ASME 5th Joint Thermophysics and Heat Transfer Conference,* Seattle, WA, 1990, AIAA 90-1708.

[75] Hall, S.E., Lewis, M.J., Akin, D.L., "Design of a High Density Cold Gas Attitude Control System," *AIAA/ASME 29th Joint Propulsion Conference*, Monterey, CA, 1993, AIAA 93-2583.

[76] Watkins, A.N., Buck, G.M., Leighty, B.D., Lipford, W.E., "Using Pressure- and Temperature-Sensitive Paint for Global Surface Pressure and Temperature Measurements on the Aft-Body of a Capsule Reentry Vehicle," *46th AIAA Aerospace Sciences Meeting,* Reno, NV, 2008, AIAA 2008-1230.

[77] Rausch, J.R., Roberts, B.B., "Reaction Control System Aerodynamics Interaction Effects on Space Shuttle Orbiter," *Journal of Spacecraft and Rockets,* Vol. 12, No. 11, pp. 660-666.

[78] Brevig, O., Strike, W.T., Fisher, R.R., "Aerothermodynamics of the Space Shuttle Reaction Control System," *AIAA 11th Aerospace Sciences Meeting,* Washington, DC, 1973, AIAA 73-93.

[79] Stechman, R.C., Lawson, C., "Historical Evolution of the Space Shuttle Primary and Vernier Reaction Control Rocket Engine Designs," *42nd AIAA/ASME/SAE/ASEE Joint Propulsion Conference,* Sacramento, CA, 2006, AIAA 2006-4892.

[80] Rausch, J.R., "Space Shuttle Orbiter Reaction Control System Interactions with the Vehicle Flow Field," San Diego, CA: General Dynamics Convair Division, Report No. CASD-NAS-78-007 (1978).

[81] Spaid, F.W., et. al. "Aerodynamic Interference Induced by Reaction Controls," Paris, France: Advisory Group for Aerospace Research and Development, December 1973, AD-775 209.

[82] Strike, W.T., Scheuler, C.J., Deitering, J.S., "Interactions Produced by Sonic Lateral Jets Located on Surfaces in a Supersonic Stream," Arnold Engineering Development Center, Arnold Air Force Station, Tennessee. AEDC-TDR-63-22, April 1963. (Unclassified Report)

[83] Hanna, J.L., Chavis, Z.Q., Wilmoth, R.G., "Modeling Reaction Control System Effects on Mars Odyssey," *AIAA/AAS Astrodynamics Specialist Conference,* New Orleans, LA, 1996, AIAA 96-1890.

[84] Calhoun, P.C., Queen, E.M., "Entry Vehicle Control System Design for the Mars Science Laboratory," *Journal of Spacecraft and Rockets*, Vol. 48, No. 5 (2011), pp. 746-755.

[85] Staack, D.A., "Experimental Study of Interacting Rarefied and Continuum Flows Using Planar Laser-Induced Iodine Fluorescence," *Masters of Science Thesis*, Charlottesville, VA: University of Virginia, January 2001.

[86] Danehy, P.M., Wilkes, J.A., Brauckmann, G.J., Alderfer, D.W., Jones, S.B., Patry, D.P., "Visualization of a Capsule Entry Vehicle Reaaction-Control-System (RCS) Thruster," *44th AIAA Aerospace Sciences Meeting*, Reno, NV, 2006, AIAA 2006-1532.

[87] Danehy, P.M., Inman, J.A., Alderfer, D.W., Buck, G.M., Bathel, B., "Visualization of Flowfield Modification by RCS Jets on a Capsule Entry Vehicle," *46th AIAA Aerospace Sciences Meeting,* Reno, NV, 2008, AIAA 2008-1231.

[88] Inman, J.A., Danehy, P.M., Alderfer, D.W., Buck, G.M., McCrea, A., "Planar Fluoresence Imaging and Three-Dimensional Reconstructions of Capsule Reaction-Control-System Jets," *AIAA Journal,* Vol. 47, No. 4 (2009), pp. 803-812.

[89] Inman, J.A., Danehy, P.M., Alderfer, D.W., Buck, G.M.., McCrea, A., "PLIF Imaging of Capsule RCS Jets and Simulated Forebody Ablation," *46th AIAA Aerospace Sciences Meeting*, Reno, NV, 2008, AIAA 2008-248.

[90] Danehy, P.M., Inman, J.A., Brauckmann, G.J., Alderfer, D.W., Jones, S.B., "Visualization of a Capsule Entry Vehicle Reaction-Control-System Thruster," *Journal of Spacecraft and Rockets*, Vol. 46, No. 1 (2009), pp. 93-102.

[91] Hiller, B., "Combined Planar Measurements of Velocity and Pressure Fields in Compressible Gas Flows Using Laser-Induced Iodine Fluorescence," Topical Report T-256, November 1986.

[92] Incropera, Frank P., *Introduction to Molecular Structure and Thermodynamics*, New York City, NY: John Wiley and Sons, 1974.

[93] Atkins, P.W., *Physical Chemistry*, San Francisco: W.H. Freeman and Company, 1978.

[94] Levine, Ira N., *Molecular Spectroscopy*, New York, NY: John Wiley and Sons, 1975.

[95] McDaniel, J.C., Codoni, J.R., Reed, E.M., Alkandry, H., Boyd, I.D., "Propulsion Deceleration Studies Using Planer Laser-Induced Fluorescence and Computational Fluid Dynamics," *Journal of Spacecraft and Rockets*, Vol. 50, No. 4 (2013), pp. 771-780.

[96] Donohue, James M., "Ramp Injectors for Supersonic Mixing" *PhD Dissertation¸* Charlottesville, VA: University of Virginia, January 1995.

[97] Bernath, Peter F., *Spectra of Atoms and Molecules,* 2nd edition¸ New York, NY: Oxford University Press, 2005.

[98] Fletcher, Douglas, G., "Spatially-Resolved, Nonintrusive Measurements in a Nonreacting Scramjete Combustor Using Laser-Induced Iodine Fluorescence," *PhD Dissertation¸* Charlottesville, VA: University of Virginia, January 1989.

[99] Vincenti, W.G., Kruger, C.H., Jr., *Introduction to Physical Gas Dynamics¸* Malabar FL: Krieger Publishing Company, 1965.

[100] Hollo, S.D., Hartfield, R.J., McDaniel, J.C., "Planar Velocity Measurement in Symmetric Flow Fields with Laser-Induced Iodine Fluorescence," *Optics Letters,* Vol. 19, No. 3 (1994), pp. 216-218.

[101] Codoni, J.R., Reed, E.M., McDaniel, J.C., Alkandry, H., Boyd, I.D., "Investigations of Peripheral Propulsive Deceleration Jets on a Mars Science Laboratory Aeroshell," *Journal of Spacecraft and Rockets* (to be published). DOI: 10.2514/1.A32456

[102] Codoni, J.R., Reed, E.M., McDaniel, J.C., Alkandry, H., Boyd, I.D., "Investigations of Peripheral Propulsive Deceleration Jets on a Mars Science Laboratory Aeroshell," *AIAA Aerospace Sciences Meeting¸*2011, AIAA 2011-1036

[103] Ashkenas, H., Sherman, F.S., "The Structure and Utilization of Supersonic Free Jets in Low Density Wind Tunnels," *Rarefied Gas Dynamics,* Vol. II, Ed. J.H. de Leeuw, New York, NY: Academic Press, 1966, pp. 84-105.

[104] Personal communication with NASA Langley Aerothermodynamics Branch, Langley, VA: NASA, March 22, 2007.

[105] Korzun, A.M., Cruz, J.R., Braun, R.D., "A Survey of Supersonic Retropropulsion Technology for Mars Entry, Descent and Landing," IEEE, 2007, Paper 1246.

[106] Korzun, A.M., Cruz, J.R., Braun, R.D., "Survey of Supersonic Retropropulsion Technology for Mars Entry, Descent and Landing," *Journal of Spacecraft and Rockets*, Vol. 46, No. 5 (2009), pp. 929-937.

[107] Alkandry, Hicham, "Aerodynamic Interactions of Propulsive Deceleration and Reaction Control System Jets on Mars-Entry Aeroshells," *PhD Dissertation¸* Ann Arbor, MI: University of Michigan, 2012.

[108] Bernath, Peter F. "Molecular Spectroscopy and Structure," Waterloo, Canada: University of Waterloo. Online resource, accessed November 8, 2013, http://bernath.uwaterloo.ca/media/molspec_combined.pdf

[109] Cecil, Eric, "Velocity Field Measurements in Rarefied, Hypersonic Flows of Nitrogen Using Laser-Induced Fluorescence of Iodine," *PhD Dissertation*, Charlottesville, VA: University of Virginia, 2011.

[110] Alkandry, H., Boyd, I.D., Reed, E.M., Codoni, J.R., McDaniel, J.C., "Aerodynamic Interactions of Reaction-Control-System Jets for Atmospheric Entry Aeroshells," *AIAA Journal*, Vol. 51, No. 5 (2013), pp 1105-1118.

[111] Dyakonov, A.A., Shoenenberger, M., Scallion, W.I., Van Norman, J.W., Novak, L.A., and Tang, C.Y., Aerodynamic Interference Due to MSL Reaction Control System," *41st Thermophysics Conference,* 2009, AIAA Paper 2009-3915.

[112] Broyer, M., Lehmann, J.C., "Rotational Landé Factors in the $B^3\Pi_{0+u}$ State of Iodine," Physics Letters A, Vol. 40, No. 1 (1972), pp. 43-44.